Surv Geophys (2017) 38:869–933
https://doi.org/10.1007/s10712-017-9435-1

Application of 3-D Electromagnetic Inversion in Practice: Challenges, Pitfalls and Solution Approaches

Marion P. Miensopust[1]

Received: 6 December 2016 / Accepted: 26 September 2017 / Published online: 30 November 2017

Abstract In recent years, three-dimensional (3-D) inversion of electromagnetic (EM) data gained a lot of attention and the number of 3-D EM case studies has increased. Many publications discuss the challenges and advancements of 3-D inversion with respect to the numerical aspects and often show synthetic studies to prove their assumptions. On the other hand, field data have other/additional demands than synthetic data sets. There are challenges and requirements to fulfil along the entire sequence from survey planning to interpretation. To obtain a meaningful and reliable interpretation it is not sufficient to only be aware of and address issues with respect to one step along this sequence. Ideally one should be concerned with all or at least most of them, because many of these challenges are related to or even consequences of each other. Not all issues when dealing with field data can be solved, but one should at least be aware of the consequences of unavoidable shortcomings as this knowledge may be crucial for interpretation. With the intention to raise awareness, this review comprises a variety of difficulties related to the data acquisition, the numerical part—preparation for and performance of 3-D inversion—and the interpretation itself, when dealing with field data sets. The majority of published work on 3-D EM inversion of field data is related to magnetotellurics; nevertheless, there are also aspects discussed that are specific to other EM methods or illustrate different ideas to deal with challenges (e.g., airborne and controlled-source EM).

Keywords Electromagnetics · 3-D inversion · Field data

✉ Marion P. Miensopust

[1] Leibniz Institute for Applied Geophysics, Stilleweg 2, 30655 Hannover, Germany

1 Introduction

Three-dimensional (3-D) inversion of electromagnetic (EM) data concerns the EM community for a while. Already in 1976, the first review paper on 'magnetotelluric modelling and inversion in three-dimensions' was published by Hewson-Browne and Kendall (1976). A few years later, Oldenburg (1990) stated in his review 'Efficient codes for solving the 3-D forward simulation problem are on the horizion'. In honour of Gerald W. Hohmann the series of 3-D EM Symposia started in 1995, offering the opportunity to discuss diverse aspects of 3-D EM modelling and inversion (Oristaglio and Spies 1999). In the outlook, Ogawa (2002) stated that the use of constraints will be important for 3-D inversion in order to incorporate a priori information and to stabilize the inversion. Finding appropriate trade-off parameters between data misfit and norms of constraints will also be essential. These statements are of course still true, but how far did we get to date?

Although the focus of this review is clearly on the practical issues and challenges when dealing with field data, there is always a close connection to the numerical aspects and synthetic studies. To understand the challenges and solution approaches, synthetic studies are sometimes required and therefore shown, but the amount of numerical aspects is as much as possible kept to a minimum. For deep insights, detailed review papers about numerical aspects have been given at previous EM induction workshops (e.g., Avdeev 2005; Börner 2010; Siripunvaraporn 2011; Newman 2013) and other relevant publications are referred to throughout the manuscript. The 'MT 3-D inversion' workshop series (Dublin 2008, 2011; Bari 2016) is a good example where synthetic magnetotelluric (MT) studies are applied to highlight and tackle challenges in 3-D inversion with specific aspects that might matter for real data (Miensopust et al. 2013; Jones et al. 2016; Vozar et al. 2016). However, the challenges and pitfalls of real data inversion already start way before the actual 3-D inversion algorithm comes into play and end far beyond the colourful image obtained from the inversion code. While this paper covers a broad range of those aspects, there is by no means a claim for completeness.

In principle, one can subdivide the sources of difficulties into three main areas of origin. One—often underestimated—part already comes into play during data acquisition and is related, for example, to survey design, position accuracy, noise of any kind and topography/bathymetry. The next area is related to the numerical part. It involves all challenges concerning the inversion procedure, namely data preparation, mesh design, error definition, parameterization and resolution, but also issues with respect to the trade-off between computational costs and image quality. Finally—anything but negligible—the interpretation of the obtained model can also be the cause of trouble, i.e. equivalent models as well as the use of a priori information and joint interpretation or inversion are a boon and a bane at the same time and can result in interpretation errors. Many of those issues are of course area overlapping or consequences of the others. However, no matter which EM method one considers many of those issues appear in one way or the other. One should also keep in mind that the demands on the data and resulting model/interpretation may vary from case to case and clearly differ for scientific versus commercial applications—especially in terms of the resulting consequences.

The variety of scales and targets that 3-D EM inversion is applied to is diverse. There are focused studies of local geological features such as small volcanoes and/or geothermal areas (e.g., Heise et al. 2008; Newman et al. 2008; Ingham et al. 2009; Árnason et al. 2010; Cumming and Mackie 2010), hydrocarbon reservoirs (e.g., He et al. 2010; Newman et al. 2010; Mansoori et al. 2016), ore deposits (e.g., Tuncer et al. 2006; Farquharson and Craven 2009; Xiao et al. 2010; Yang et al. 2014a), salinity mapping (e.g., Cox et al. 2012)

and waste site deposits (e.g., Newman et al. 2003) that are spatially limited (i.e. covering a few tens of square kilometres) and often have a reasonably well site coverage. But there are also larger-scale surveys investigating extended volcanic complexes (e.g., Hill et al. 2009; Kelbert et al. 2012) and major fault systems (e.g., Tietze and Ritter 2013). Of an even larger scale are studies of (mid-)continental rift systems and related volcanic activity (e.g., Heise et al. 2010; Bertrand et al. 2012a, b; Heise et al. 2013; Jegen et al. 2016) and geological and structural investigations of huge areas (e.g., Patro and Egbert 2008; Türkoğlu et al. 2009; Zhdanov et al. 2010, 2011; Patro and Egbert 2011; Thiel and Heinson 2013; Bedrosian and Feucht 2014; Meqbel et al. 2014; Padilha et al. 2015; Yang et al. 2015; Robertson et al. 2016; Ślęzak et al. 2016; Thiel et al. 2016).

All those studies are based on airborne, on- and off-shore data sets of controlled-source or natural-source EM methods. As the majority of published work is on 3-D MT inversion, most of the issues and examples discussed in this review are related to MT, but many aspects are similarly valid for 3-D inversion of other EM methods. There are also challenges specific to other EM methods or different ideas to deal with issues, and therefore, a few non-MT studies and concepts are included as well.

2 Data Acquisition

Positioning is a known issue for airborne and marine data. Therefore, a major part of data processing aims at the correction of position and adopting to a single coordinate system for the entire data set (e.g., Hunziker 2012; Garcia et al. 2015; Jegen et al. 2016). Also for land-based data sets, an accurate positioning is not always trivial. Especially for commercial applications, the enlarged uncertainty of the positioning due to poor satellite reception (e.g., vegetation and other kinds of shielding) is a challenge. In rough terrain, a digital elevation model is a good alternative to GPS elevations with errors of hundreds of metres (pers.comm. William Cumming 2016). To avoid the endless confusion and source of errors and misunderstandings, it is essential that the coordinate system, the data rotation (e.g., magnetic vs. geographic North), the sign convention and the time dependence which are used are unambiguously documented (e.g., Holtham and Oldenburg 2012). Additionally, the accuracy of the sensor orientation is of concern and is discussed in more detail by Ferguson (2012). Furthermore, each inversion code requires its individual input data format (including all the above-mentioned aspects). This can be an additional source of errors as converting the field data to the input data format and a Cartesian coordinate system has to be done outside the inversion algorithm and is left to the individual user.

Errors and noise during data acquisition have many sources, which are difficult or even impossible to quantify. For the MT case, challenges related to instrumentation, their calibration, layout errors and data acquisition are discussed in more detail by Ferguson (2012). In many areas, EM data suffer from high levels of electromagnetic noise, which originates from many different sources. Szarka (1988), Junge (1996) and Ferguson (2012) reviewed them in detail. The main sources of electromagnetic noise are artificial, such as railways, power lines, electric fences, cathodically protected pipelines, radio communication systems and all sorts of machinery (e.g., pumps, generators, vehicles) but also man-made conductors in otherwise resistive environment (e.g., metal tanks, unpowered metallic fences, pipelines and power plant facilities).

Additionally, spatial changes in electrical resistivity due to geological structures other than the survey target can be considered as geological noise (e.g., soil and regolith layers,

saline aquifers, salt lakes, swamps, coastlines, topography; Ferguson 2012)—often also called distortion (see Sect. 3.5). Furthermore, the level of noise at a given distance from a particular source depends on the resistivity distribution in the subsurface (e.g., Szarka 1988; Ferguson 2012).

How severe noise is for the data not only depends on the noise source and amplitude as well as the subsurface it propagates through but also on the source signal strength itself. In the MT case, during quiet geomagnetic periods (i.e. the signal level is lower), and in areas of conductive lithosphere (i.e. the electric fields are smaller) the effect of noise on the data will be greatest (Ferguson 2012). On the other hand, seeking for strong source signal (e.g., days of solar storm) improves the signal-to-noise ratio and hence the data quality (e.g., Cembrowski et al. 2016).

One should bear in mind, when talking about noisy data, that one means all data! Using lots of very good data will still not make it infinite exact data (Constable 2016). To deal with acquisition errors and noise, an assignment of appropriate uncertainties to the data is essential (see Sect. 3.1.3).

Field data are often collected along single or widely separated profiles rather than on a grid of well-distributed sites. Moreover, if the layout is aiming at a regular and dense array it might be precluded due to logistical limitations and external circumstances in the field (e.g., terrain, infrastructure, noise conditions) or purely lack of time, funds and/or equipment (i.e. a trade-off between cost and benefit/quality). The absence of an equidistant site distribution makes the 3-D inverse problem more unstable. Nevertheless, in the presence of 3-D structures performing solely 2-D inversions of the individual profiles may not be an alternative or is at least subject to restrictions (Ledo 2005; Ivanov and Pushkarev 2010).

For the majority of case studies, the number of sites available for 3-D inversion varies from a few tens (e.g., Xiao et al. 2010; Patro and Egbert 2011; Heise et al. 2013; Thiel and Heinson 2013; Ślęzak et al. 2016) to a few hundreds (e.g., Heise et al. 2010; Tietze and Ritter 2013; Mansoori et al. 2016) sites, which sometimes are not uniformly distributed over an area of interest. Some studies even applied 3-D inversion to profile data, i.e. a single profile, intersecting or parallel profiles (e.g., Bertrand et al. 2012b; Xiao et al. 2010; Patro and Egbert 2011; Heise et al. 2013; Jegen et al. 2016). One reason is the 3-D nature of the observed responses, although the site distribution is restricted to a single profile (Heise et al. 2013). Another reason is the observation that 3-D inversion results provide more realistic images beneath the profile and possibly even limited resolution of off-profile structures, if the full MT tensor is considered (Siripunvaraporn et al. 2005b; Patro and Egbert 2011). For some studies, more or less equally distributed arrays are available (e.g., Heise et al. 2010; Thiel and Heinson 2013; Robertson et al. 2016) and others are a mix of profile data and array-like distributed sites, where spatially subsampling of the profile lines is used to achieve a roughly even site spacing (e.g., Thiel and Heinson 2013). The influence of the site coverage on the final inversion result is shown later (see Sect. 3.8.5).

The final inversion results can be improved if the survey planning and data acquisition already consider those aspects mentioned above and a few others. For example, a target depth close to the MT investigation depth at the noisy frequencies of the dead band around 1 Hz desires redundant station spacing (Cumming and Mackie 2010). Marine MT surveys require an appropriate site spacing in the area where coast effects are expected (see Sect. 3.5). Additionally, the loss of instruments—and therefore, loss of data—is an additional issue for marine MT as well as conflicting interests with the active fishing industry (e.g., bottom trawling in water depths down to $\approx$ 800 m; Garcia et al. 2015). For radio MT (RMT), Newman et al. (2003) showed that an additional reference profile outside

the target area may be useful to obtain an unscreened background resistivity image yielding advanced inversion results of the target area.

3 Preparing, Performing and Validating 3-D Inversion

The numerical solution of the inverse problem, which is inherently ill-posed (Tikhonov and Arsenin 1977), depends not only on the data quality and amount of a priori information but also on one's level of expertise. The latter introduces some degree of subjectivity regarding the choice of an initial model, its parameterization and various variables (e.g., error floors and estimates, weighting coefficients and regularization parameter) as optimal values are often not available or difficult to determine in practice (Tietze and Ritter 2013; Grayver 2015; Lindsey and Newman 2015). Additionally, Cumming and Mackie (2010) pointed out that it is likely that 3-D MT inversions, in general, are less forgiving of noisy data and data gaps than 1-D and 2-D are and therefore require more careful editing of input data. At the same time, contradictorily a lot less periods are used for 3-D inversion as there are for 1-D and 2-D (see Sect. 3.1.2).

In general, inversion codes do not perform plausibility checks on the inputs, i.e. the code will not stop if the model dimension, the distance to model boundaries or cell sizes are not appropriate for the given sites and frequencies. Hence, an unsophisticated user risks obtaining a colourful but absolute meaningless resistivity model. Furthermore, as soon as frequencies differ at least at the last decimal place provided they will be considered as two separate frequencies. This increases the computing time or the required number of nodes as most codes are based on calculations done for each frequency individually. All this has to be taken care of outside the inversion and requires thoughtful decisions and careful data preparation and model/mesh design.

In many cases, the preparation of the data for inversion is underestimated, which is according to Holtham and Oldenburg (2012) the most critical aspect of the entire inversion process. Nevertheless, there are also many more aspects that can lead to solution bias, inefficient model-data convergence or in some cases even to lack of convergence. In the following, aspects of data preparation (see Sect. 3.1), mesh design (see Sect. 3.2), initial and prior models (see Sect. 3.3) will be discussed. Inversion parameters (see Sect. 3.4), dealing with distortion (see Sect. 3.5) and large data sets (see Sect. 3.6) as well as misfit (see Sect. 3.7) and model assessment and resolution (see Sect. 3.8) are also addressed.

3.1 Data Preparation

Due to much larger numbers of elements and degrees of freedom in a 3-D model (compared to 1-D or 2-D) that must be constrained by data, there is more opportunity for a 3-D inversion to produce unrealistic results if misleading data are included. Smoothing and robust processing alone are insufficient to obtain realistic results from 3-D inversion if data with noise—especially correlated noise—are not (or only lightly) edited (Cumming and Mackie 2010).

One important step from field data to inversion is robust processing and error estimation to obtain reliable data. As there are many publications (e.g., Egbert and Booker 1986; Chave et al. 1987; Jones et al. 1989; Garcia and Jones 2008; Myer et al. 2011; Chave 2012; Streich et al. 2013) and an entire review by Chave (2017) about this topic, it will not be discussed further here. However, there are many other aspects of data preparation (i.e.

dimensionality and strike analysis, data selection as well as uncertainties) that are important too and will be described in the following.

3.1.1 Dimensionality and Strike Analysis

To get a good first impression of a data set, quality and dimensionality/regional structures plotting simple maps and sections (e.g., for MT data impedance tensor and induction arrow maps) is often helpful. Also prior to full 3-D inversion, thorough analysis of dimensionality and strike behaviour of the data set is advisable. Being aware of parameters related to dimensionality and strike analysis is advantageous for the 3-D inversion. They either are used indirectly [e.g., rotation of coordinate system for inversion (see Sect. 3.2), additional information for model appraisal (see Sect. 3.8)] or directly [e.g., phase tensor inversion (see Sect. 3.5)].

One possibility is to use the phase tensor approach (Caldwell et al. 2004) for dimensionality and also strike analysis (e.g., Patro and Egbert 2011; Tietze and Ritter 2013; Patro and Sarma 2016; Ślęzak et al. 2016). Lilley (2015) discussed some limitations of the phase tensor approach related to strong distortion (i.e. distortion tensor may become singular) and accounting for data error (i.e. distortion matrix may be indistinguishable from singular). Another procedure is the WALDIM approach (Martí et al. 2009), which is based on rotational invariants of the MT tensor (Weaver et al. 2000).

3.1.2 Data Selection

While most studies admit that sites with bad data quality are rejected for inversion, there hardly is any specification when data are considered too bad to be included and it seems a matter of personal choice. While industry with huge amounts of sites and data is quite rigorous with rejection (also large scientific projects—e.g., Heise et al. (2010) used 220 out of 276 sites recorded), especially small-scale scientific studies with only very few sites tend to be very attached to their collected data and try to include them all. Another reason to exclude sites from inversion is too close site spacing (e.g., less than 2 km for a crustal study by Heise et al. 2010) or to minimize influence of an irregular site distribution (e.g., Tietze and Ritter 2013) or sites located in the high conductive part of geothermal systems (e.g., Heise et al. 2010). Preference may be given to sites with high data quality, covering a wide period range and/or where both impedances and vertical transfer functions are available (e.g., Tietze and Ritter 2013).

Not only must the sites be selected, but also the periods considered during inversion need to be chosen. Only in a very few cases is information, such as the removal of noisy data, smoothing with a spline function, interpolation or a manual inspection of the data points is provided (Heise et al. 2010; Tietze and Ritter 2013). Often—if at all—one finds a statement that three to four periods per decade are used (e.g., Kelbert et al. 2012; Thiel and Heinson 2013; Tietze and Ritter 2013; Burd et al. 2014; Lindsey and Newman 2015; Jegen et al. 2016; Ślęzak et al. 2016; Meqbel et al. 2016; Patro and Sarma 2016) or even less (about two per decade by Heise et al. 2010; Patro and Egbert 2011) while five to six is an exception (e.g., Robertson et al. 2016). Recently, Yang et al. (2015) published inversion results from EarthScope MT data (Schultz et al. 2006–2018, 2008–2013) using eight periods per decade (28 in total). As for each period used the entire system of equations must be solved, the computational costs are often the excuse to only consider so few periods. Hence, what are the effects on the resulting inversion model? Do artefacts appear? Is there any loss of information?

It seems that data are processed to be appropriate for 2-D inversion, which requires a downsampling (with or without interpolation/smoothing) to prepare them for 3-D inversion. Instead of data rejection, one could process the data to give an appropriate number of periods per decade for 3-D inversion. The advantage would be data with a better statistical reliability, but it requires processing the data twice to obtain two different response sets for 2-D and 3-D inversion. No matter which approach is used, a clear and reproducible documentation is required.

Another decision that is to be made regarding data selection is which data components are included. This is not only a decision if impedance and vertical transfer function (VTF) data are both included (e.g., Kelbert et al. 2012; Tietze and Ritter 2013; Yang et al. 2015; Ślęzak et al. 2016) but also which impedance tensor elements are considered. One major difference compared to 2-D MT data is that in 3-D the diagonal elements of the impedance tensor are nonzero. The importance of the diagonal elements in the inversion, their influence on the results and the meaning of nonzero diagonals are still under discussion. Although nonzero, they are often several orders of magnitude smaller than the off-diagonals, and therefore, some argue they are basically zero (i.e. can be neglected). On the other hand, the diagonal elements of field MT data are, even though they are a few orders of magnitude smaller than the off-diagonal elements, by far larger than for the synthetic cases. Presumably this is a consequence of imperfect data acquisition, such as instrument noise and inaccuracy, external noise (e.g., artificial and wind noise) and distortion. Hence, how should diagonal elements be treated in 3-D inversion? Do measured diagonal elements only contain information about distortion and noise? There are no satisfying answers for those questions yet. The following examples only summarize the experiences made and conclusions drawn by those authors with their specific case studies and not a final and general conclusion of the correct treatment of diagonal elements.

While some studies use the full impedance tensor for 3-D inversion (e.g., Heise et al. 2013; Thiel and Heinson 2013; Tietze and Ritter 2013), many recent publications show 3-D MT inversion results where only the off-diagonal element data are used (e.g., Tuncer et al. 2006; Newman et al. 2008; Zhdanov et al. 2010; Lindsey and Newman 2015). Lindsey and Newman (2015) found the ratio of on- to off-diagonal element amplitudes to be about 1:10 for most of their geothermal MT data (higher on-diagonal amplitudes are mainly observed below 1 Hz), and therefore, they justify ignoring the on-diagonal elements during 3-D inversion. Newman et al. (2008) found that the performance of the inversion is degraded due to the lower magnitudes and, therefore, lower signal-to-noise ratios of the diagonal elements, if they are included.

Patro and Egbert (2011) showed a comparison of inversion based on full impedance and only off-diagonal component data from Edlabad–Khandwa at the Deccan volcanic province of western India (see Fig. 1). Both—full impedance (Fig. 1b) and off-diagonals only (Fig. 1c)—were inverted using the same periods and inversion parameters, but show a noticeably different pattern of conductive and resistive crustal structures. The authors state that fitting only off-diagonal components with 3-D inversion yields models more like the 2-D results, but without smaller conductive features. In this case, 3-D inversion of off-diagonal components only seems to have little benefits over 2-D inversions, while the full impedance 3-D inversion provides a much more detailed subsurface image.

As mentioned above selections are not only made to separate good and bad quality data but are also an approach to simply reduce the size of the numerical problem, and therefore, accelerate the inversion. Grayver et al. (2014), for example, claimed that to run 3-D inversion of controlled-source EM (CSEM) data efficiently, a non-redundant data subset is required that effectively contains all of the subsurface information and allows running

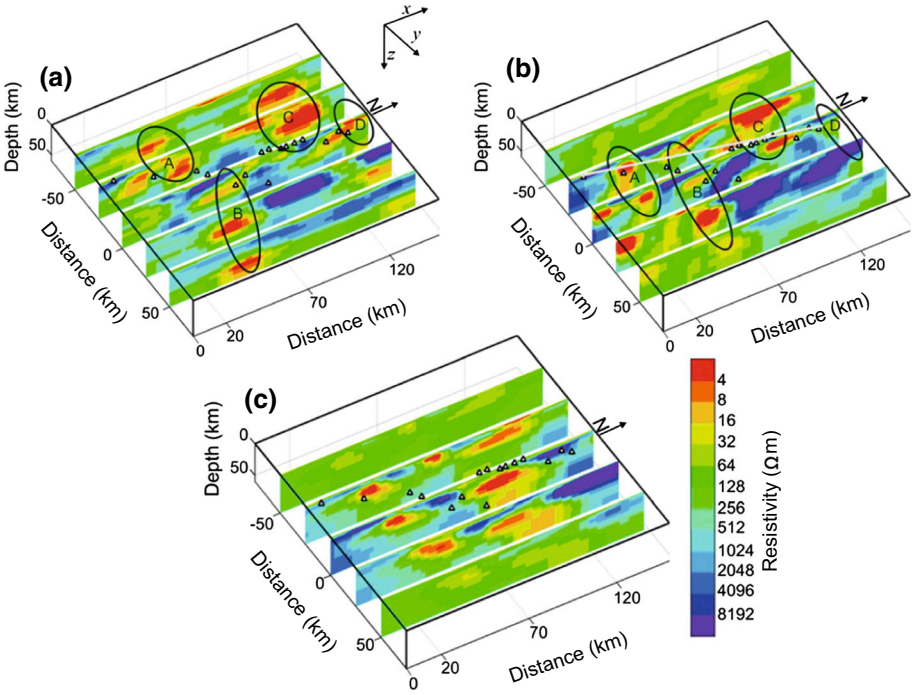

Fig. 1 Final inversion models from the Edlabad–Khandwa data (sites indicated by triangles), Deccan volcanic province of western India (modified after Patro and Egbert 2011 with permission from Elsevier). The models based on full impedance data were obtained (**a**) using default isotropic covariance (i.e. model length scale $\delta_x = \delta_y = \delta_z = \sqrt{2}$) and (**b**) anisotropic model covariance to increase smoothing along geoelectric strike (i.e. $\delta_x = \delta_z = \sqrt{2}, \delta_y = \sqrt{10}$). See Sect. 3.4 for discussion of inversion parameters. Inversion of only off-diagonal tensor components and anisotropic model covariance are shown in (**c**) and reveal noticeably different patterns of conductive and resistive crustal features especially to the north

multiple inversions within manageable time. Redundancy in a CSEM data set is caused by overlapping information in different frequencies and EM field components and is a result of the transmitter setup with linearly dependent currents (Grayver 2013). Grayver et al. (2014) only used horizontal electric field components in the real data inversion because the magnetic fields generally have little sensitivity to resistive objects (e.g., Oldenburg et al. 2013b), while electric fields are sensitive to both—resistors and conductors (e.g., Constable and Weiss 2006).

3.1.3 Uncertainties and Data Weighting

Constable (2016) described the correlation of data errors, data weights and uncertainties as follows: the sources of data error are diverse, and error estimates are a tool to weight data (or components) during inversion. Commonly the data weighting matrix is based upon the inverse of the error estimates of the measured data. Therefore, error estimates (and error floors) are as important as the actual data estimate and should not be applied blindly. While one can handle statistical processing errors relatively well (e.g., MT spectral estimation, CSEM stacking), all the rest is lumped in some sort of uncertainty. The latter comprises not only the above-discussed artificial and natural electromagnetic noise but also systematic

errors such as navigation errors, installation errors and instrument calibration as well as geological noise (i.e. our inability to parameterize fine details of geology sufficiently well; see Sect. 2). It is difficult to quantify the individual contributions of the various error sources, let alone their cumulative effect.

Various authors deal with data errors very differently. Sometimes the purely statistically determined variance of the observed data (i.e. impedance tensor elements) is used (e.g., Patro and Egbert 2008; Farquharson and Craven 2009; Árnason et al. 2010), while others combine these determined variances with pre-set error floors (Tuncer et al. 2006; Ingham et al. 2009; Türkoğlu et al. 2009; Patro and Egbert 2011; Bertrand et al. 2012a; Kelbert et al. 2012; Burd et al. 2014) or use a percentage of the data value as relative errors (Heise et al. 2008; Newman et al. 2008; Hill et al. 2009; He et al. 2010; Heise et al. 2010; Xiao et al. 2010; Tietze and Ritter 2013; Jegen et al. 2016).

There are also various strategies to assign relative errors or error floors. One approach is to use a percentage of $\sqrt{Z_{xy} \cdot Z_{yx}}$ to all four impedance elements. However, one should be very careful when doing so, as noise that is only present in one electric (or magnetic) field component can be propagated to all others—originally not affected—components. For land MT data a common assumption is that the main noise is in the electric field components. Therefore, Z_{xx} and Z_{xy} often have error floors assigned based on a percentage of the absolute value of Z_{xy} (Z_{yx} and Z_{yy} are based on Z_{yx}, respectively). Otherwise for marine MT data, the noise is actually in the magnetic field, hence, Z_{xy} should be used for Z_{xy} and Z_{yy} and Z_{yx} for Z_{yx} and Z_{xx}. The applied percentages vary and are usually about 3–5% for the impedance off-diagonal elements and at least 5–10% for the diagonals. Others use a percentage for each individual impedance tensor element. Using the latter approach one risks very small errors for Z_{xx} and Z_{yy} that are not feasible for the entire period range and give too much weight to them during inversion. This can result in over-fitting the diagonals and at the same time in a poor fit of the off-diagonals and may create artefacts in the inverted model. Therefore, Thiel and Heinson (2013) assigned a ten times higher percentage to the diagonals than to the off-diagonals. On the other hand, defining large errors would effectively downweight or omit information contained in the diagonals, and therefore, Tietze and Ritter (2013) applied an error floor based on $|Z_{xy} \cdot Z_{xy}|$ to the diagonal elements and emphasized that relative sizes of components are taken into account for a sensible data weighting scheme.

For 2-D, Wheelock et al. (2015) found that logarithmic amplitude and phase are the optimal data format and misfit space to perform the inversion. Considering diagonal elements for 3-D inversion, they point out that there is a risk that the logarithm approaches negative infinity and the phase becomes undefined. That is the reason why many 3-D studies interpret and invert real and imaginary impedance and tipper data, but instead Wheelock et al. (2015) suggested introducing a threshold to remove both logarithmic apparent resistivity and phase data from an inversion once their relative error percentage exceeds a chosen value. Similarly, Miensopust et al. (2013) suggested to use a threshold value (in this case based on an absolute apparent resistivity value) to distinguish whether the diagonal element values contain structural information, and hence should be included in an inversion, or not.

In general, it is a good approach to assume natural-source data errors that are some percentage of the data plus some error floor (Holtham and Oldenburg 2012). Nevertheless, for the VTF data a constant absolute error is used for on-shore data [commonly 0.01–0.03; e.g., Tietze and Ritter (2013), Burd et al. (2014), Padilha et al. (2015), Yang et al. (2015), Meqbel et al. (2016)], but at the ocean floor a relative error in combination with an error

floor is commonly used. More and more studies show a combined inversion of full impedance and VTF data, where the chosen errors balance the influence of the different components. The study by Tietze and Ritter (2013) even uses the comparison of separate and joint inversion of full impedance and VTF for model assessment (see Sect. 4.1).

Looking at MT response curves it is often visible that parts of the data (e.g., in the dead band) scatter a lot, while other parts look rather smooth. Ideally, errors should be assigned such that the scatter is completely covered but not exceeding them. If individual errors are applied for each period, an additional absolute error floor for each component is required.

When jointly inverting multiple EM data sets additional re-weighting may be required (e.g., if significantly more data are available for one data set). Similar to considerations in 2-D (e.g., Candansayar and Tezkan 2008; Kalscheuer et al. 2010; Wheelock et al. 2015; Key 2016), Commer and Newman (2009) and Meqbel and Ritter (2015) discussed data weighting when different EM data sets are jointly inverted. Assuming similar noise levels, for joint inversion of CSEM and MT data (if the number of CSEM data $\gg$ the number of MT data) the more numerous CSEM data can cause the influence of MT data on the final inversion model to become insignificant (Commer and Newman 2009). Therefore, an additional trade-off parameter between the different data types is required to obtain a more balanced data influence. A weighting scheme, based on the number of data points each method contributes, requires a high confidence in the individual error estimates and similar intrinsic sensitivities of both methods. As the latter vanishes with less overlap in model resolution capacities between both data sets, Commer and Newman (2009) suggested a re-weighting approach based on the ratio of the data gradient norms, considering only the data constituents in the objective function. This approach incorporates both the quantity and resolution capacity in the joint data set. Meqbel and Ritter (2015) applied an adaptive data gradient approach to invert jointly MT, CSEM and geo-electric data. They determine the norm of all individual data gradient vectors as well as the total data gradients after each nonlinear conjugate gradients (NLCGs) iteration. To obtain equal contribution Meqbel and Ritter (2015) computed weighting parameters that result in higher weights for data gradients that originally had less influence and vice versa. Both studies—by Commer and Newman (2009) and Meqbel and Ritter (2015)—showed that joint inversion of multiple EM data sets can have advantages over the individual inversions of the methods, but an appropriate weighting between the data sets is essential.

Joint inversion of EM and other data (e.g., seismic and gravity data) comprises very similar issues of data weighting and different resolution capacities. More details on the application of joint inversion of methods sensing different physical properties can be found in the review by Moorkamp (2017).

3.2 Mesh Design

Talking about inaccuracies and errors of inversion one should remember that an inversion algorithm is always based on a forward solution. Any inaccuracy or error in the forward solution process is propagated into the inversion. Even if one uses the true subsurface resistivity structure as an initial model, if the forward solution is not perfect the inversion will try to fit the measured data to the dissenting synthetic data, and therefore, the model will be modified away from the true model. How significant this effect is for the final model depends on how inaccurate the forward solution is. Especially challenging for the forward solution—and hence for the inversion—are, for example, rough topography and bathymetry but also structures and interfaces in the true resistivity distribution that do not match the chosen model discretization. While the rectangular meshes of finite-difference

(FD) and integral equation (IE) methods require boundaries to be perpendicular, the finite-element (FE) approach is—due to unstructured grids—more flexible, but in all cases any interface must be located at the cell edge. The Dublin test model DTM2 (an outcropping conductive (10 Ωm) hemisphere of 5 km radius in a 300 Ωm half-space; Miensopust et al. 2013) was originally designed to investigate how well galvanic effects are dealt with. The simple geometry was chosen because for a hemisphere analytic solutions exist at the galvanic limit (Groom and Bailey 1991), i.e. for long periods only. Figure 2 shows a data example of a site located outside but close to the edge of the hemisphere. Firstly, the analytic solution considering only the galvanic effects on the electric field (i.e. only the galvanic distortion tensor C is applied to the true impedance tensor $Z_{\text{true}} \rightarrow Z = CZ_{\text{true}}$, after Groom and Bailey 1991) is indicated by a grey dashed line. Secondly, the full analytic solution of the galvanic scatterer was calculated by David Bosch (after Groom and Bailey 1991) and is represented by the solid black line. Blue symbols represent the various FD response curves, green symbols are the FE results, and the IE responses are in red. Note that, although the code by Farquharson is an FE code, it used a rectangular mesh. Using rectangular meshes, the blocky discretization of the hemisphere boundary causes a large variation in the response curves at sites in its proximity (Fig. 2). One can see two clusters of resistivity curves at site 18, and the phases show a bit of scattering at short periods. While the top cluster scatters around the analytic solution for long periods the bottom one comprises the three response curves obtained using a minimum cells size of 500 m lateral edge length, which is twice (or more) of the length used for the responses of the top cluster. This clearly shows how significant the artefacts of rectangular meshes can be. Those artefacts are purely caused by the meshing and are by no means related to static shift and

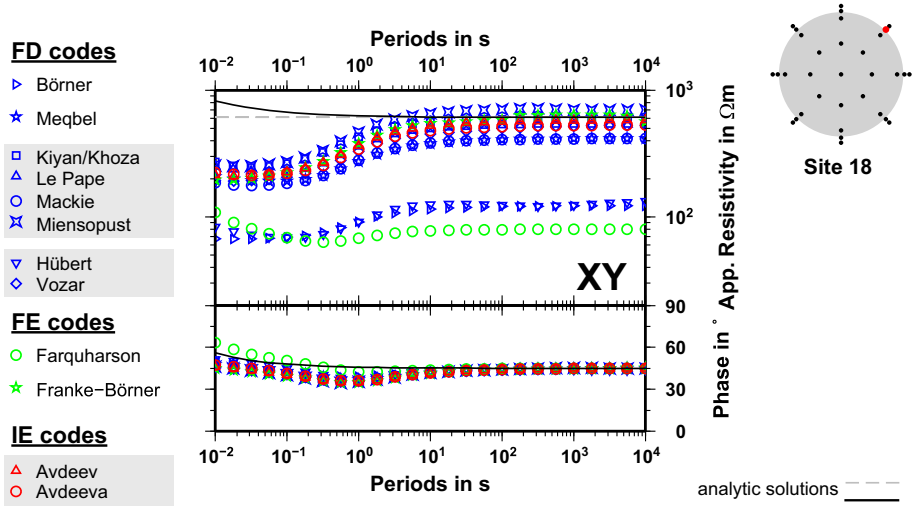

Fig. 2 Comparison of the obtained XY components of the DTM2 responses (i.e. apparent resistivity and phase curves). The left column lists the different FD, FE and IE results named after the person calculating the responses (grey shading indicates usage of the same code). The middle shows the responses at site 18, whose location is indicated by the red dot in the small sketch on the top right (outside the hemisphere, at surface 100 m away from the edge). The grey dashed line represents CZ_{true} and the solid black line the analytic solution calculated by David Bosch (after Groom and Bailey 1991). Note that both analytic solutions are only valid at the galvanic limit, i.e. for long periods. The comparison of all components as well as the detailed information about the meshes, forward parameters and used codes is given by Miensopust et al. (2013)

distortion originating in field data due to small-scale near-surface heterogeneities. Additionally, the variation in volume and exact depth of the bottom of a blocky discretized hemisphere can even affect sites that are more distant. While most people are aware of the artefacts when considering topography (i.e. using a rectangular realization of elevation), it sometimes is neglected that the same happens in the subsurface part of the mesh too. These artefacts are mostly 'automatically' prevented in synthetic studies, as usually for numerical tests one uses a matching combination of model structure and mesh, but they are relevant for field data inversion.

As the subsurface must be discretized to solve Maxwell's equations, the discretization is a compromise between numerical accuracy in the forward modelling and the computational costs (i.e. time and required resources). Especially if the variation in elevation is significant, a sufficient accurately discretized topography as well as correct positioning of sites on the surface is required. Using regular rectangular meshes, this can require very large meshes. There exist various approaches on the numerical side that try to minimize the excessive needs. Beside unstructured grids, codes use octree meshes (Haber and Heldmann 2007), adaptive meshes (Haber et al. 2012; Grayver 2015; Grayver and Kolev 2015) and local meshes (Yang et al. 2014b) or indeed deal with huge meshes of extremely fine cells running massively parallelized on huge clusters [e.g., electromagnetic geological mapper (EMGeo) by Newman and Alumbaugh (2000), Newman and Boggs (2004)]. These are examples of numerical advancements to tackle the challenge of fine enough discretization and limited resources (see also Sect. 3.6 and the mentioned publications).

If the full impedance tensor is used, the resulting 3-D inverse model is not always independent of the coordinate system (Tietze and Ritter 2013). While for VTF-only data, the resulting models show very similar resistivity structures, the effect of the chosen coordinate system has a significant influence on the resulting 3-D models based on impedance-only (Z) and combined Z and VTF data. Figure 3 shows an example from the central San Andreas Fault in California (only Z + VTF is shown here, for Z-only and VTF-only inversion see Tietze and Ritter 2013). The highly conductive zone (HCZ, 1–10 Ωm) is only recovered, if the coordinate system is aligned to the predominant geo-electric strike direction (N41W°) but not if a geographic coordinate system (N00°) is used. Their explanation is that, in the general 3-D situation, the impedance tensor components are interrelated, but 3-D inversion codes cannot handle them independently as data covariance is not taken into account. Therefore, they recommend to perform the 3-D inversion in a coordinate system where the coupling between the components is minimized and the current systems have the strongest separation, i.e. are aligned with the predominant geo-electric strike direction. This of course means that an essential pre-processing step for 3-D inversion should be a detailed strike analysis (see Sect. 3.1.1). Similarly, Burd et al. (2014) rotated their mesh and data set to the strike of the Pacific Coast and subducted slab. Rotation of the mesh has also influence on the regularization and smoothing (see Sect. 3.4).

3.2.1 Topography and Bathymetry

If topography or bathymetry is included, the rectangular realization of FD and IE codes but also the smoothing of real interface roughness by FE cells holds the risk that sites are not placed at the cell faces but below or above them. This results in very different responses and therefore can be misleading for the inversion process, as the data have been measured at the interface. Currently also not considered are tilts in the sensor orientation in the forward and inversions codes. While marine MT data (Jegen et al. 2016) and airborne EM

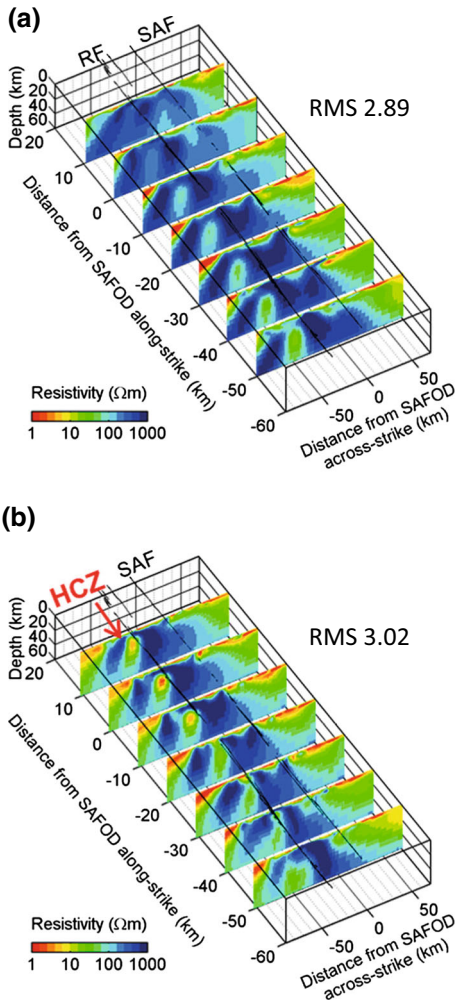

Fig. 3 Influence of the coordinate system on the 3-D inversion model. Example impedance (Z) and vertical transfer function (VTF) data from central San Andreas Fault in California. The comparison shows the 3-D inversion result using (**a**) a geographic coordinate system (N00°) and (**b**) a coordinate system aligned to the predominant geo-electric strike direction (N41°W). The final RMS misfit is specified. The highly conductive zone (HCZ, 1–10 Ωm) is only recovered if the strike-aligned coordinate system is used (modified after Tietze and Ritter 2013) (*SAFOD* San Andreas fault observatory at depth)

data are corrected for tilt, its effects are generally neglected for on-shore data. Additionally, strong field attenuation at the bottom of the seafloor and at short periods results in inaccurate forward responses, which may cause problems for inversion especially for older codes using single precision (pers.comm. A. Avdeeva). Most likely, this is rather a problem for synthetic studies than for real data, which are not measurable in practice at such short periods to date.

Including the coastline and bathymetry in a fine discretized mesh is required to fit coast-distorted MT data well (e.g., Constable et al. 2009; Key and Constable 2011; Worzewski et al. 2012; Jegen et al. 2016). The coast-perpendicular electric fields are distorted as they intersect with the resistive seafloor topography and the coastline (e.g., Cox 1980; Ranganayaki and Madden 1980) causing unphysically small resistivity values (Constable et al. 2009). The very large currents flowing parallel to the coast cause inductive effects on-shore (Fischer 1979) and off-shore (Constable et al. 2009). The latter is characterized by a minimum of the horizontal magnetic field perpendicular to the coastline and a phase

reversal in the field (Constable et al. 2009). In 2-D, this phenomenon is described in detail and the influencing components are systematically studied (e.g., Constable et al. 2009; Key and Constable 2011; Worzewski et al. 2012). Worzewski et al. (2012) also showed that the coast effect contains information on the host resistivity and increases the sensitivity to conductive anomalies. As the maximum coast effect is of localized nature, they pointed out that a dense coverage of marine stations is essential for detection. To handle the strong distortion effect at the coast, it is important to have sites on both sides—on- and offshore—to have good constraints on the strong resistivity contrast or a good a priori resistivity model on the opposing side of the array (Jegen et al. 2016). Jegen et al. (2016) also found that the 3-D resistivity variations in their MT data are not only caused by 3-D structures within the seafloor but also by the rough and complex bathymetry. They rate the errors introduced to the 3-D model by neglecting the complex and pronounced bathymetry as more significant than the effect due to irregular site distribution across the survey area. Therefore, the mesh has to be fine enough to approximate the bathymetry to achieve accurate solutions for smaller periods while at the same time should not become too demanding on computation time and memory requirements. To address this, Burd et al. (2014) approximated the ocean using a layer of constant thickness but varying electrical conductance (i.e. layer thickness divided by electrical resistivity). This ocean layer has high resistivities where the water is shallow and low resistivities where it is deep.

3.2.2 Boundaries and Cell Sizes

Considering the lowest inverted frequency, effects of the lateral boundaries become negligible at a distance of three times the skin depth (Weaver 1994). This rule of thumb is also often used in 2-D. Nevertheless, Lindsey and Newman (2015) recommend to place the boundaries five skin depths away as it warrants the required distance in geologic environments where a priori estimations of penetration depth often underestimate reality. In the vertical direction, the model space should extend also a few skin depths into the earth and incorporate the air to pad the model towards the top boundary. To limit the vertical depth extent for large-scale (L)MT experiments another valid approach is to include the known conductivity jumps at 410 and 660 km depth which have an attenuating effect due to the low resistive layers associated with them (see also Sect. 3.3).

It is always a trade-off to extend the mesh far enough and still keep a reasonable resolution at the area of interest. Usually the cell size is kept constant inside the area of interest (e.g., Lindsey and Newman 2015) and then is increased towards the boundary for the so-called padding cells by a factor (typically 1.2 to 1.3; e.g., Tietze and Ritter 2013; Lindsey and Newman 2015; Yang et al. 2015). Additionally, the mesh should match the survey geometry, i.e. the lateral cell sizes should not be much smaller than the distance between neighbouring sites. About a fifth to a sixth of the spacing is considered reasonable (e.g., Bedrosian and Feucht 2014; Meqbel et al. 2014; Jegen et al. 2016). On the other hand, the example by Meqbel et al. (2014) shows that a too coarse mesh leads to increased misfits (Fig. 4). The finer mesh (12.5 km instead of 25 km; 70 km site spacing) considerably improves the misfit in general but especially for the VTF data and the Z_{yy} component. Furthermore, conductive structures appear narrower in the finer discretized case.

A common approach for the vertical cell extent is to keep it constant in the shallow part [e.g., top 12 layers (Padilha et al. 2015), for 1–8 km below surface (Lindsey and Newman 2015)]. Alternatively, some use only a very thin first layer and then increase the subsequent vertical cell sizes by a factor (typically from 1.12 to 1.4; e.g., Patro and Egbert 2011; Tietze

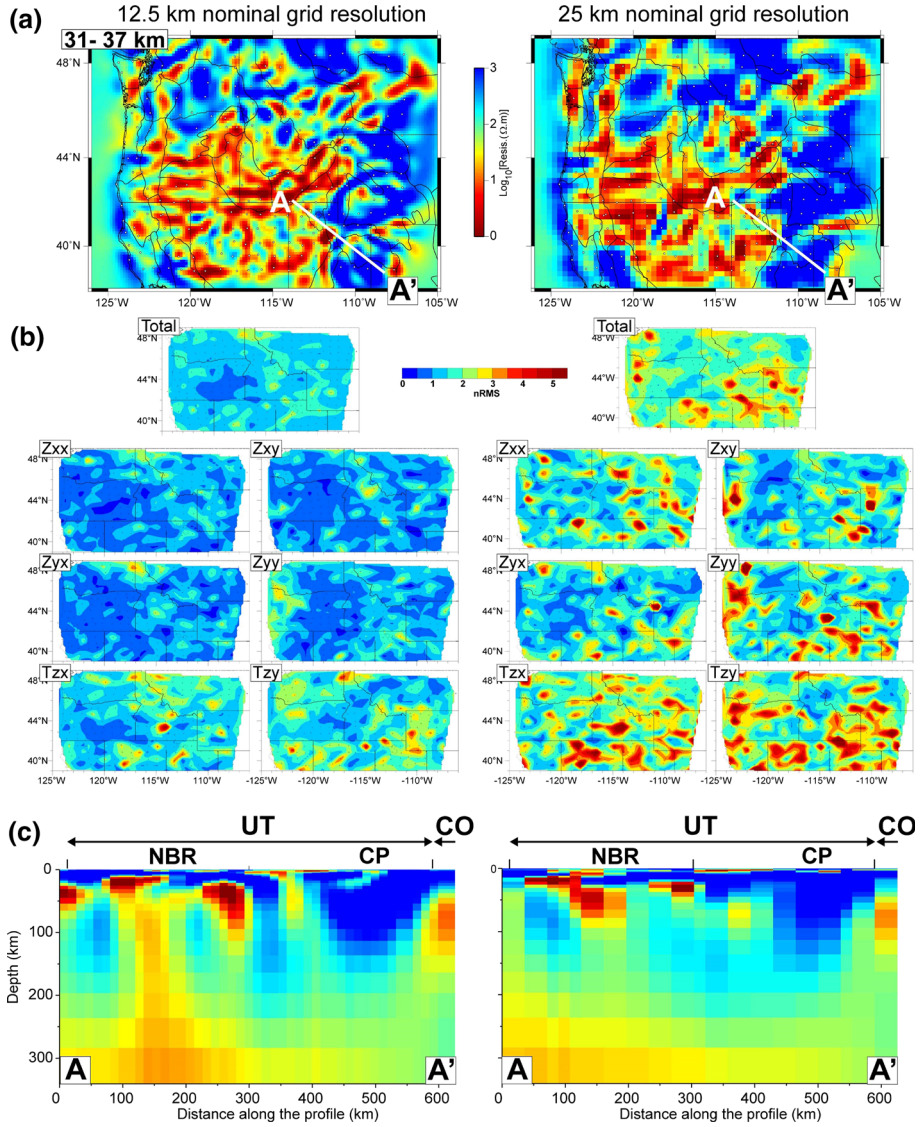

Fig. 4 Comparison of inversion results obtained with 12.5 km (left) and 25 km (right) centre cell sizes (Meqbel et al. 2014). Site spacing is about 70 km, and the shortest period is about 10 s. A plan view (**a**) near the base of the crust (31–37 km depth), the RMS misfit (**b**) averaged over periods for total and each individual components and cross sections (**c**) are shown (Reprinted from Meqbel et al. (2014) with permission from Elsevier)

and Ritter 2013; Yang et al. 2014a; Lindsey and Newman 2015; Padilha et al. 2015; Yang et al. 2015; Jegen et al. 2016; Patro and Sarma 2016).

Meshes designed for WSINV3DMT (Siripunvaraporn et al. 2005a) consist of only a few tens of cells in each direction (about 20–65 cells in lateral and 20–50 cells in vertical direction; e.g., Heise et al. 2010; Patro and Egbert 2011; Thiel and Heinson 2013), which can result in a very coarse grid spacing of several kilometres (e.g., 10 km or even 20 km

lateral cell extent in the central part of the mesh; Patro and Egbert 2011; Yang et al. 2015, respectively). Therefore, there might be more than one site placed within a single cell. Lindsey and Newman (2015, using EMGeo) consider such a low number of cells as coarse mesh and use it for the first inversion step, while their final finer mesh has about 90–150 cells in each direction (see Sect. 3.2.3 for more details on this sequenced approach). For the inversion using ModEM (Egbert and Kelbert 2012; Kelbert et al. 2014), Tietze and Ritter (2013) designed meshes with an inner uniform part (lateral edge length 4 km) of about 35 cells in lateral and 57 cells in vertical direction. Those meshes are laterally padded by 21 and 15 cells of increasing size, respectively.

Extremely large meshes are required if, for example, the survey area is influenced by two large-scale structures one each side. As the data are sensitive to resistivity variations beyond the site locations, inversion codes based on an integral equation approach or those using 1-D boundary conditions at the edges of the mesh will struggle. Jegen et al. (2016) faced this problem when inverting an amphibian data set being influenced by ocean in the west and the continental crust to the east; hence, a single 1-D background model was inadequate. Therefore, they extended the mesh so far that the influence of the 1-D background model was negligible. To find a reasonable trade-off Jegen et al. (2016) used 10 km horizontal cell sizes for a site spacing of up to 60 km, and vertical cell dimensions from 10 m to 50 km to approximate the bathymetry for an area of 906 km $\times$ 920 km $\times$ 300 km. This solved the problem of the 1-D background, and they obtained a mesh of 96 $\times$ 92 $\times$ 34 cells.

One should also consider that some codes (e.g., WSINV3DMT) require the sites to be located at the centre of the grid cell. Especially when using large cells the site might be misplaced by a few kilometres. The influence of these shifted sites on the final inversion result is still to be investigated.

Borehole-to-surface on-shore CSEM modelling and inversion involve additional challenges. Steel-cased boreholes—especially if a large number of them are present as in a producing oil field—are likely to distort CSEM (and other EM) signals in the subsurface (Tietze et al. 2015b; Patzer et al. 2017). The extreme resistivity contrast from steel casing to surrounding material and different spatial scales make the 3-D modelling a non-trivial task and require advanced numerical modelling (Yang et al. 2009; Commer et al. 2015). A realistic representation of the steel casing requires extremely small cells of about 1 cm, while the largest cells of the domain are hundreds of metres thick and the conductivity contrast between steel and air exceeds 12 orders of magnitude (Vilamajó et al. 2016). The dimension of the highly ill-conditioned system matrix that captures all effects near the casing and far away from it exceeds 5–6 million and requires distributed memory computing systems (Puzyrev et al. 2016). On the other hand, borehole-to-surface on-shore CSEM measurements use the propagation of the electric field along the steel casing to enhance resolution for deeper targets (e.g., Tang et al. 2015; Tietze et al. 2015b; Vilamajó et al. 2015, 2016; Patzer et al. 2017). Therefore, including steel casing correctly in the model improves the misfit and enhances the detection of layers and structures and hence is certainly a future challenge for 3-D EM inversion of real data (see Sect. 5).

3.2.3 Strategies to Reduce Mesh-Related Computational Demands

Lindsey and Newman (2015) described a so-called sequenced workflow for 3-D MT inversion that uses fewer computational resources than standard approaches and at the same time retrieves a better-fitting 3-D resistivity model of geothermal systems. They introduced a two-step approach. At first, they only considered low-frequency data (i.e.

$f < 1$ Hz) and inverted them using a coarse mesh and a homogeneous initial model to fit the data to a level of RMS < 2. Note that they did not observe advantages when aiming for a better fit. In the preparation for the next step, they refined or re-parameterized the resulting model onto a finer mesh. As the refinement adds additional nodes to the mesh, the assigned values of those new nodes are based on interpolated or averaged resistivity gradients of the coarse mesh. This refined solution of the first step is used as initial model and mesh for the second step, namely the inversion of the entire data set (high and low frequencies). Figure 5 shows a comparison of two 3-D MT inversion results of the Krafla geothermal field, Iceland, using standard work flow (A) and their sequenced workflow (B). The model based on the standard workflow fails to image the relatively more resistive fractured reservoir at 1–3 km depth. It also does not show the electrically conductive pathway that Gasperikova et al. (2011) interpreted as conduit supplying the magma encountered by a deep well of the Iceland Deep Drilling Project (IDDP). On the other hand, Lindsey and Newman (2015) retrieved a geologically consistent model using their sequenced workflow, which images both the magmatic conduit and the resistive core of the geothermal reservoir.

Field data have to be rotated to align with the inversion coordinate system. Commonly this rotation is done to align the x-axis of the inversion coordinate system with geographic north, but Tietze and Ritter (2013) also tested a mesh with the x-axis aligned with the geo-electric strike (see Fig. 3). A positive effect of the alignment with geo-electric strike direction is that the grid better aligns to the site layout, and therefore, fewer cells are required. While these two strategies are applicable to any 3-D inversion code as they are based on changes of inputs, there are also codes that have hardwired solutions implemented to solve meshing demands.

Similar to the idea by Lindsey and Newman (2015) is the nested mesh approach implemented in ModEM (described and first applied to real data by Meqbel et al. 2014). The nested mesh approach is used to avoid meshes with a huge number of cells but at the same time warrant a fine enough mesh at the area of interest and prevent boundary effects. Therefore, a coarse, large-scale mesh is used to compute the regional electric field. Then, this electric field is imposed as boundary condition and initial model to a much smaller

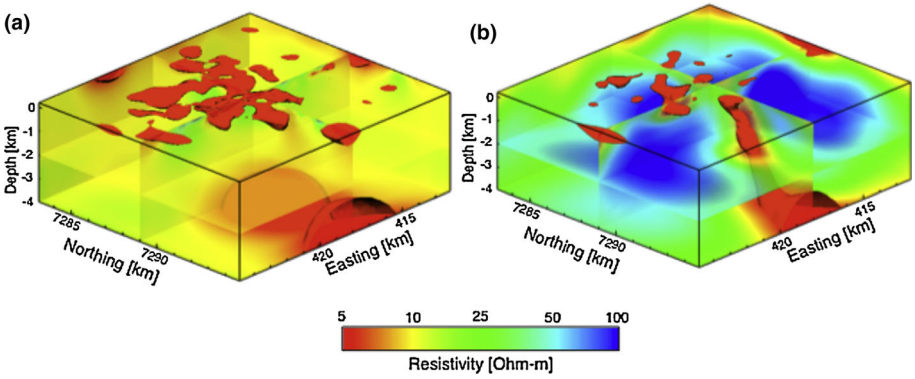

Fig. 5 Comparison of 3-D inversion results of MT data recorded at Krafla geothermal field, Iceland, obtained by (**a**) a standard inversion workflow and (**b**) a sequenced workflow (reprinted from Lindsey and Newman 2015 with permission from Elsevier). Neither the resistive core of the geothermal reservoir nor the strong electrically conductive ascending pipe feature (interpreted as source of the magma encountered in the deep IDDP well) is retrieved by the standard procedure but by the sequenced workflow based on a two-step approach (see Sect. 3.2.3)

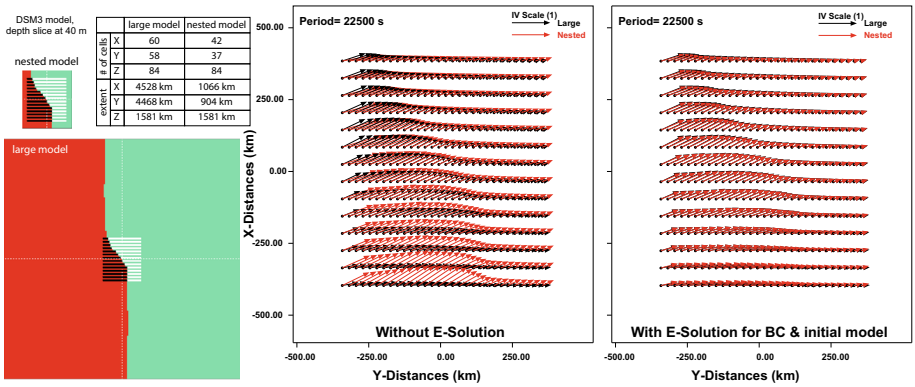

Fig. 6 Example to illustrate effects of too close mesh boundaries and the advantage of the nested mesh approach (pers. com. Naser Meqbel; shown at ModEM training course, Bari, Italy, 15 May 2016). The model is the DSM3 model of the MT3DINV3 Workshop 2016 in Bari, Italy (Jones et al. 2016), and a depth slice at 40 m is shown on the left—once as large mesh and once as small/nested mesh. The table lists the specifications of both meshes. The middle and right show VTF data as induction vectors (IV) in black for the large mesh and red for the small/nested mesh. Results obtained using just the small mesh without any additional information (middle) show obvious discrepancies. Using the nested mesh approach (right), i.e. calculating the electric regional field on the large mesh and use those fields as boundary condition (BC) and initial model for the small/nested mesh, clearly improves the results

mesh—not much larger than the area of interest—with smaller cells. Figure 6 shows an example based on the DSM3 model of the MT3DINV3 Workshop 2016 in Bari, Italy (Jones et al. 2016). Both the large and the nested model are with respect to each other shown to scale, and the table lists the mesh specifications (Fig. 6 left). A comparison of predicted VTF data based on using both meshes just as they are (without the nested mesh approach) clearly shows the boundary effects caused by a too small mesh (middle). If the small/nested mesh is used, applying the regional electric field as boundary condition and initial model avoids such boundary effects (right). Boundary effects are of course a matter of the combination of used period and distance to the edge of the mesh. The closer the boundary and/or the longer the period, this effect increases. A similar effect can be observed for impedance data too (especially the long period), which is not shown here.

An approach to overcome meshing issues from the numerical/code implementation side is the adaptive finite-element method by Grayver (2015), an approach Key and Ovall (2011) demonstrated to be efficient for 2.5D. He adopted an automatic mesh refinement algorithm based on a goal-orientated error estimation to avoid a subjective and interminable process of finding a suitable model parameterization. The meshes of forward and inverse problems are decoupled to prevent over-parameterization. This approach refines the mesh where needed—in fact without prior assumptions about model parameterization—instead of using small grid sizes for the entire central part of the mesh and it also considers the different spatial characteristics of the EM fields over a wide range of frequencies (i.e. independent mesh refinement for all frequencies).

3.2.4 Validation of Model Discretization

Long computing time and large memory requirements are—unfortunately—very common excuses to disregard careful mesh testing. Therefore, if the area of interest is large and, hence, the required mesh is large too, it can be very useful to consider either a subset of

sites and/or individual frequencies separately to perform thorough mesh tests on a smaller scale. Such an approach reduces calculation time and memory requirements and enables the user to learn how to handle the code and the particular data set.

Grayver et al. (2014) verified the quality of their grid by comparing a 3-D CSEM numerical solution to a 1-D quasi-analytical solution for a layered model. In a similar manner, one can use homogeneous or layered half-space models to forward calculate MT responses and compare them to 1-D and 2-D solutions. It is of course important to select realistic resistivity values for such half-spaces to ensure a reliable conclusion about the influence of boundary effects and cell sizes.

3.3 Initial and Prior Models

As the inverse problem is non-unique and has limitations in sensitivity and resolution, approaches to integrate independent information are required. The review by Bedrosian (2007) discusses the different aspects and levels of integration of various information in detail. He distinguishes between the following types—(1) qualitative, post-analysis (i.e. data analysis and inversion are not affected but information is used to interpret the results, see Sects. 3.8 and 4), (2) hard and (3) soft a priori constraints (e.g., resistivity models included in the inversion process) and (4) constrained multi-property inversion [will be discussed in detail in the review by Moorkamp (2017)] and post-inversion structure classifications. The hard and soft a priori constraints are implemented in the resistivity model used for inversion—either as fixed parameters or as not explicitly fixed model parameters such as changes in regularization or spatially varying structure constraints, respectively (Bedrosian 2007).

There are two different types of resistivity models: firstly, a model is required to get the inversion process started—known as starting or initial model (in the following called initial model). Secondly, there is a model that is part of the model objective function and that is used to regularize against—called prior, reference or preferred model (in the following called prior model). Depending on the used inversion code at least an initial model is required and often an additional prior model is used (e.g., ModEM by Egbert and Kelbert 2012; Kelbert et al. 2014). Most of the recent 3-D inversion codes populate the prior model—if not specified separately—from the initial model (i.e. initial and prior model are identical). This feature cannot be turned off. Those models are 'prejudice models'—as J. Booker called them at the MT3DINV3—and bear a risk. While wisely chosen models can enhance the fitting and improve the inversion result, erroneous models can steer the inversion into the wrong direction. That means the inversion can be forced to focus on a specific cluster of inverse models matching the prior model (not necessarily the truth) but ignores all other clusters of inverse models that might fit the data as well but do not satisfy the prior model.

For both initial and prior models, a fundamental consideration is that the model is free of major artefacts, i.e. features which are false (Holtham and Oldenburg 2012). While conductivities from down-hole measurements can provide valuable information, one must carefully decide whether these values are representative for features at the size of the applied discretization or not. If trustworthy a priori information about geological structures and/or rock properties or additional information from other geophysical investigations is available, they can be incorporated into the models. In cases where limited or no information is available, generally a simple model should be chosen (Holtham and Oldenburg 2012). The simplest model has a uniform conductivity distribution, i.e. the best fitting homogeneous half-space. For some methods (e.g., MT) merging resistivity models

generated by 1-D or 2-D inversions to a 3-D model is another option that can improve the inverse model (e.g., Ivanov and Pushkarev 2012). For other data sets such as ZTEM (Z-Axis Tipper EM), this approach suffers from the zero vertical magnetic fields for all 1-D layered models (Holtham and Oldenburg 2012).

VTF data alone can only recover the horizontal position and lateral resistivity contrast but not the vertical position and absolute resistivity value of the anomaly (e.g., Siripunvaraporn and Egbert 2009). Therefore, it is obvious that the final model is biased towards the initial and prior models and the recovery of the correct resistivity structure is improved by models close to the real background resistivity (e.g., Siripunvaraporn and Egbert 2009; Tietze and Ritter 2013; Padilha et al. 2015). Some control on the absolute resistivity values is required and needs to be obtained from other methods such as MT impedance data, or other a priori information. Similarly, phase tensor inversion can recover the regional conductivity structure (even in the presence of galvanic distortion) if the initial and prior models provide a reasonable assumption for the regional resistivity average (Tietze et al. 2015a). Performing a joint inversion of phase tensor data and VTF, they found better recovery of the absolute resistivity structure with less dependence on the prior model.

In general, it is obvious that the resistivity level of the initial and prior models can have an influence on the resulting inverse model and that, at poorly constrained parts of the model, the inversion tends to keep or return to the assumed resistivities provided by the models (e.g., see Fig. 9). To validate the sensitivity of a particular model feature, the inversion results using different initial and prior models (e.g., different homogeneous half-space models) should be compared (e.g., Kelbert et al. 2012; Tietze and Ritter 2013; Lindsey and Newman 2015; Jegen et al. 2016; Ślęzak et al. 2016).

Otherwise homogeneous initial and prior models should at least comprise topography and bathymetry and treat air and water with appropriate resistivity values. In general, initial and prior models allow to include information such as oceans (e.g., Heise et al. 2010; Thiel and Heinson 2013; Tietze and Ritter 2013; Jegen et al. 2016) and other geological information (e.g., vertical and lateral extent and average resistivity of a sediment layer (e.g., Jegen et al. 2016) or other geological units or a saline near-surface aquifer [e.g., Ślęzak et al. 2016)]. Especially, if—due to poor site distribution—the constraints from the data are lost or if dominant off-profile features (e.g., ocean) are present, inclusion in the initial and prior models can minimize the artefacts. In certain circumstances, e.g., a continental shelf with shallow bathymetry (< 100 m) for the first few kilometres off the coast line, the coast effect only affects long-period data (e.g., Miensopust et al. 2014) but, in general, a nearby ocean should be included in the initial (and prior) model using known bathymetry and a constant resistivity. It also has to be considered which ocean or sea is affecting the inversion, while most oceans are represented by about 0.3 Ωm, for instance, the more conductive Dead Sea requires 0.2 Ωm (Meqbel et al. 2016). Commonly, the ocean is kept fixed during the inversion procedure (Padilha et al. 2015), while other features are usually—to some degree—variable.

Jegen et al. (2016) used a mesh including the bathymetry for their Walvis Ridge data, but the inversion using a homogeneous half-space with ocean included failed to converge. Only if they included a 3-km-thick 1 Ωm sedimentary layer, they successfully fitted their data and obtained a reasonable RMS value of 2.27 (see Fig. 7). Similarly, Thiel and Heinson (2013) found for on-shore MT data that shallow features are strongly dependent on the chosen model (e.g., information of sedimentary basins in the prior model), and Tietze and Ritter (2013) observed artefacts and misleading structures if the true resistivity distribution includes strong contrasts (i.e. strongly differs from simple initial and prior models). Increasing the mantle conductivity of the prior model, Kelbert et al. (2012)

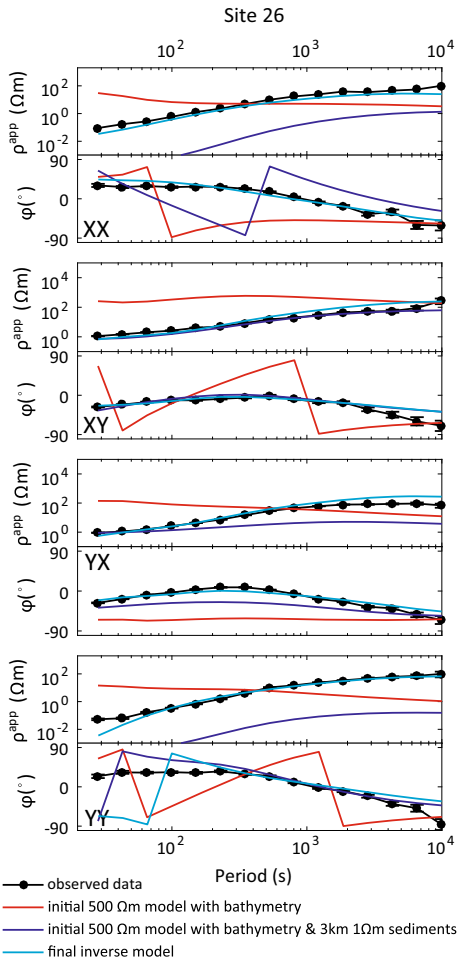

Fig. 7 Good quality MT data (black) of an example site from the amphibian data set at the Walvis Ridge of the Namibian coast. If the initial model only includes the bathymetry (red), the 3-D inversion does not converge. Including the sedimentary layer (dark blue) the inversion succeeds with a reasonable data fit (cyan) and RMS of 2.27 (modified after Avdeeva et al. 2016; Jegen et al. 2016 with permission from Elsevier)

observed an upwards shift of conductive features by up to 10 km for a regional scale setting. Patro and Egbert (2011) used homogeneous initial and prior models, ran the inversion for three to four iterations and then used the model of the iteration with minimum RMS misfit as a new prior model to restart the inversion for another two iterations. Using this two-step approach they found the results generally better fitting than without restart; not a surprise as they adjust the prior model to the requirements of the data set (i.e. a smooth version of the final model is mitigating the effects caused by firstly penalizing against an inadequate model).

Löwer (2014) demonstrated that oceans are not the only features that influence data at sites located aside. He systematically investigated the influence of resistivity anomalies with different lateral distances to the observation location and found that local near-surface structures required to fit the high-frequency data at one site can have a regional influence on the low-frequency data at another site. His forward modelling studies showed that VTF data from the Vogelsberg, Germany, could only be approximated if the north German sedimentary basin—although far off the area of interest—was included in the model, while the influence on the phase tensor and impedance data were negligible.

Meshes designed for large penetration depth (e.g., lithospheric MT studies) should include known boundaries such as the 410 and 660 km discontinuities. Based on mantle conditions and minerals (Xu et al. 2000) and supported by observations (Kelbert et al. 2009; Khan and Shankland 2012), a low resistive half-space below 660 km is a commonly used assumption [e.g., Booker et al. (2004); Burd et al. (2014) used 3 Ωm, although global induction studies determined an even lower resistivity of 0.5–1 Ωm (e.g., Constable 1993; Olsen 1999)]. Associated with the olivine to wadsleyite phase transition at the upper mantle transition zone is a substantial decrease in resistivity (Yoshino and Katsura 2013), thus an expected discontinuity at 410 km which is by some studies included as tear (e.g., Burd et al. 2014).

Other geophysical methods can also provide additional information; for example, sharp seismic horizons can be inserted as tear surfaces in the model, if the exact depth and lateral extent are known. However, be aware that things might be mixed up, when trying to match the sharp boundary velocity model and the smooth inversion EM model. Benefits and challenges of joint inversion are discussed in more detail by Moorkamp (2017).

Scholl et al. (2015) presented a different approach to make use of a priori information. They successfully applied additional regularization based on a cross-gradient concept after Gallardo and Meju (2003) to introduce known geological structures to the inversion of airborne EM data. The cross-gradient approach is a known concept for joint inversion of different geophysical methods and supports structural similarity between two otherwise independent models. Scholl et al. (2015) built a model based on geological a priori knowledge (e.g., the dip) and applied the cross-gradients to steer the inversion towards the structural similarity to this model. To achieve this, an additional regularization term is required that defines the direction of change, but neither the strength of change nor if it increases or decreases in that direction. Hence, an arbitrary numerical value can be used to set up the steering model—which is a huge advantage over initial and prior models! Figure 8 shows an example of geo-steered inversion of airborne EM data of the Maimon

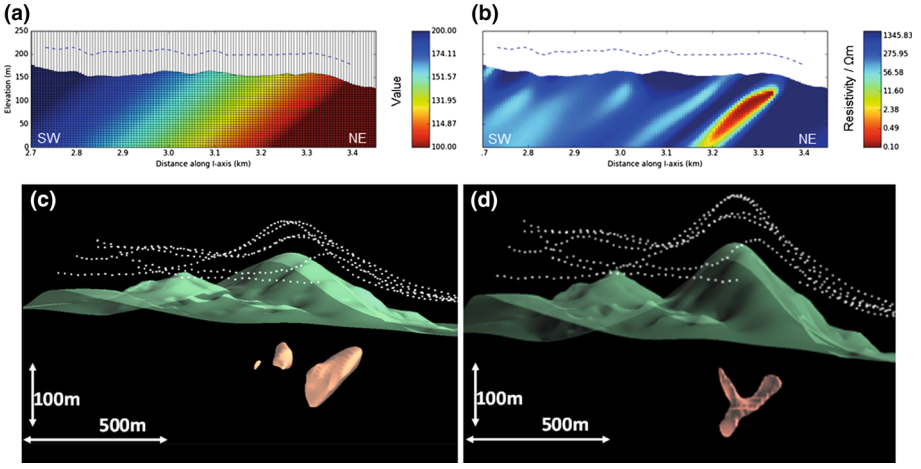

Fig. 8 Geo-steered 3-D inversion of airborne EM data of the Maimon orebody, Dominican Republic, after Scholl et al. (2015). The steering model (**a**) is a model of arbitrary numerical values with 45° dip based on the observed regional geological dip (Roos et al. 2007). The inversion result defines a SW-dipping conductor (**b** profile view; **c** conductive body of < 1 Ωm), plunging to the SE. For comparison, the conventionally regularized inversion is shown (**d**). (**c**, **d** white dots—flight path; green surface—topography)

orebody, Dominican Republic. Scholl et al. (2015) used a steering model of arbitrary numerical values based on the regional geological dip (A) and obtained a 3-D inversion result (B and C) that outmatches the result based on conventionally regularized inversion (D). Introducing this simple structural model increased the geological plausibility, i.e. it is in good agreement with the geological section, and the effective resolution.

3.4 Inversion Parameters

To stabilize multidimensional inversion of EM data, regularization is required and commonly a smoothness criterion is applied which often results in uniformly blurred features that tend to not appear geologically meaningfully. Compared to 1-D and 2-D inversion, 3-D inversion has many more degrees of freedom and therefore requires particularly robust stabilizing functions. It is challenging to prevent the inversion from placing many resistivity variations in the model where little constraints from data are available, for example outside the site coverage or in gaps between sites. Holtham and Oldenburg (2012) suggested initially inverting the data on a coarse mesh to ensure that the data and inversion parameters have been set correctly. Thus, it is possible to carry out multiple inversions in a reasonable time to explore possible parameters. While those tests are standard procedure for 1-D and 2-D, it seems that 'this wheel has to be reinvented' for 3-D, but slowly it becomes more and more common practice.

Usually one has to define a starting value for the regularization parameter λ, also known as Tikhonov regularization operator, and a scale of reduction of λ. Meqbel et al. (2016) stated that for ModEM rapid or continuous changes of the regularization parameter λ can result in a loss of orthogonality of the search direction vector in nonlinear conjugate gradients (NLCGs) algorithms. On the other hand, keeping λ as fixed value can cause the NLCG algorithm to get stuck in local minima. Therefore, Meqbel et al. (2016) used $\lambda = 1$ to start the inversion, and if the difference between data misfit (in terms of RMS) of the current and previous iteration is below a certain threshold (e.g., < 0.002) λ is decreased by a factor of ten. This procedure ensures that the orthogonality of the search direction vector is maintained and the NLCG algorithm can escape from a local minimum. Using the massively parallelized EMGeo algorithm, Lindsey and Newman (2015) started with $\lambda = 1.25$ and made a 50% reduction if the NLGC algorithm stalls in its line search and reset λ after mesh refinement.

Additionally, there are smoothing parameters—for example WSINV3DMT by Siripunvaraporn et al. (2005a) requires four smoothing parameters. The time step parameter is usually set to default (i.e. $\tau = 5$; e.g., Heise et al. 2010; Thiel and Heinson 2013). The other three parameters define the smoothing in lateral and vertical direction, i.e. the smaller the model length scale δ, the rougher the resulting model. Thiel and Heinson (2013) used a uniform starting $\delta = 0.3$ which is reduced to 0.1 for the final step, whereas Heise et al. (2010) chose a constant $\delta_z = 0.1$ but compared results of different $\delta_x = \delta_y = 0.2$, 0.3 and 0.4 yielding to models with less smoothness in z-direction compared to the lateral directions. They found that the smallest value resulted in the lowest RMS value, but the model appeared unreasonably rough at shallow depth levels, while the largest value did not match the phase tensor data as well as the model with the intermediate roughness. As Patro and Egbert (2011) align their mesh with the geo-electric strike direction, they can use the model length scale to promote smoothing and longer structures along strike. Figure 1 shows the comparison of (a) isotropic (i.e. $\delta_x = \delta_y = \delta_z = \sqrt{2}$) and (b) anisotropic (i.e. $\delta_x = \delta_z = \sqrt{2}, \delta_y = \sqrt{10}$) model covariance values. The observed

model using the anisotropic model length scale tends to be more elongated structures along strike—as expected—but also to be significantly higher conductivities (about factor 3). They report that the anisotropic result has slightly larger misfit, it is rougher, and it has larger amplitude anomalies, suggestive of over-fitting within the constraints imposed by the model covariance. Note that the model length scale is defined in terms of grid cells rather than physical length units and therefore is dependent on the model discretization used. It depends on the code used if the size of grid cells is compensated for or not.

Similarly, determining appropriate smoothing parameters in ModEM is crucial as they depend on many factors including cell size (Meqbel et al. 2016). Ślęzak et al. (2016) found that for their data set from northwest Poland using ModEM smoothing parameters of 0.3 for all directions resulted in a conductive area placed only in the top few layers. Continuously modifying the lateral values from 0.7 to 0.5 and setting the z-direction to 0.7 achieved the best result. Tietze and Ritter (2013) used horizontally isotropic smoothing for the mesh in geographic coordinate system, and for the strike-aligned mesh, they increased smoothing parallel to strike. Yang et al. (2015) also tested different smoothing strategies using ModEM for EarthScope data from the north-central USA (Schultz et al. 2006–2018, 2008–2013). Figure 9 shows their preferred inverse model (a–c) and an inverse model based on uniform smoothing applied to all parts of the mesh (d–f). For the preferred inverse model the smoothing was reduced for layers shallower than 2 km, resulting in isolated high and low resistivities producing a spotty image of the near-surface structures. This reflects the weak sensitivity of the MT data to near-surface resistivities between the widely spread sites and is caused by the regularization approach which penalizes differences from the prior model (in this case a 100 Ωm half-space). Static distortion and the strategy to reduce smoothing to better fit near-surface effects exacerbate this problem (compare a and d). Nevertheless, the conductance map shows strong consistency with known surface geological features such as the Michigan Basin (subsided for 500 m.y. and accumulated about 4 km of Phanerozoic sediments at its centre; Sleep and Sloss 1978) and the Illinois Basin (up to 6 km Palaeozoic sediments; Heidlauf et al. 1986). Although the conductance map of the uniform smoothing (d) looks more pleasing, the spotty image of the reduced smoothing is more honest but you must know how to read and interpret it. Additionally, the uniform smoothing introduces more artificial low resistive structures at greater depth—especially outside the area covered by sites. This example by Yang et al. (2015) clearly illustrates that a thoughtful and responsible handling of smoothing parameters and the interpretation of the resulting models is essential.

Another approach is to define the structure penalty in all spatial directions increasing with depth, as the diffusive physics of MT causes decreased spatial resolution with depth (Burd et al. 2013, 2014). One could also consider applying bounds on the conductivities to enforce realistic values in the inverse model. However, no matter which approach is used, exploring the parameter settings thoroughly (probably by trail and error) is required.

3.5 The Distortion Challenge

Earlier reviews by Jones (1983) and Jiracek (1990) discuss in detail the sources and effects of current channelling and distortion due to resistivity inhomogeneities but also topographic effects. In general, distortion comprises all the small-scale, near-surface conductivity inhomogeneities and topographic effects that cannot be resolved with the conductivity model of the subsurface, but still affect the data, i.e. distort them. The process of distortion is complex and can be distinguished into galvanic and inductive effects each of which influence the electric but also the magnetic fields (Berdichevsky et al. 1973;

Berdichevsky and Dmitriev 1976b). Those individual contributions as well as assumptions and their limitations are discussed by many authors (e.g., Berdichevsky and Dmitriev 1976a, b; Jones 1983; Chave and Smith 1994; Chave and Jones 1997; Smith 1997; Garcia and Jones 2002). If station spacing and model discretization used are too coarse to image the small-scale near-surface resistivity heterogeneities, the MT responses at deeper depth levels are distorted. One approach is to remove this distortion from the impedance tensor before inversion, and another one is to consider distortion during inversion.

A detailed, recent compilation on identification and removal of distortion of MT data is given by Jones (2012). An early idea was to correct MT data for static shift using transient EM (TEM) data (Sternberg et al. 1988; Pellerin and Hohmann 1990; Sternberg and deGroot 1993). While this highly controversial approach persists in geothermal exploration (Árnason et al. 2010; Árnason 2015), Urzúa-Monsalve (2008) reviewed data collected and interpreted by companies and researchers worldwide and found that unreliable MT static shift correction based on misleading TEM data is common in geothermal prospects with thick resistive rocks at the surface (e.g., Cascades of western USA, rhyolite lava fields in New Zealand). Although the focus of TEM is more on vertical resistivity variations, the data can be distorted by large lateral contrasts (Wilt and Williams 1989). Additionally, TEM data can be affected by induced polarization effects (e.g., Lee 1981; Raiche et al. 1985; Fitterman and Stewart 1986), superparamagnetic effects (Buselli 1982) and topographic effects (Stark et al. 2013; Watts et al. 2013). Furthermore, Cumming and Mackie (2010) discovered that the static shift correction depends on the TEM equipment used.

Another approach to correct for static shift is based on the identification of 1-D sections within the MT response curves at short periods (Bibby et al. 2005; Heise et al. 2010). Nevertheless, no matter which approach is applied it remains questionable whether using EM data to check and correct other EM data for static shift distortion is appropriate. It is better to consider other constraints if possible. Furthermore, with high-resolution topographic data (e.g., airborne LiDAR Stark et al. 2013) and modern 3-D modelling capabilities, there should no longer be an uncertainty about distortion of MT data due to terrain.

If distortion of non-topographic origin is present, it needs to be addressed otherwise. For 2-D, Groot-Hedlin (1991, 1995) tried to simultaneously invert for the resistivities and static shift, assuming that for a large area the sum of all shifts on log-scale is zero, or the full electric galvanic distortion matrix to find the smoothest model. Another approach by Ogawa and Uchida (1996) was to assume a Gaussian distribution around zero for the log of the shift multipliers. Nowadays, similar approaches are under development for 3-D (e.g., Miensopust 2010; Avdeeva et al. 2015).

Patro and Egbert (2011) found that even if site density and cell sizes are not sufficient to resolve distorting near-surface structures, features are inserted in the surface layers during full 3-D inversion to fit distorted data. Conductive and resistive features generally with peak amplitudes off-profile and restricted to the upper few layers effectively fit site-to-site variations in impedance amplitudes and also produce diagonal impedance elements due to the effects on the current flow and, hence, on the electric field. Nevertheless, Patro and Egbert (2011) mentioned that their data are not substantially distorted and that severely distorted data (e.g., phases out of quadrant, mode splits of several orders of magnitude) require more explicit treatment.

Cumming and Mackie (2010) found that 3-D MT inversion codes inverting for static shift effects based on smoothness of the model are an effective tool in sedimentary basins. Nevertheless, in the volcanic highlands of the Glass Mountain area, USA, their 3-D MT inversion with static smoothing caused geological elements important to the interpretation to be overly smoothed.

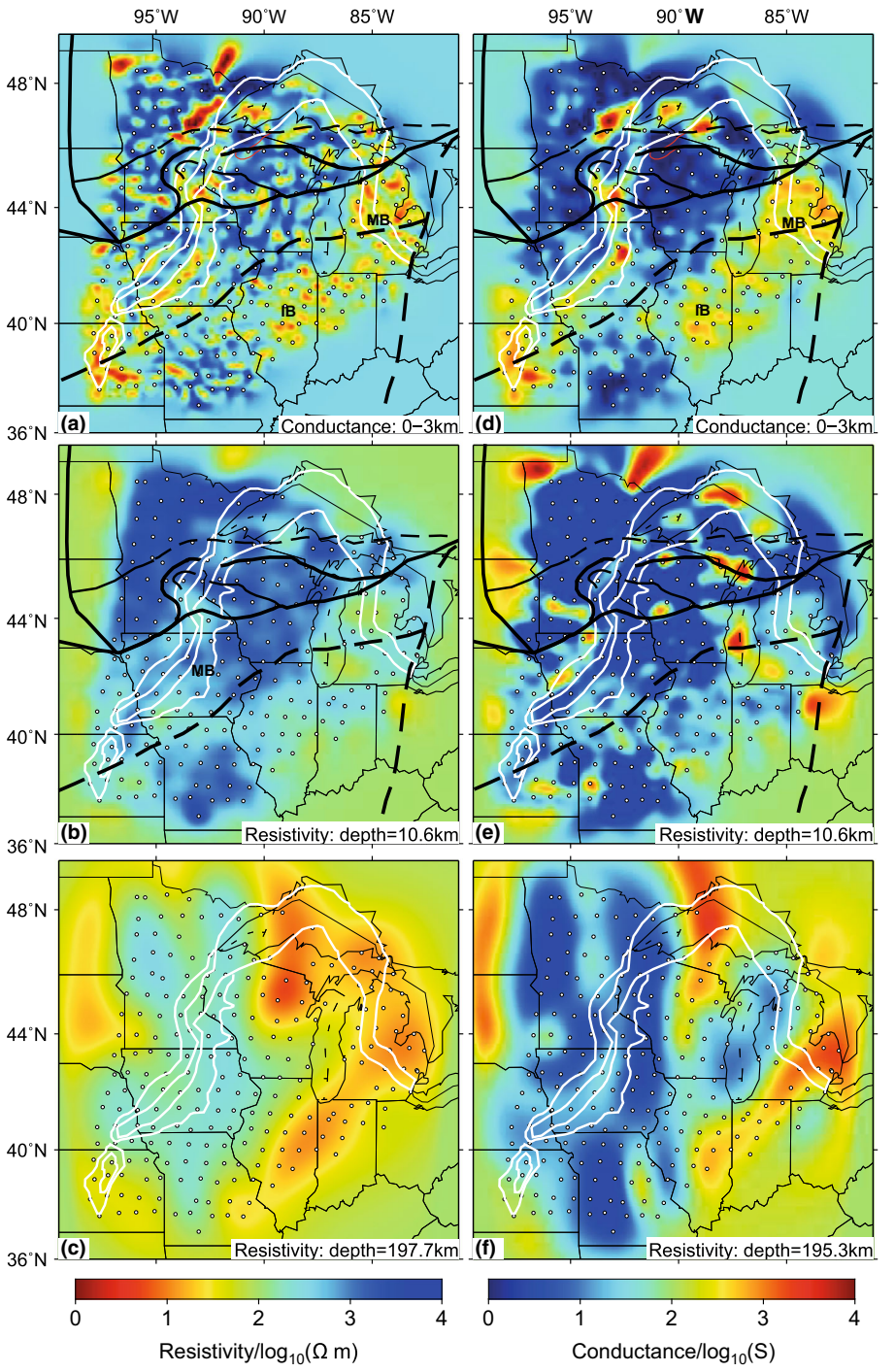
95°W
90°W
85°W
48°N
44°N
40°N
36°N
MB
IB
(a) Conductance: 0–3km
(d) Conductance: 0–3km
(b) Resistivity: depth=10.6km
(e) Resistivity: depth=10.6km
(c) Resistivity: depth=197.7km
(f) Resistivity: depth=195.3km
0 1 2 3 4
Resistivity/log10(Ω m)
Conductance/log10(S)

◀**Fig. 9** Resistivity 3-D inverse models of the north-central USA from EarthScope long-period MT data (modified after Yang et al. (2015) with permission from Elsevier and G. Egbert, ModEM training course, 15 May 2016, Bari, Italy). Note that for the depth range 0–3 km (**a**, **d**) the conductance (i.e. vertical integrated conductivity) is shown. The left column (**a**–**c**) shows inversion models obtained using reduced smoothing in layers shallower than 2 km, whereas on the right (**d**–**f**) the same smoothing was applied at all depth levels. While the former produces rougher shallower structures, it results in slightly smoother and simpler deep structures. White lines indicate the Mid-Continent Rift, and MT site locations are marked by white circles. Tectonic zones and terrane boundaries are indicated by black outlines (IB: Illinois Basin; MB: Michigan Basin)

To invert for resistivity structure and distortion parameters simultaneously, inversion strategies suggested (e.g., by Miensopust 2010; Avdeeva et al. 2015) consider only the electric galvanic distortion, which is a frequency-independent, real 2×2 matrix per MT site. Note that for higher frequencies the distortion is no longer frequency independent as the magnetic distortion comes into play. One should be aware of this limitation of the approach. Similarly, to joint inversion, the objective function is extended by an additional term describing the measure of closeness to reference distortion parameters (often identity matrix, i.e. undistorted data) with an additional weighting term. Other than 'classic' joint inversion, in this case two models—the distortion matrix and the resistivity model—are manipulated to fit one data set rather than changing one model to fit two independent data sets. This leads to a slightly different objective function compared to 'classic' joint inversion and implies a trade-off between fitting the data using distortion parameters and the resistivity model. Avdeeva et al. (2015) demonstrated the applicability of this approach using the synthetic test data set DSM2 generated for the MT3DINV Workshop II (Miensopust et al. 2013). The data set is based on the COMMEMI 3D-2 model (Zhdanov et al. 1997) with a few modifications and was contaminated with random galvanic distortion and 5% Gaussian noise [for more details on the data set or to download it, see Miensopust et al. (2013)]. Figure 10 shows slices of the true model and inversion results of standard inversion of undistorted, noise-free data as well as of distorted, noisy data, and finally, of the simultaneous inversion for resistivity structure and distortion matrix of distorted, noisy data. Additionally, a comparison of the predicted and observed distortion matrix elements at all sites obtained by the latter inversion is shown. Clearly, the algorithm by Avdeeva et al. (2015) recovers the resistivity structure and the underlying distortion parameters well, if they are jointly inverted for. Without such an approach to account for the distortion during the inversion, the resulting resistivity model is dominated by artificial structures.

This approach and code has also been successfully applied to a real data set from the Kemaliye geothermal field, western Anatolia, Turkey (Avdeeva and Moorkamp 2015; Moorkamp et al. 2016). Figure 11 shows the resistivity model obtained by standard inversion without considering distortion (top) and by simultaneous inversion for resistivity structure and distortion parameters (bottom). The near-surface depth slice (left) clearly shows that ignoring distortion results in numerous spurious structures, which can significantly be reduced when distortion is considered. Additionally, the vertical section (right) shows that including distortion in the inverse process results in a better agreement of the model with boundaries known from boreholes. In general, Avdeeva and Moorkamp (2015) and Moorkamp et al. (2016) concluded that this approach results in better recovery of structures and less artefacts for the near-surface compared to inversion without.

Recently, Patro et al. (2013) and Tietze et al. (2015a) implemented phase tensor inversion in the widely used codes WSINV3DMT and ModEM, respectively. The phase tensor is unaffected by galvanic distortion but provides only little information about the

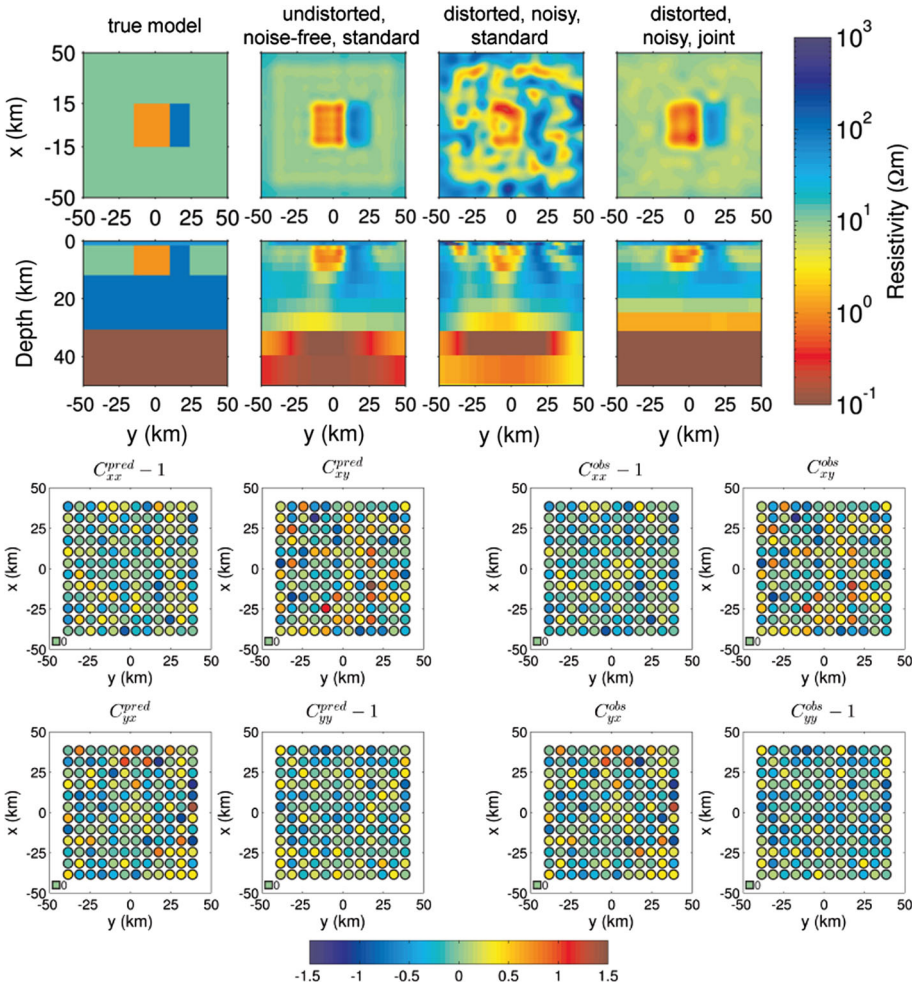

Fig. 10 Comparison of inversion results of the DSM2 (Miensopust et al. 2013) data set (modified after Avdeeva et al. 2015). Top: horizontal slices at 3 km (first row) and vertical cross section (second row) through the centre of the resistivity model; from left to right: true model, standard inversion of undistorted, noise-free data, standard inversion of distorted, noisy data and simultaneous inversion for resistivity structure and distortion matrix of distorted, noisy data. Bottom: comparison of the four predicted (left) and observed (right) distortion matrix elements at all sites corresponding to the simultaneous inversion (top; last column)

absolute resistivity values as it—analogous to VTFs—describes only variations of the conductivity structure (Caldwell et al. 2004). Therefore, the conductivity structure of the initial (and prior) model has a huge influence on the resulting inverse model (as discussed above). Both Patro et al. (2013) and Tietze et al. (2015a) show synthetic studies that illustrate the effects of various initial resistivity distributions on the resulting model. They also found—for synthetic as well as real data—that if the initial model is close to the true model, phase tensor inversion of galvanic distorted data could recover the regional structure better than impedance inversion. To obtain an adequate initial model, undistorted EM data can be useful. Even the MT survey data itself can be used to get some rough idea

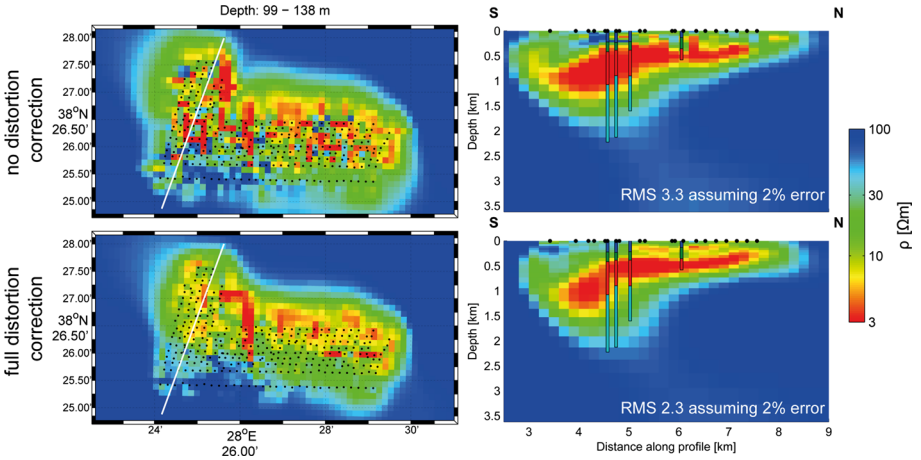

Fig. 11 Real data example of simultaneous inversion for resistivity structure and distortion matrix—Kemaliye geothermal field, western Anatolia, Turkey (modified after Moorkamp et al. 2016). A near-surface depth slice (left) and a vertical section (right; marked as white line in depth slice) show the obtained resistivity model based on standard inversion without distortion correction (top) and simultaneous inversion for resistivity and distortion (bottom). Considering distortion reduces near-surface artefacts and results in better fit to borehole information

considering 'average' impedances to narrow the range of suitable initial models (e.g., Heise et al. 2008; Patro et al. 2013; Tietze et al. 2015a). Although phase tensor and VTF both poorly constrain the absolute resistivity values, their combination of sensitivity to vertical and lateral resistivity variations, respectively, provides a superior resolution and a better recovery of the absolute resistivity structure (Tietze et al. 2015a).

3.6 Large Data Sets

When data sets are too large (e.g., exceed available memory, unacceptable long computing time), the inverse problem must be reduced in size. There are different approaches available. Some of them are 'outside' the inversion and concern the reduction of the input data. Others are numerically integrated into the actual inversion or meshing procedure. For natural-source and land-based data, this problem is known, but it is by far more obvious when considering controlled-source methods and, especially, airborne EM data as the data point spacing along flight lines is small (i.e. a few metres) and an entire data set easily comprises several hundred thousand of locations.

Since full 3-D inversion of an entire multi-frequency airborne EM data set is still extremely time-consuming and numerically expensive, the standard procedure is to perform a 1-D inversion at each data point and to stitch them together (e.g., Sengpiel and Siemon 2000) or perform lateral (Siemon et al. 2009) or spatial (Viezzoli et al. 2008) constrained 1-D inversions. Especially at areas of strong lateral conductivity contrast, this is a rather poor compromise. Therefore, Ullmann et al. (2016) developed a new algorithm for automated identification and extraction of induction anomalies in airborne EM data sets, which allows to combine rapid 1-D and accurate 3-D inversion, performed only at those parts where 1-D is not sufficient. Based on the individual apparent conductivity maps for each frequency, they calculate the gradient magnitude as a measure for spatial change in conductivity. Applying hysteresis thresholding, they first identify areas of strongest

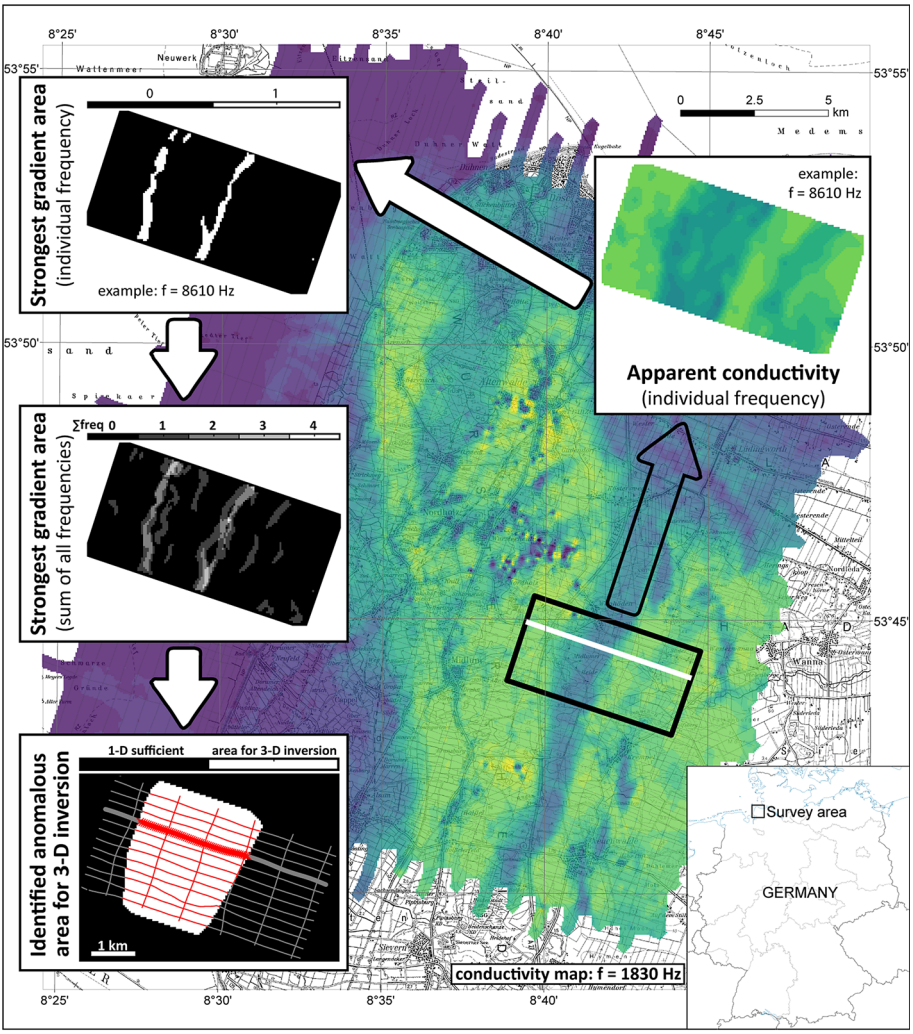
Strongest gradient area
(individual frequency)
example: f = 8610 Hz
Strongest gradient area
(sum of all frequencies)
Identified anomalous
area for 3-D inversion
1-D sufficient
area for 3-D inversion
1 km
example:
f = 8610 Hz
Apparent conductivity
(individual frequency)
Survey area
GERMANY
conductivity map: f = 1830 Hz
pure 1-D inversion
combined 1-D/3-D inversion
Elevation [m asl]
Distance [m]
NW
SE
1-D
3-D
1-D
σa [Sm-1] 0.0005 0.005 0.01 0.0154 0.025 0.04 0.0667 0.1429 0.3333 1.0

◀**Fig. 12** Example of the cut-and-paste 3-D inversion of airborne EM data (modified after Ullmann et al. 2016 with permission from Elsevier). Top: background apparent conductivity map ($f = 1830$ Hz) of the Cuxhaven tunnel valley at the German North Sea Coast (inlay: overview map). Black rectangle indicates area of interest and white line the profile shown below. Sequence of overlaying boxes illustrates the procedure of automatic selection of the anomalous area: For each frequency, a gradient search algorithm is applied to the apparent conductivity map to identify strong lateral variations. Once the strongest gradients are mapped for all frequencies, those results are arithmetically combined to identify induction anomalies. The resulting area of strongest gradients at multiple frequencies is gap-filled, surrounded with padding based on the approximated footprint of the airborne EM system and used to extract the area (white) and data points (red lines) from the entire data set that require 3-D inversion. Bottom: section along the white line marked in the map above. The result of pure 1-D inversion (left) shows strong artefacts at the edges of the tunnel valley, which disappear when the combined 1-D/3-D inversion approach (right) is applied. Note that conductivities are plotted and colour scale goes from resistive (yellow) to conductive (purple)

gradients for each frequency individually and then arithmetically combine them. Only areas identified in neighbouring frequencies are kept, and gaps smaller than the approximate footprint of the airborne EM system are closed. Exclusively data inside this identified area and a padding zone around are then extracted for 3-D inversion. Once the 3-D inversion result is available, the 1-D and 3-D conductivity models are stitched together. Figure 12 shows an example of an airborne EM survey of the buried Cuxhaven tunnel valley in northern Germany which consists of over 460,000 measuring points. The little overlaying snapshots illustrate the steps of the automatic procedure. The 3-D inversion was done with the code by Scheunert et al. (2016), and at the bottom the comparison of the pure 1-D model (left) and the combined 1-D/3-D model (right) is shown. Clearly, artefacts related to the edges of the tunnel valley are significant for the former (i.e. downwards banded structure at both ends of the conductive anomaly) and not presented at the latter.

The following approaches are based on numerical skills to tackle the problem. They are mainly beyond the scope of this review, and the interested reader is referred to the related literature. Nevertheless, a few approaches are mentioned to make the reader aware of such codes that might be of interest when dealing with large real data sets. Cox et al. (2012) chose an approach based on the assumption that the footprint of airborne EM systems (typically less than 400 m) is significantly smaller than the area surveyed (and later combined it with a hybrid IE-FE method, Cox et al. 2015). They apply a moving footprint to perform 3-D inversion only of those parts of the entire 3-D model, which are within the footprint of a particular transmitter–receiver pair. By superimposition, they construct the sensitivity matrix of the entire 3-D model. Based on a similar idea, Oldenburg et al. (2013a) used separate meshes for forward modelling and inversion, especially using small, local meshes for each transmitter–receiver pair. This allows decomposing the large EM problem into many small, highly independent problems for which massive parallelization can be effectively applied. Yang et al. (2014b) extended this approach and introduced the adaptive sounding methodology. It is a random and dynamic downsampling method to address that it is not necessary to include all available airborne EM data at each iteration in the inversion. Yang et al. (2014b) applied a random sampler with an adaptive number of soundings selected for each iteration. Fewer soundings are used in earlier iterations to build up larger-scale structure, while more soundings are selected later as the regularization is relaxed and additional structure is need to fit the data. Holtham and Oldenburg (2012) used a domain decomposition based on a tiling approach, where they overlap meshes such that the individual tiles can be merged to a continuous final model.

Commer et al. (2008) were able to reduce the computational demands of large-scale 3-D EM problems. Their code is capable of solving large 3-D imaging problems by exploiting multiple levels of parallelization over data and model space and utilizing

different meshes for field simulation and imaging. Unfortunately, not everybody has access to a supercomputer such as the IBM Watson Research Blue Gene/L as Commer et al. (2008) did. Nevertheless, with their resources they were able to reduce the computational time from about 4 months to 1 day for a large-scale 3-D CSEM data set. Also, inversion of MT case studies (e.g., Lindsey and Newman 2015) benefits from massively parallelized codes (e.g., EMGeo by Newman and Alumbaugh 2000; Newman and Boggs 2004) and huge clusters. Additionally, application of multi-grid pre-conditioner and smoothing schemes of the multi-grid algorithm have been successfully, i.e. faster and naturally parallelizable, applied to iterative solvers (e.g., Mulder 2006; Nechaev et al. 2008; Yavich and Scholl 2012). Also, automatic mesh refinement to reduce the total number of cells while remaining fine enough at areas of interest and to cluster sites to run them separately can be utilized to handle large data sets (Grayver 2015).

To tackle the challenge of memory size and computing time, Thiel et al. (2012) used cloud computing architectures consisting of low-cost chips in data centres of public cloud service providers such as Microsoft, Amazon and Google. In general, cloud architecture is poorly suitable for message passing interface (MPI) routines involving frequent message passing, but works well for highly distributable problems, which require minimal or no communication. Parallelizing WSINV3DMT by frequency (i.e. submitting each frequency computation as a separate job), they were able to show that cloud computing is an interesting alternative to common local cluster use and has great potential for non-deterministic modelling approaches.

3.7 Misfit

The real world is unlikely to be captured by the model parameterization. The best fitting model almost certainly will not be either and, because of noise, the best fitting model will not have the same misfit as the real world does (Constable 2016).

More than for 1-D and 2-D, it is important for 3-D to appreciate that a single number, i.e. RMS value, cannot rate the misfit. It is essential that each individual data point—for example for MT each component at each frequency—has been fitted adequately. It is a positive development that more and more publications show data fits in various ways that are beyond a single number. In many cases, the misfit is nowadays plotted, for example, as map for each frequency.

Often a poor fit can be improved by a much finer model discretization, but for large-scale models such a fine discretization may not be feasible. Especially for coastal sites, discretization often is not fine enough to avoid localized large misfits. Therefore, one may ignore these local misfits visible on the misfit map but at the same time should be aware of them and their origin when interpreting the final resistivity model.

A good approach is to look at the RMS values at different levels of detail, starting from the highest level (i.e. the single number) then at a lower level (i.e. maps, pseudo-sections) down to the level of specific sites, frequencies and data components. By considering all those levels, one obtains a much better idea of the quality of the fit and which areas, sites, frequencies and/or components are causing problems. As the RMS is strongly dependent on the chosen error floors, it is sensible to run the inversion with different error floors to assess the obtained RMS values and examine the influence on the resulting resistivity model. Also, Patro and Egbert (2011) mentioned that different error normalizations used to specify the penalty functionals will result in not directly comparable RMS values. This should be kept in mind when comparing different inversion results (e.g., 2-D vs. 3-D), if the data sets were not treated equally.

Tietze and Ritter (2013) compared models with similarly good RMS value but showing significantly differing and partly erroneous and misleading images of the subsurface. They used misfit maps for individual data components to assess whether large-scale structural inconsistencies can be detected. If a particular component cannot be fit, structural information contained in other components may be attenuated or even lost. Figure 13 shows an example based on a synthetic data set, where the missing highly conductive zone results in comparably high RMS values in Z_{xy} exactly above the missing structure. Tietze and Ritter (2013) also noted that the overall RMS misfit is not rotationally invariant as only data variances are considered. This of course must be taken into account when comparing results of differently orientated meshes.

Instead of looking at RMS value plots (e.g., RMS maps for particular periods or RMS plots of periods vs. site number) often maps or curves of observed and predicted data are shown for comparison, sometimes as maps but also—especially if the data were recorded along profiles—in a pseudo-section style (e.g., Jegen et al. 2016). As diagonal impedance components are often very small and therefore have poorly defined phase values, Patro and Egbert (2011) plotted pseudo-sections of the real and imaginary parts of the diagonal impedance components scaled by $\sqrt{\text{Period}}$ rather than resistivity and phase curves.

Another approach to investigate the fit of MT data is to compare the phase tensor ellipses derived from the observed and modelled MT impedances and plot maps for the individual periods (e.g., Thiel and Heinson 2013). Figure 14a, b shows an example of such phase tensor maps by Heise et al. (2010), where orientation and minimum phase values Φ_{min} are in good agreement. The degree and spatial distribution of phase misfit can be

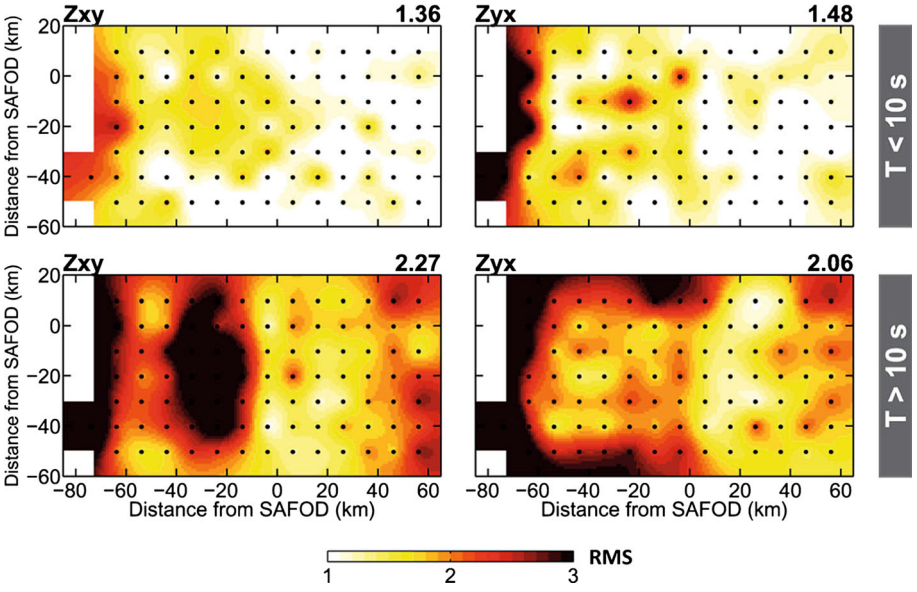

Fig. 13 Spatial distribution of RMS errors for periods below (top) and over (bottom) 10 s of the final inversion result of a synthetic test data set to simulate the San Andreas Fault settings (see Fig. 3). While the RMS errors of Z_{xy} (left) and Z_{yx} (right) are more or less equally low for periods below 10 s, Z_{xy} shows relatively high RMS values clustered at sites which are located above the not resolved highly conductive zone in about 20 km depth (modified after Tietze and Ritter 2013) (SAFOD: San Andreas fault observatory at depth)

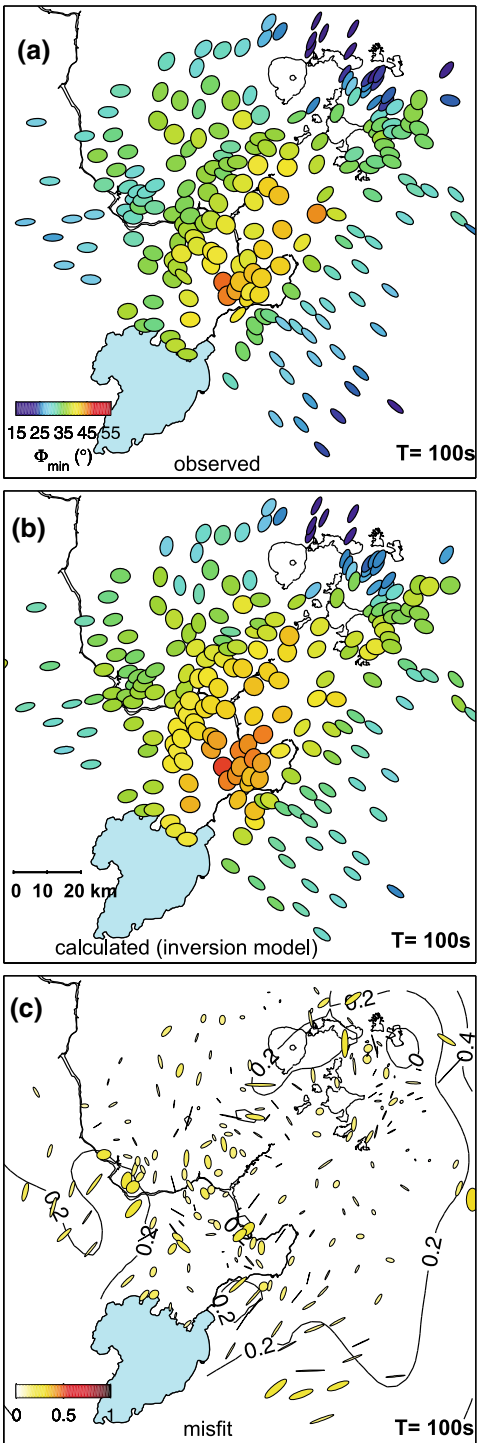

Fig. 14 Observed (**a**) and modelled (**b**) phase tensor ellipses derived from MT impedance transfer functions at $T = 100$ s (Heise et al. 2010). Face colour illustrates the minimum phase Φ_{min} (for colour scale see **a**). For most parts, the orientation and minimum phase values are in good agreement and hence well represented by the model. To even better illustrate the difference, tensor misfit (Δ) ellipses are shown (**c**). The face colour shows the mean of the maximum and minimum misfit $(|\Delta_{max}| + |\Delta_{min}|)/2$

assessed using the following tensor (Heise et al. 2007, 2008): $\mathbf{\Delta} = \mathbf{I} - \left(\Phi_{\text{obs}}^{-1}\Phi_{\text{mod}} + \Phi_{\text{mod}}\,\Phi_{\text{obs}}^{-1}\right)/2$. Therefore, Heise et al. (2010) additionally plotted tensor misfit Δ ellipses (Fig. 14c; face colour presents the mean of the maximum and minimum misfit $|\Delta_{\max}| + |\Delta_{\min}|)/2$ to even better illustrate the difference compared to a purely visual inspection of the observed and modelled phase tensor maps. In general, Δ is small, but in the southeast systematic spatial correlation in misfit can be observed.

Another and independent approach to assess the appropriateness of the model and the fit of data was suggested by Siripunvaraporn et al. (2005a) and used by Heise et al. (2010). This approach is based on data that were observed but not used during inversion (e.g., induction vector data). If such independent data are forward modelled based on the inversion result, the comparison with the observed data is a good indicator for the acceptability of the model.

3.8 Model Assessment and Resolution

As discussed before, inversion models depend on much more than just the data inputs. Therefore, it is important to pay attention to all factors beside the data that determine the result and run more than only one inversion. The most important thing for model assessment and the subsequent interpretation is to understand the nature of limitations. Questions that should be asked are (Constable 2016): are the applied physics sufficient for the problem (e.g., isotropic versus anisotropic resistivity)? Is the forward computation accurate enough (e.g., handling topography and bathymetry)? Is the model discretization fine enough while at the same time the model size is sufficiently large? It is rather implausible that all these can be achieved blindly. Therefore, understanding, experience and perhaps trial and error must be applied to assess and value the obtained model. Although done for 2-D CSEM and MT data, Constable et al. (2015) carried out in the order of 100 inversions to explore aspects of model complexity versus misfit and illustrate how regularized inversion depends on misfit, data type, model parameterization and regularization parameters. They admitted that such an extensive exploration of model and misfit space is unrealistic for 3-D but suggested that 2-D inversion provides an effective way to explore EM data sets before the computational cost of 3-D inversion is expended.

There are many approaches for model assessment—most of them are discussed in the following—based on different data subsets, inversion parameters and initial (and prior) models, but also comparison with 2-D models, other data sets and a priori information as well as modifying the final resistivity structure, including tear zones and testing for boundary effects. Even comparison of results using coarse and fine meshes is made, but modification of the model discretization (e.g., shifting the mesh by half a cell size in x- and y-direction) by unchanged resistivity distribution seems to be unpopular. It is a pity, as this could provide an indication of the influence of the cell edge locations on the obtained result, but so far mesh testing is only done before inversion. Also hardly done are tests to assess the amount of code bias in the resulting inversion model. For example, one should consider performing forward modelling tests based on the final or manipulated models with other codes that are based on a different forward engine (e.g., Tietze and Ritter (2013) did their forward modelling tests using ModEM and WinGlink). Of course, this would require access to other codes and a bit of effort to re-discretize the model and adopt to a different data format according to the needs of the other code, but this might be worthwhile.

3.8.1 Resolution

Discretization as well as the number and distribution of sites and periods has an influence on the resolution in the 3-D inverse model and the amount of realistic equivalent models. If the site spacing is larger than the structures causing distortion, such shallow structures are expected to be less reliable than deeper structures. Running many inversions with varying inversion parameters (e.g., regularization and smoothing parameters), data subsets (e.g., in terms of included sites, data components and periods) and initial/prior models (different half-space and 1-D layered model, model with a priori information) can be useful to assess the resolution and allows to find a reasonable preferred inverse model (e.g., Yang et al. 2015). In addition, estimates of the skin depth at the shortest period can be a hint on the limited vertical resolution at shallow depth and at the longest period on the maximal depth with reliable resistivity information. On the other hand, using 1-D penetration depth estimations such as skin depth or Niblett-Bostick depth approximation (Niblett and Sayn-Wittgenstein 1960; Bostick 1977) is not necessarily reliable in 3-D as currents can flow around resistive bodies. Therefore, these are just very crude estimates and may not suggest equal depths of investigation for all components; nevertheless, some sort of depth approximate should be considered to assess the data coverage.

In seismic tomography, resolution tests are commonly performed by the so-called checkerboard tests. However, the physics of electromagnetic data and seismic tomography data is very different. While seismic energy is penetrating to all levels of the model with little distortion, electromagnetic energy is screened from deeper blocks by structures above and the requirement of continuous current flow makes the blocks act very differently compared to seismics. Additionally, EM responses from 2-D and 3-D checkerboard structures are fundamentally different and current flow through a small conductive connection between large-scale conductive regions can be 'lit up' even if skin depth considerations suggest the connection should not be resolvable (e.g., Burd et al. 2013, 2014). Hence, the required derivative matrix strongly depends on the resistivity model itself. Therefore, a checkerboard test is not applicable to electromagnetic data.

There are numerous approaches to investigate model validity and appraisal for EM. One is the comparison of results obtained for only a data subset, i.e. subsets of observation sites (e.g., Ingham et al. 2009) or period ranges (e.g., Newman et al. 2008; Farquharson and Craven 2009) or data components (e.g., individual impedance elements analogous to TE and TM mode inversion in 2-D or separate inversion of impedance and VTF, Tietze and Ritter 2013).

3.8.2 Assessment by Forward Modelling

Another approach is to test whether a structure is required to explain the data by manipulating the model. One can remove or add structures or connect regions of similar conductivity or change resistivity or position of certain features and then calculate the forward responses—the so-called hypothesis testing. If the predicted data of the manipulated and the original model are the same (within measurement errors), the modified structure (e.g., removed conductor or resistor) is not contributing and therefore not required. The reverse is not a rigorous test for existence but an indication. However, these can be sensitivity tests concerning specific (isolated) features in the inversion model (e.g., Hill et al. 2009; Xiao et al. 2010; Bertrand et al. 2012a; Kelbert et al. 2012; Yang et al. 2015; Ślęzak et al. 2016)

or a comparison with 3-D forward modelling of principle model structures (e.g., Tuncer et al. 2006; Heise et al. 2008, 2013; Tietze and Ritter 2013).

One has different options to assess the changes between the synthetic data based on the inversion result and the manipulated model. One is to simply compare the global RMS values obtained based on those two models. This might give an idea of the influence of the added/removed/modified structure on the calculated responses, but suffers from all the previous discussed issues of using a single number as measure of misfit. Therefore, site-by-site and/or period-by-period comparison of the misfit must be made—of course with the focus on those sites and periods that correspond to the manipulated model area.

Figure 15 shows an example presented by Meqbel et al. (2014), where they assessed the influence of structures to the east of the array by extending the model domain 500 km eastwards, where the background resistivity was set to 100 Ωm as for the prior model. The preferred inverse model with the extension was subsequently modified in three steps. First, all resistivities below 10 Ωm were set to 10 Ωm (Fig. 15c). Secondly, an elongated, 1 Ωm block was added to simulate the North American Central Plains (NACP) conductivity

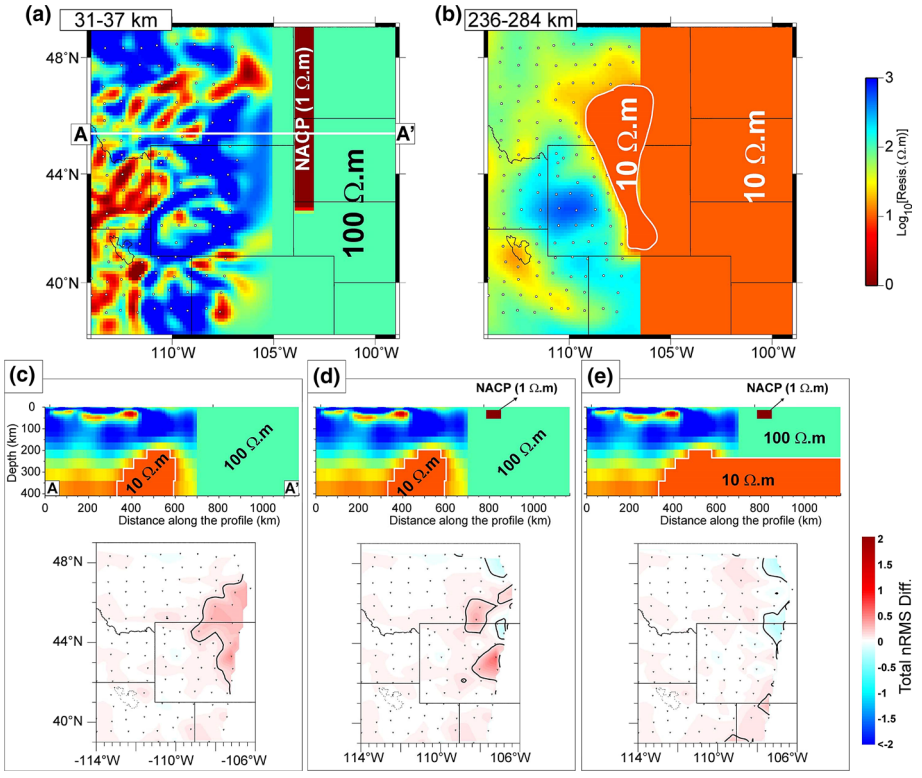

Fig. 15 Example of model assessment using forward modelling tests (Meqbel et al. 2014). To assess the possible influence of structures to the east of the array Meqbel et al. (2014) extended the model domain 500 km eastwards with background resistivity set to 100 Ωm. Three cases are considered and illustrated in cross sections (**c** resistivities below 10 Ωm are set to 10 Ωm; **d** 1 Ωm, elongated block is included to simulate the NACP conductivity anomaly; **e** 10 Ωm asthenospheric mantle below 250 km depth towards the east). Additionally, two depth slices (**a**, **b**) of model (**e**) are shown above. Below the cross sections (**c**–**e**) the total RMS differences for each model are shown (Reprinted from Meqbel et al. (2014) with permission from Elsevier)

anomaly (Fig. 15d). Finally, below 250 km the resistivity was set to 10 Ωm simulating the asthenospheric mantle layer (Fig. 15e). Two horizontal depth slices of the latter are shown above (Fig. 15a, b). Below the cross sections (Fig. 15c, e), the total RMS differences are shown for each model. Meqbel et al. (2014) observed increasing misfit at the eastern sites if the minimum resistivity was set to 10 Ωm, while the two conductive blocks to the east showed a comparable misfit to the preferred inverse model. Hence, those blocks were not required by the data. In a similar manner (not shown here) they tested the depth resolution of their data set, i.e. below a certain depth they freeze the resistivity to the prior value, and by varying that depth level and comparison of the RMS differences they conclude that their data can resolve structures down to 350–490 km depth.

An alternative is to use the change in normalized phase tensor skew angle Ψ relative to its estimated error σ given by $\delta\Psi_\sigma = |\Psi - \Psi_0|/\sigma = |\Delta\Psi|/\sigma$ (Burd et al. 2014). Using $\delta\Psi_\sigma$ has the advantages that it is unaffected by shallow 3-D distortion and large-scale 1-D or 2-D model changes and, additionally, it is independent of the coordinate system it is computed in. Furthermore, it combines all impedance elements and can be examined by site maps of individual frequencies. Burd et al. (2014) state if $\delta\Psi_\sigma > 1$ at many sites or $\delta\Psi_\sigma > 2$ at few sites one can be confident that the change in structure has strongly affected the data.

3.8.3 Constrained Inversion Using Manipulated Inverse Models

Computationally more intensive but also more rigorous testing is to run an inversion that is constrained to omit the debatable structure. Figure 16 shows an example from the Payún Matrú volcanic field in the Andean backarc of Argentina (Burd et al. 2014). The original

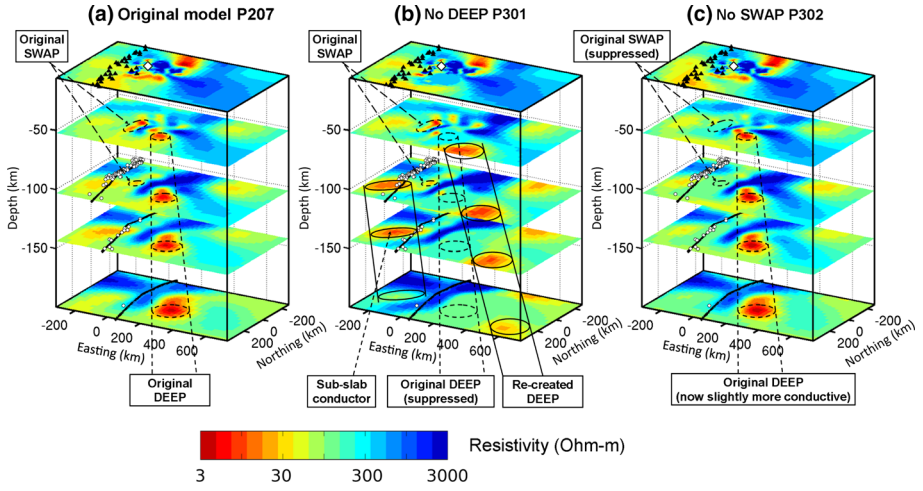

Fig. 16 Model assessment by structure removal—an example from the Payún Matrú volcanic field in the Andean backarc of Argentina (taken from Burd et al. 2014). The original model (**a**) shows two conductors called DEEP and SWAP which are tested for model reliability. The inversion results of suppressed DEEP (**b**) and SWAP (**c**) were obtained by setting the area of the conductor to background resistivity and keeping it fixed during inversion. Black triangles are Southern Volcanic Zone volcanoes active in the Holocene, white diamond at surface is the location of Payún Matrú Caldera, and black lines and dashed black lines are location of subducted Nazca slab, based on the slab surface discussed in Burd et al. (2013). White points are hypocentres of recorded earthquakes

inverse model (a) shows two conductive structures—DEEP (deep eastern plume) and SWAP (shallow western asthenospheric plume). Burd et al. (2014) used a threshold scheme in which they replaced resistivities below 100 Ωm by the mantle background resistivity (approximated by 100 Ωm) and kept the structure of the altered volume fixed. Using this approach, they tested the existence of DEEP (b) and SWAP (c). The result of suppressed DEEP is interesting as just outside the forbidden volume an almost identical conductor re-forms and the conductivity of the subvertical conductor (subslap conductor in Fig. 16b) increased a lot. Their explanation is that a specific amount of vertical current flow is required by the model to fit the data. As DEEP is suppressed, the inversion increases vertical current flow elsewhere to compensate. They call those structures 'halo plumes' and emphasize that there is no reason to read geological meaning into those halo structures. Burd et al. (2014) concluded that the removal of entire DEEP is not permitted by the data. However, removing SWAP slightly decreased the resistivity of DEEP (especially at shallow depth) and the subslap conductor become less conductive. This is possibly related to cutting off the electrical connection to this subslap conductor, i.e. reducing current flow through it. To investigate SWAP further (not shown), they systematically implemented gaps in the plume to block vertical current flow and performed forward modelling tests. They found that, while SWAP is dominantly a mantle feature, it is definitely extending into the crust and has two conductive chimneys approaching the surface beneath Payún Matrú caldera and Trómen volcano.

To obtain a comprehensive image of the subsurface (i.e. resistivity structure as well as absolute resistivity) inversion results of various data components (e.g., phase tensor, VTF, impedance) should be compared and combined to exploit the advantages of each data type and to accomplish a solid basis for the best possible interpretation. One should try to explore the entire model space, especially considering not only smooth inversion but also sharp boundary inversion. Another common and from 2-D well-known approach is to compare inversion results with and without tear zones.

3.8.4 Comparison 2-D Versus 3-D

Other authors also compare 2-D (based on data subsets, especially if recorded along profiles) and 3-D inversion results (e.g., Tuncer et al. 2006; Newman et al. 2008; Türkoğlu et al. 2009; Cumming and Mackie 2010; He et al. 2010; Heise et al. 2010; Patro and Egbert 2011; Bertrand et al. 2012a, b; Tietze and Ritter 2013; Ślęzak et al. 2016) and often find good agreement in the main features of the resistivity structures but significant differences in details. Even observations of opposed resistivities at parts of the model are reported but interpreted as effect of the limitation of the 2-D analysis of 3-D data (e.g., Heise et al. 2010; Patro and Egbert 2011; Tietze and Ritter 2013; Ślęzak et al. 2016). Another reason could be that 3-D inversion cannot resolve the structure in the required detail (e.g., Tietze and Ritter 2013). In such a case, a forward modelling test including the missing feature will reveal if it is consistent with but not required by the data. Tietze and Ritter (2013) observed that their conductive zone is imaged narrower and shallower in 3-D models compared to 2-D. Using synthetic studies they found that 3-D inversion tends to place structures systematically at shallower depths compared to the true structure if the prior and initial model are too conductive. Cumming and Mackie (2010) stated that 1-D and 2-D MT inversions—where they are dimensionally valid—are likely to have higher resolution than a 3-D inversion as they are less robustly smoothed.

Meqbel et al. (2016) also present a rarely used approach to assess their resistivity model from Dead Sea Basin MT data. They included a conductive feature from their 2-D model

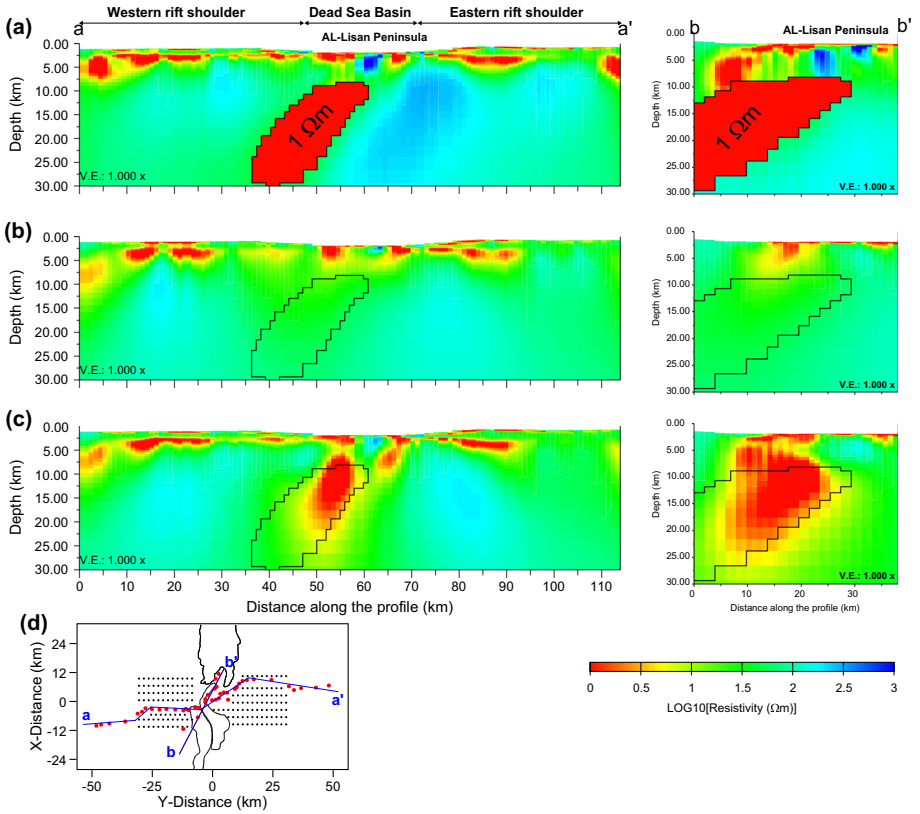

Fig. 17 Assessment of sensitivity of the site layout with respect to changes in the subsurface resistivity structure by Meqbel et al. (2016). A deep conductive channel was inserted into the preferred 3-D resistivity model of the Dead Sea Basin data (**a**) and this model was used to generate synthetic MT data. The inversion results of the synthetic data using (**b**) the real site distribution (red dots in d) and (**c**) additionally a regular grid of sites distributed evenly around the Dead Sea Basin (black dots in **d**) are shown below

into their preferred 3-D resistivity model (Fig. 17a) and computed synthetic impedance and VTF data at the real site locations supplemented with a quasi-regular grid of 2.5 km site spacing (red and black dots in Fig. 17d, respectively). The inversion based on the synthetic data using the real site distribution (Fig. 17b) fails to recover the massive conductive channel, while the result based on both the real plus the regular grid sites shows a conductive feature (Fig. 17c). Nevertheless, its top seems smeared with the overlaying conductive sedimentary formation of the southern Dead Sea Basin. Meqbel et al. (2016) concluded that this test has demonstrated that the available site coverage is insufficient to confirm or exclude the existence of a deep, subvertical conductive structure beneath the basin. Furthermore, they found that the conductivity contrasts are much stronger in 2-D than in 3-D. Due to the diffusive nature of the MT method, sensitivity is high for the shallow parts and the 3-D inversion seems to introduce shallow-off-profile features at the cost of levelling out conductivity contrasts at greater depth beneath the profile.

Another example why 2-D inversion can be beneficial for 3-D model appraisal is described by Tietze and Ritter (2013). A conductive path parallel to the coastlines, which is meant to connect the highly conductive zone in about 20 km depth with the San Andreas

Fault, is visible in 2-D inversion models of MT impedance and VTF data but absent in 3-D models. The 3-D inversion performed with ModEM was fitting real and imaginary parts of the impedance tensor rather than apparent resistivity and phase values (as usually done for 2-D inversion). Using standard error settings the larger component (i.e. Z_{yx}) was fitted at the expense of the smaller one (i.e. Z_{xy}). Only the misfit maps (see Fig. 13) and looking at phases revealed the bad fit of Z_{xy}. While 2-D inversion was able to fit the phases and showed the conductor in the final model, 3-D inversion parameters had to be manipulated such that the smaller impedance components are fit, and hence, the conductive channel became also visible in the 3-D inverse model. Therefore, Tietze and Ritter (2013) suggested that 2-D and 3-D inversion should be used complementary. While 3-D has clear advantages in complex subsurface situations, 2-D still provides more options and control about resolution of small-scale structures, handling static shift, detailed topography and bathymetry and finer mesh discretization.

3.8.5 Site Coverage

The Dead Sea Basin example by Meqbel et al. (2016) already indicated that the site coverage could affect the inverse model. A synthetic data example that illustrates the influence of site distribution on the resulting model is the Dublin Secret Model DSM2 (MT 3-D inversion workshop II, 2011). It was designed for code testing (i.e. synthetic data of a

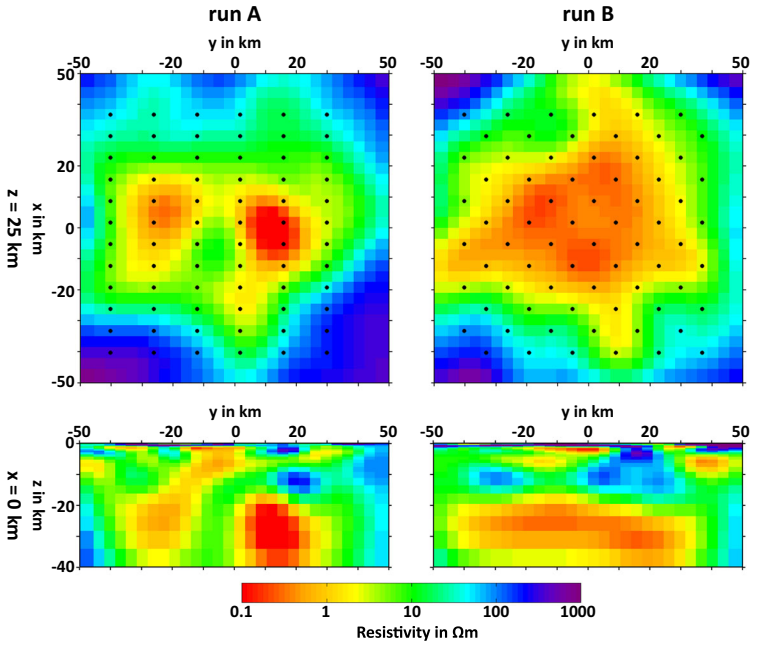

Fig. 18 Comparison of two MT inversion results of the DSM2. The inversions were performed by Vozar using half of the provided sites each: every second profile (run A, left column) and a checkerboard-like selection of every second site (run B, right column). On top a depth slice ($z = 25$ km) and at bottom a section ($x = 0$ km) of the resulting inverse models are shown. The black dots represent the sites used. Full comparison of all depth slices and inversions by others as well as the details on the inversion parameters and the true model are shown by Miensopust et al. (2013)

structure unknown to the participants) and consists of an MT data set of 144 sites with 30 periods each with random galvanic distortion and Gaussian noise (Miensopust et al. 2013). Each participant was free to decide how many and which sites and periods were used for inversion. The inversion results presented clearly show the effect of using different data subsets on the achieved model (Fig. 18). Keeping the inversion code, mesh, inversion parameters, initial model, number of periods and error floor the same, Vozar ran the inversion twice each with half of the available sites: first by using every second profile (left, run A) and secondly using a checkerboard-like selection of every second site (right, run B).

Although in both cases the site distribution is very regular over the entire area of interest, it is obvious that the selection of sites has an influence on the obtained model, but none of them is able to capture the true structure correctly (not shown, see Miensopust et al. 2013, for more details). In a synthetic case one is aware of these shortcomings as the true structure is known, but using field data one does not know the real resistivity structure. Additionally, in the field the distribution of sites is rarely covering the area of interest with such a regular and dense array.

3.8.6 Personal Choice Matters

In 2014, both Bedrosian and Feucht (2014) and Meqbel et al. (2014) each published a 3-D resistivity model of the north-western USA derived from the EarthScope USArray magnetotelluric data (Schultz et al. 2006–2018, 2008–2013). Although the field data set was identical, they used very different data subsets, applied diverse error estimates and used different 3-D inversion codes and model discretization (see Table 1). The only common setting was the resistivity of the initial model (i.e. 100 Ωm half-space including the 0.3 Ωm ocean). Figure 19 shows both resulting models as a lower crustal depth slice at approximately the same depth as well as two pairs of roughly coinciding profiles. In principle,

Table 1 Comparison of data subsets, inversion settings, etc., used by Bedrosian and Feucht (2014) and Meqbel et al. (2014), respectively, to invert the same EarthScope MT data set (Schultz et al. 2006–2018, 2008–2013)

	Bedrosian and Feucht (2014)	Meqbel et al. (2014)
No. of sites	241	325
Components	Full impedance Z	Full impedance Z and VTF
Periods	10 log-spaced (full period range)	Z: 22 (full period range) VTF: 19 (only < 6500 s)
Error	5% relative (individual component)	5% of $\lvert Z_{xy} Z_{yx}\rvert^{1/2}$ to all Z 0.03 for VTFs
Code	WSINV3DMT	ModEM (nested mesh)
Cell size	Horizontal: 15 km Vertical: 250 m–100 km (Crust typically 1–2 km)	Horizontal: 12.5 km Vertical: 50 m (43 layers with factor 1.2)
Initial model	100 Ωm half-space including 0.3 Ωm ocean	100 Ωm half-space including 0.3 Ωm ocean

See Fig. 19 for inversion results

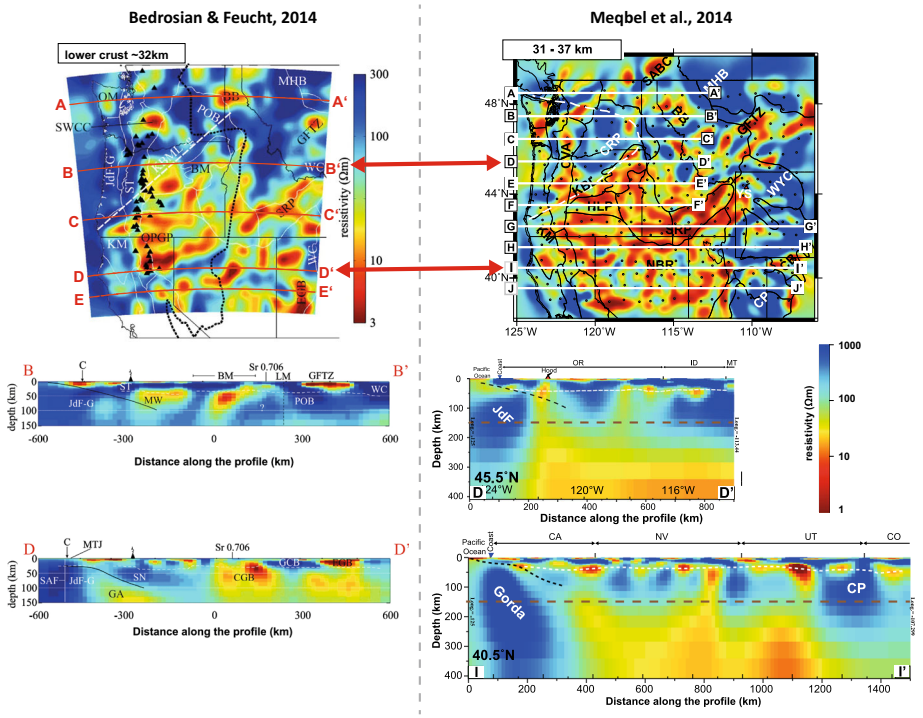

Fig. 19 Comparison of 3-D resistivity models of the north-western USA derived from EarthScope USArray data by (left) Bedrosian and Feucht (2014) and (right) Meqbel et al. (2014). At the top one horizontal slice each of approximately the same depth is shown and below are two pairs of roughly coinciding profiles (marked by red arrows). See Table 1 for details on the used data subsets and inversion settings (Reprinted from Bedrosian and Feucht (2014) and Meqbel et al. (2014) with permission from Elsevier)

there are some common structures visible in the models but also many differences (for a detailed comparison of both models see Meqbel et al. 2014). It is impossible to distinguish the diverse contributions of the various differences [e.g., in terms of used data subset, error settings, code, mesh, boundaries, regularization, visualization (see also Sect. 4.3)] and therefore to favour one model over the other. And the most important question is, are those differences crucial for interpretation?

4 Interpretation

Beside the above-discussed model validity and appraisal (see Sect. 3.8), limitations of detectability of structures (see Sect. 4.1) and the presence of anisotropy (see Sect. 4.2) are concerns for interpretation. At least as important but often underestimated is the visualization of the resistivity model (see Sect. 4.3), which is the basic information used for interpretation. Before those three aspects are discussed in detail, a few general concerns and examples are mentioned.

Even if the obtained model is a good representation of the true resistivity distribution, those values themselves may not ultimately be the quantity of interest but the geology

itself. Fullea (2017) describes in detail how such secondary geophysical parameters like electrical conductivity and more fundamental primary parameters describing the thermo-chemical state of rocks within the earth (e.g., temperature, composition, melts) can be combined to enhance interpretation and understanding of the subsurface. Additionally, for natural field EM data conventional inversion techniques do not provide images with the resolution necessary to accurately locate drill holes, for example over typical massive sulphide targets (Watts 2012), but assist in assembling a conceptual model that would define drilling targets (Cumming and Mackie 2010). In any case, to avoid that the resistivity models are over-interpreted, a good interaction between the geophysicist that performed the inversion and the geologist/engineer who interprets the model is required (Holtham and Oldenburg 2012).

The sequence from data collection to a final resistivity image is subject to a multitude of underlying assumptions and simplifications as well as to noise and uncertainty at each step. Nevertheless, those uncertainties are rarely incorporated in the final assessment of the reliability of the image (Watts 2012). Furthermore, all the underlying assumptions and simplifications regarding the data (see Sect. 3.1), models (see Sects. 3.2 and 3.3) and inversion settings (see Sect. 3.4) imply limitations on the validity of the inverse model.

Resistivity models based on minimum-structure inversion depend largely on smoothing parameters and other inversion settings, i.e. they often lead to non-geological images, which have to be interpreted in the light of other data. Therefore, comparing the resistivity models with results from other geophysical studies such as seismics (e.g., Kelbert et al. 2012; Jegen et al. 2016; Ślęzak et al. 2016), earthquake hypocentres (e.g., Heise et al. 2013; Robertson et al. 2016) or surface heat flow data (e.g., Thiel and Heinson 2013; Padilha et al. 2015) or magnetic and gravity anomaly maps (e.g., Yang et al. 2015; Robertson et al. 2016) can be useful and supportive for the interpretation (i.e. qualitative, post-analysis approach by Bedrosian 2007). Instead of a visual comparison of subsurface models based on different geophysical methods, clustering methods can also be applied for interpretation. Ledo et al. (2016) presented a new 3-D image of Tenerife Island obtained by using soft clustering methods (i.e. fuzzy c-means) for combining the independently derived models of magnetotelluric and seismic velocity data. This new 3-D image allows better identifying the main geological structures and processes on the island.

Newman et al. (2003) discussed how misleading the interpretation of RMT data over a waste site deposit can be. From borehole information they knew that the base of the waste deposit is at about 13 m. Using 2-D RMT inverse models, they found a conductor of about 20 m thickness, while 3-D inversion results in an approximately 16-m-thick conductor. With the aim to identify contamination beneath the waste deposit one could be misled to interpret a conductor thicker than the waste deposit itself as an indication of leakage. Including the background resistivity found at a profile outside the deposit into the initial model of the 3-D inversion they obtained an estimate near 13 m for the base of the pit, which is in good agreement with the borehole data. The discrepancy in thickness has influence not only on the possible detection of leakage but also on the estimate of the pit volume which is overestimated by a factor of approximately 1.5 if the background resistivity found at the profile outside the deposit is not included in the initial model of the 3-D inversion (Newman et al. 2003).

4.1 Considering Limits of Detectability

As the example from the Dead Sea by Meqbel et al. (2016) showed (Sect. 3.8.5, Fig. 17), detectability of structure depends on the data coverage, but this is not the only influencing parameter. The following examples will illustrate a few others.

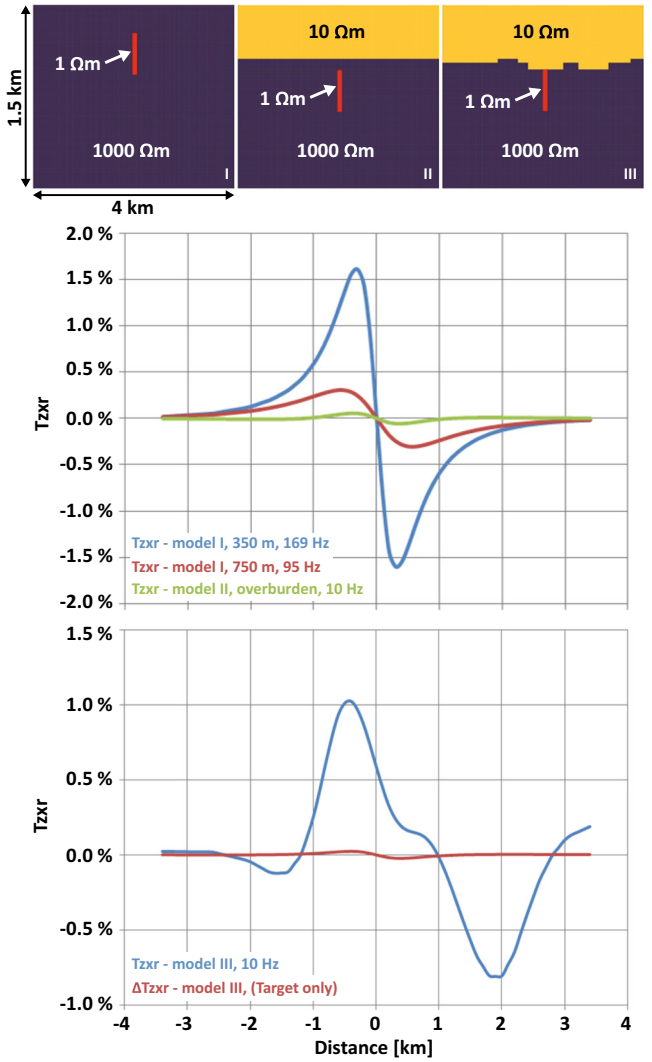

Fig. 20 AFMAG responses obtained for synthetic models based on typical settings of 3-D sulphide targets (modified after Mackie and Watts 2012). Top: three models—vertical conductor (75 m × 350 m × 500 m) in uniform resistive host (I), with added 500-m-thick conductive overburden (II) and finally with variable thickness of the overburden (III). Middle: AFMAG responses as Tzxr in percentage over model I with target depths of 350 m (blue) and 750 m (red) and model II (green) at the frequency which gives the maximum response in the 10–1000 Hz range. Bottom: AFMAG responses as Tzxr in percentage over model III (blue) and the response contribution of the target (red)

A common application of AFMAG (audio frequency magnetics) is massive sulphide exploration with target depths down to 500 m. Mackie and Watts (2012) investigated the detectability of a large, conductive 3-D target corresponding to a 50 million ton target under conditions ranging from heterogeneous conductive overburden to a highly resistive host according to field observations in Australia and Canada, respectively. Figure 20 shows that in the case of a uniform resistive host of 1000 Ωm a measurable response is obtainable

down to a depth of 750 m below surface when assuming a noise level of 0.25%. On the other hand, introducing a 500-m-thick overburden of 10 Ωm will already reduce the response to 0.02% at a frequency of 10 Hz, hence below noise level. If a heterogeneous overburden (in this case with varying thickness) is assumed, the response contribution of the target itself (Fig. 20 bottom; red line) becomes even smaller, i.e. unrecognizably small. This study clearly shows what is detectable depends not only on the target itself and on the resistivity distribution of the surrounding host but also on the presence of conductive overburden and the roughness of the interface. These shielding effects should be considered during interpretation.

Gist et al. (2013) reported about a false positive in hydrocarbon exploration. Using marine CSEM, surveys are expected to map regions of high vertical resistivity in areas of resistive hydrocarbon reservoirs, but not all regions of enhanced vertical resistivity are associated with hydrocarbons. Nevertheless, the combination of high resistivities by CSEM and low acoustic impedances by 3-D seismics found at the Fox Roost in the Orphan Basin, Canada, was wrongly interpreted as indicative of hydrocarbon presence. Figure 21 shows a synthetic study explaining the false positive, which is caused by the properties of the non-net (here: shale and sand that is too thin or has too low porosity to be considered reservoir quality). Gist et al. (2013) show the probability distribution of wet and hydrocarbon reservoir models (Fig. 21). The CSEM inversion results (green shaded area) allow the possibility of wet reservoir (blue) but are more consistent with hydrocarbon reservoir (red). Hence, thin resistive layers make it possible to have a high vertical resistivity even though the depth interval sensed by CSEM contains thick layers of conductive wet reservoir. Gist et al. (2013) stated that sometimes false positive can be mitigated by additional information (e.g., high acoustic impedance can indicate that the high resistivity is associated with low porosity), but at Fox Roost the low porosity layers are too thin to affect the seismic response. Therefore, a false positive cannot always be avoided!

Deeper structures can be shielded and confounded by highly conductive and inhomogeneous structures above and, therefore, an interpretation should focus on those parts above that are robustly resolved. Other artefacts may be caused by biases introduced by near-surface distortion or vertical smearing from lateral variations in more deeply seated low resistivities (Patro and Egbert 2011). It is also important to keep in mind that only the conductance of a structure is constrained by the data, i.e. a thinner layer of much lower

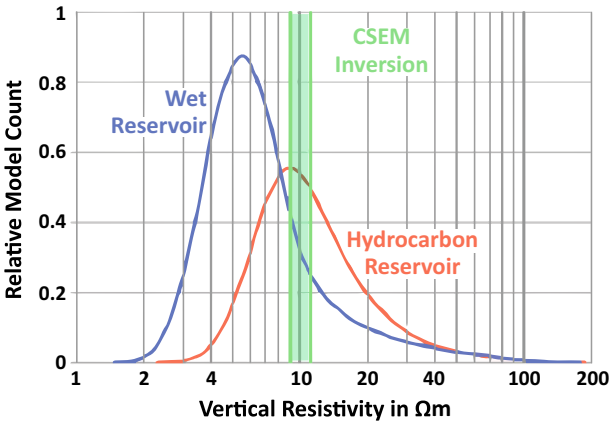

Fig. 21 Estimation of the probability density of CSEM vertical resistivities based on random 1-D models to explain false positive [modified after Gist et al. (2013)]. The probability densities for vertical resistivities expected from hydrocarbon (red) and wet (blue) reservoirs at Fox Roost, Canada, are shown. The green shaded area is the range of target-level vertical resistivities from the CSEM inversions at Fox Roost

resistivity would be indistinguishable from a much thicker and more resistive layer in the inverse solution.

4.2 Anisotropy

Another issue that affects EM data besides distortion and noise is the presence of anisotropy. Details on the main theoretical aspects how electrical anisotropy may influence EM data—especially MT responses—and the consequences for analysis, modelling and inversion can be found in the review by Martí (2014).

At the Taupo Volcanic Zone, New Zealand, Heise et al. (2010) performed a 3-D inversion of MT data using 220 sites. The final inversion model shows a region of high resistivity values, where an interconnected melt fraction is present and concentrated surface heat flux is observed (Bibby et al. 1995). It is known from isotropic 2-D inverse models of anisotropic structures that alternating conductive and resistive zones are produced to satisfy the competing demands of model regularization and the assumption that the resistivity is isotropic (Heise and Pous 2001; Wannamaker et al. 2002). Therefore, Heise et al. (2010) tested the 3-D model for a similar effect. They replaced the resistor in the final 3-D model (R1, Fig. 22a) by narrow alternating strips of low (10 Ωm) and high (200 Ωm) resistivities to represent a SW–NE trending anisotropic zone below 13 km depth (Fig. 22b) and computed the 3-D forward modelling responses. The obtained phase tensor misfits of both models are similar, and therefore, they concluded that a zone of anisotropic

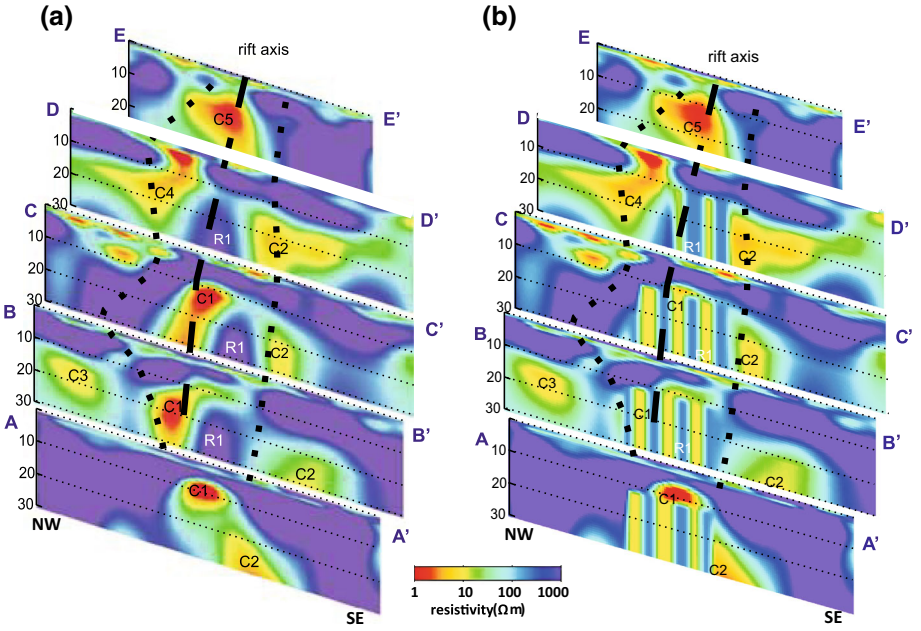

Fig. 22 Cross sections of the 3-D inverse model (**a**) and the anisotropically modified forward model (**b**) of the Taupo Volcanic Zone (TVZ), New Zealand (modified after Heise et al. (2010); dotted lines: margins of the TVZ, dashed line: rift axis). Low and high resistive strips simulating an anisotropic resistivity structure of a dyke swarm parallel to the rift axis replace the resistor R1. Obtained phase tensor misfits of both models are similar (not shown)

resistivity below a depth of 13 km is also a plausible model. Such a zone could be related to a SW–NE trending dyke swarm parallel to the axis of extension of the rift system.

Furthermore, Heise et al. (2010) found the central conductor to be suggestive of a rising melt plume and therefore tried to investigate its melt fraction. Considering the lowest resistivity (0.3 Ωm) in this conductive zone and assuming a resistivity of 0.1 Ωm for the melt (Schilling et al. 1997) they got an interconnected melt fraction of about 50%. They rated this estimate as highly uncertain as the resistivity values determined by the inversion depend—amongst other factors—on the regularization chosen for inversion. Additionally, they pointed out that MT resolves the total conductance of a conductive layer rather than its conductivity, and therefore, the melt fraction may be underestimated. On the other hand, they referred to Siripunvaraporn and Egbert (2009) who showed an implementation-related tendency of the used code (WSINV3DMT) to overestimate the conductivity of conductors. This example reminds one that caution is demanded when obtained resistivity structures are to be interpreted quantitatively.

For CSEM data, sensitivity to horizontal resistivity is strongest in broadside electric field data where detectors are offset from and orientated parallel to the towing line, while sensitivity to vertical resistivities is strongest for overflight data where the transmitter passes directly over the receiver. Therefore, Newman et al. (2010) pointed out that a consistent treatment of overflight and broadside electric field measurements require an anisotropic approach; otherwise, serious artefacts can be produced for certain data configurations. Horizontally layered sedimentary sequences relevant for oil and gas exploration can exhibit transverse anisotropy, and therefore, Newman et al. (2010) considered independent horizontal and vertical resistivities. Figure 23 shows an example from CSEM data acquired over the Troll West Gas Province (TWGP) off-shore Norway in the North Sea (Newman et al. 2010). An interpreted geological section by Johansen et al. (2005) based on well log and seismic data (a) is shown in comparison with CSEM imaging results for isotropic (b) and anisotropic—horizontal (c) and vertical (d)—media. The gas field is imaged by the isotropic model as well as by the vertical component of the anisotropic resistivity models, and it seems like the isotropic model merges the two anisotropic resistivity contributions to a single image, however at the cost of a higher misfit.

Ó Súilleabháin et al. (2012) made a very similar observation at a prospect off-shore Malaysia. The isotropic 3-D inversion of the CSEM data (1-D initial model based on well logs and including topography) shows a large conical low-resistivity zone coincident with—but a little narrower than—the observed seismic wipe out zone (Fig. 24a, b, respectively). As they believe the structure is a mud volcano, they expect the vertical fluid movement in the mud volcano would severely disrupt the horizontal layering system, leading to a quiet seismic image. In addition, the vertical resistivity would be affected and lowered to a level similar to the horizontal. Therefore, Ó Súilleabháin et al. (2012) performed an anisotropic CSEM inversion and tested an isotropic and anisotropic initial model. They found the vertical resistivity section (c) to be qualitatively similar to the isotropic one (a) although the conical low-resistivity zone is not as well defined. In contrast, the horizontal component (d) shows little correlation with the seismic wipe out zone and is generally more conductive than the vertical resistivity. Inside the wipe out zone, both the horizontal and vertical resistivities are similar, supporting the idea of Ó Súilleabháin et al. (2012) that the presumed mud volcano disrupts the vertical layering and renders the resistivity isotropic. They did not observe a difference between an isotropic or anisotropic initial model for the anisotropic inversion and therefore concluded that the CSEM inversion can at least qualitatively infer anisotropy even without prior knowledge of its polarization and amplitude.

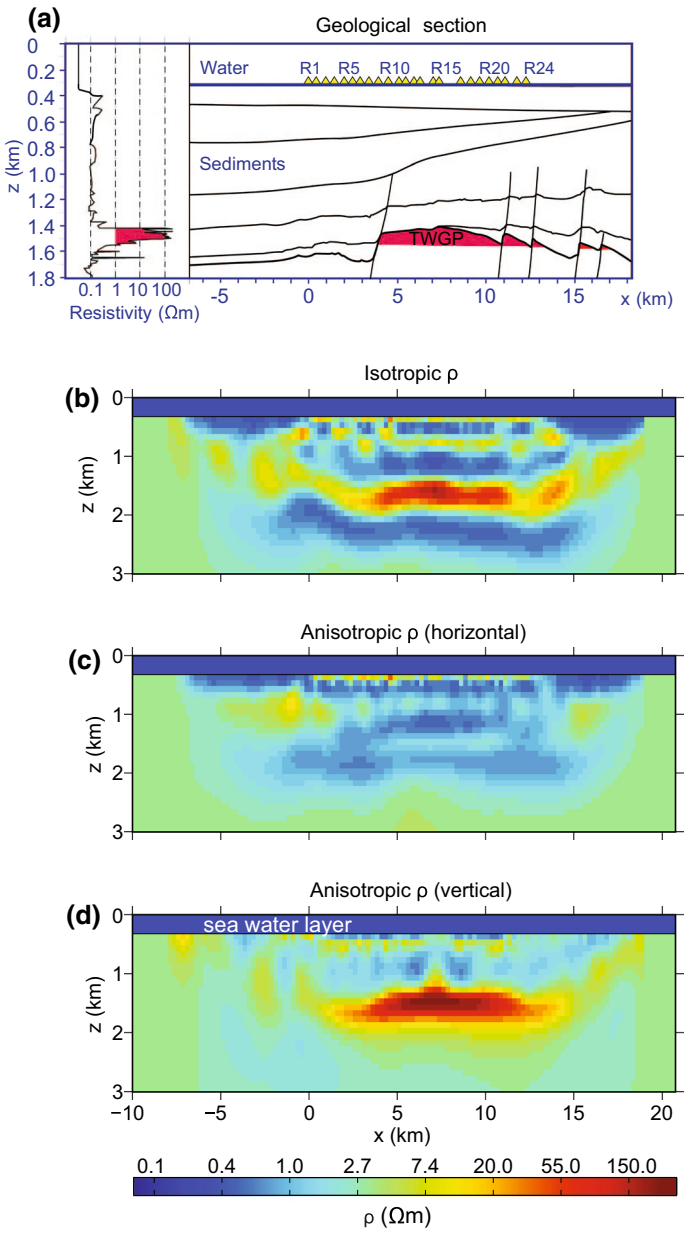

Fig. 23 CSEM imaging results from Troll West Gas Province (TWGP) off-shore Norway (taken from Newman et al. 2010). Geological section (**a**) based on well log and seismic data (Johansen et al. 2005) is shown in comparison with isotropic (**b**) and anisotropic—horizontal (**c**) and vertical (**d**)—CSEM imaging results. Note that the vertical scale of **a** is slightly different from **b**–**d**

The above examples clearly show that even if 3-D inversion is applied, there might be anisotropic resistivity structures which cannot be resolved or recognized in the final image. Therefore, an entire class of equivalent models is missing and not considered for

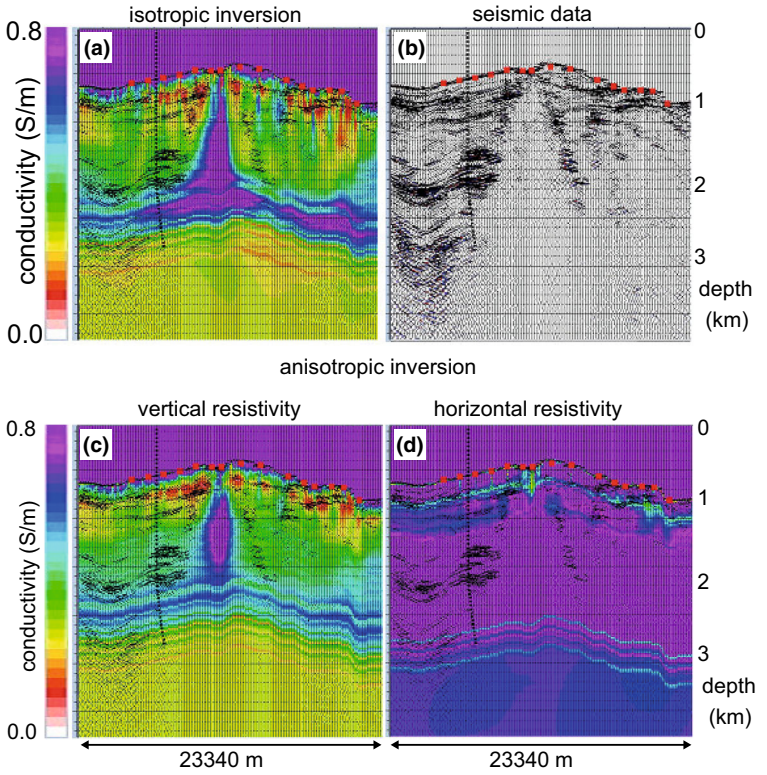

Fig. 24 CSEM inversion results of a prospect off-shore Malaysia (Ó Súilleabháin et al. 2012). The isotropic 3-D inversion result (**a**) shows a conical conductive zone where the seismic wipe zone exists (**b**, and overlain on the other three panels). Anisotropic inversion (**c**, **d**) shows that the wipe zone—associated with a mud volcano—coincides with an isotropic conductivity zone. This zone is associated with vertical fluid movement in the mud volcano disrupting the horizontal layering, which otherwise causes a lower resistivity of the horizontal than vertical direction

interpretation. Especially for hydrocarbon and geothermal but also permafrost targets, anisotropy may become a crucial issue.

4.3 Visualization

While it is quite obvious how to present a 1-D or 2-D resistivity model, for 3-D there seems to be no perfect way to visualize the entire model—especially if one is limited to a 2-D, unmovable medium (e.g., a figure in a publication or poster). Most common visualization approaches (Fig. 25) show individual or sequences of horizontal depth slices and vertical sections (e.g., Patro and Egbert 2011; Tietze and Ritter 2013; Burd et al. 2014; Heise et al. 2016) or combining both to fence diagrams (e.g., Bertrand et al. 2015; Heise et al. 2016). In some publications cube models are shown with oblique cuts through the model or disclosed faces of different levels and directions (e.g., Yang et al. 2014b; Lindsey and Newman 2015; Zhdanov et al. 2015; Ślęzak et al. 2016). Another approach is to image iso-surfaces of specific resistivity values or applying a threshold to blank certain resistivities (Bertrand et al. 2012a; Burd et al. 2014; Scholl et al. 2015). However, common to all is

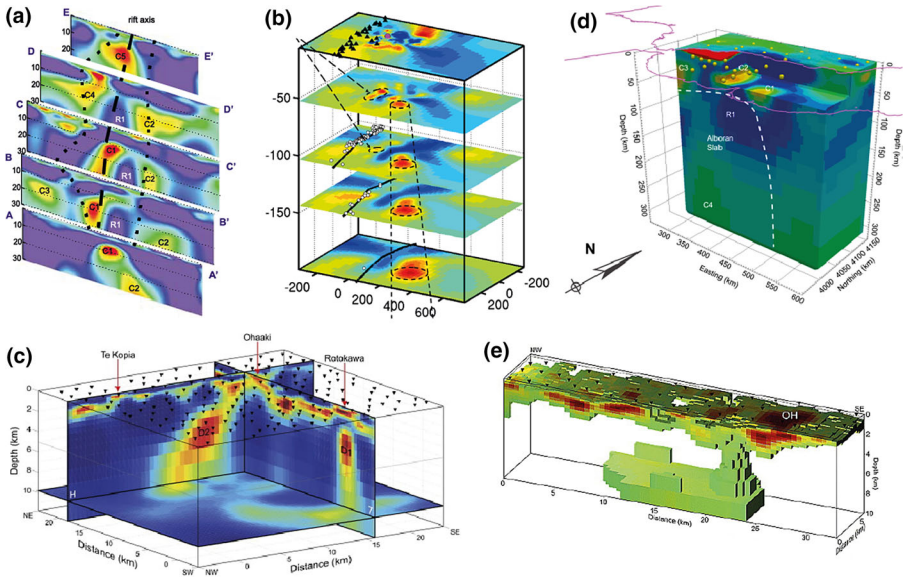

Fig. 25 Examples how to image 3-D models on 2-D media. The most common approaches are sequences of vertical section as familiar from 2-D models (**a** Heise et al. 2010), horizontal depth slices (**b** Burd et al. 2014) or a combination of both as fence diagram (**c** Bertrand et al. 2015), model cubes with oblique cuts (**d** Garcia et al. 2015) and iso-surfaces (**e** Bertrand et al. 2012a)

that they hide parts of the model and put others in the focus. Often the view is skewed and results in visual illusions—especially about position in space. Furthermore, it is all based on a personal choice! Patro and Sarma (2016) showed horizontal and vertical slices of their model but also provide a video slicing step by step through the model as digital supplementary data. Using videos to illustrate the resulting model is something already used in numerous oral presentations but is new for publications and still is no option for poster and other 2-D media. The aim should still be to present the 3-D models in 2-D in the least biased way possible.

Another—not new but still existing—issue is related to colour scale. Whether structures get in the focus or whether they are at all visible or not strongly depends on the chosen colour scale. It is not only a matter of the orientation of the colour sequence (i.e. red or blue being conductive) but also the chosen maximum and minimum values (i.e. the range and position of the scale) and the used colour gradient/scheme. Although it becomes less and less an issue, some journals print figures in greyscale only. However, not all colour scales are made to result in an equally well image in greyscale, rather often maximum and minimum values are not distinguishable. Additionally, one should keep in mind that a coloured image of the resistivity distribution might suggest different structural information to people with red-green-colour or total colour blindness than to those without.

The EarthScope example (Fig. 19) illustrates several of the issues related to visualization. Beside the different colour scales, the used projections and coordinate systems are not the same. Furthermore, the chosen depth slices and sections are not coinciding in most cases and the shown extent—especially depth extent—of the sections differs. This makes it extremely difficult to compare those two models properly and may be a challenge for interpretation.

Even if the resulting inverse model would be perfect, i.e. representing the subsurface without any shortcomings, the visualization for interpretation itself is source of errors due to assumptions and decisions made. This will result in bias as well as—unintentionally or on purpose—highlight structures while others are hidden.

5 Future Challenges

In general, there are many challenges in various areas of 3-D inversion of EM field data. Strategies for systematic and thorough model assessment need to be established as standard procedures. This would be promoted by, on the one hand, availability of codes to a broader usership just as, on the other hand, well-trained users, knowing how to apply those codes appropriately. The entire community is in demand for establishing a respectful, responsible and trustworthy atmosphere of sharing and cooperation. Furthermore, ongoing and new challenges are related to 3-D anisotropic inversion, modelling realistic situations (see Sect. 5.1) and monitoring (i.e. 4-D inversion; see Sect. 5.2). The latter two will be discussed in more detail below as well as challenges for CSEM (see Sect. 5.3), which is trying to keep up with developments in other EM fields (e.g., MT).

5.1 Modelling Realistic Situations

EM methods using electrical dipoles to measure the horizontal electric field, as is the case, for example, for MT, record the voltage between two grounded electrodes and divide it by the electrode separation. As Poll et al. (1989) already pointed out many years ago for 2-D, this procedure gives only an exact value if the electric field is uniform between the electrodes. This assumption fails for regions of near-surface inhomogeneity (i.e. only an average value for the electric field will be estimated) and, more extremely, if the electrodes are in contact with surface material of different resistivity (e.g., in the presence of a fault as shown for the Glouster Fault, Canada, by Poll et al. 1989). For the latter case, the electric field across the boundary of materials of different resistivities is discontinuous, and therefore, the used approximation results in quite inaccurate electric field estimations (Fischer et al. 1983). Poll et al. (1989) suggested that voltage divided by electrode separation is used as electric field estimate in model calculation to compare with real data on an equal basis. While in 2-D only the E_y component would be affected, in 3-D this discrepancy applies to both horizontal electric field components. Although this issue is known for quite a while, it is not addressed in common forward modelling and inversion codes. Beside a modification of the electric field formulation in the codes, it is also required to have the ability to discretize fine enough to actually be able to simulate correctly on the scale of electrode separation while accommodating a large-scale model of interest. Beside this electric field approximation, there are more and more MT studies, where the assumptions made are no longer valid (e.g., high-latitude data, influence of electrojet). Therefore, appropriate techniques are required that either correct or handle those data properly, or codes must be modified/enhanced that they are able to model those effects correctly.

Similarly, for CSEM the kilometre-long sources cannot be approximated by idealized unit dipoles without introducing significant errors (Streich and Becken 2011). Therefore, Grayver et al. (2014) introduced an approach to model realistic sources of complex geometries accurately without having to use very fine grids near the sources. They

considered the inductive component from the wire (up to 2 km long) and the contribution of the grounded electrodes (steel electrodes extending to depths of 5–10 m) in their calculation.

Another issue became obvious during the 'MT 3-D inversion III' workshop in Bari 2016. The forward test model DTM3 and the secret model DSM3—both including topography as well as bathymetry—turned out to be extremely challenging tasks for the forward modelling and therefore also for the inverse codes. Huge problems and large discrepancies between the different responses were observed trying to forward model an amphibian data set including topography and bathymetry. As the real world is not a flat earth of rectangular cubes, it is still a demanding task to be able to handle such complex scenarios appropriately. A lot more joint efforts of the community such as the COPROD2 and BC87 data (Jones 1993a, b) for 2-D inversion or the 'MT 3-D inversion' workshop series are required to compare forward and inversion results of synthetic as well as field data to enhance solutions.

Also not fully understood are the diagonal elements of the MT impedance tensor. While for real data the diagonals can be relatively large (up to the same order of magnitude as the off-diagonals), it is not trivial to generate large diagonal values for synthetic models. Hence, are they only large due to noise and misalignment to strike or do they actually contain structural information? It is important to understand the cause of those large diagonal elements to judge their importance for inversion and hence weight and fit them appropriately during inversion.

For most large-scale and some small-scale EM studies the ground truth is missing for the resulting models. Therefore, it can become a very difficult task to adjust the model to the real subsurface structure without any additional information such as borehole logging data. Hence, the ambiguity due to equivalent models is probably far more critical than instrumental errors and noise and is already an issue and concern especially for industry/commercial applications. Solving this issue could also be beneficial for 4-D, i.e. monitoring.

5.2 Monitoring

In particular, CSEM has a high potential to monitor hydrocarbon production, CO_2 storage horizons and geothermal systems in a continuous or time-lapse manner (e.g., Bhuyian et al. 2012; Tietze et al. 2015b, 2016; Vilamajó 2016). However, no matter what kind of method is used for monitoring, the most crucial issue is the repeatability of the measurements themselves. Cultural noise level, systematic installation errors as well as instrument noise and drift must be considered but also the natural EM signal as either unwanted signal or variable source. Additionally, if re-installation of instruments is necessary, an accurate relocation of receivers—and if applicable transmitters—is essential. Furthermore, changes in near-surface resistivity structures (e.g., due to rain) need to be handled. And how to deal with data sets (repeatedly) acquired over years—perhaps even with different equipment (e.g., due to enhancements in instrumentation), changing signal-to-noise ratios and diverse duration of recording or different frequencies used?

Improving monitoring concepts also demands further development of inversion codes and strategies. Often what matters is the change with time not the absolute resistivity distribution in the subsurface. Therefore, approaches considering only the changes during inversion rather than comparing absolute resistivity images could be seminal. For many years, time-lapse and difference inversion are common practice for monitoring using electrical resistivity tomography (e.g., Daily et al. 1992; Binley et al. 1996; LaBrecque and

Yang 2001). Another crucial aspect for monitoring is the time required from data acquisition to a final result. Commonly, this time scale is far too long to react immediately and, hence, techniques heading for real-time assessment, inversion and interpretation are required.

5.3 Controlled Source Electromagnetic (CSEM) Issues

Marine CSEM has been proven to be a useful tool to complement seismic data in exploration (e.g., Wright et al. 2002; Lien and Mannseth 2008; Orange et al. 2009; Andréis and MacGregor 2011), and recently, also land-based applications gain more attention (Wirianto et al. 2010; Girard et al. 2011; Bhuyian et al. 2012; Rödder and Tezkan 2013; Vilamajó et al. 2013; Zhdanov et al. 2013; Tietze et al. 2015b). First developed in academia to explore mid-ocean ridges and to study the oceanic lithosphere, marine CSEM is becoming routine in industry to explore hydrocarbons and seafloor gas hydrates (Weitemeyer et al. 2010 and references therein).

For a while the development of numerical and interpretation tools (forward and inverse codes) did not keep up with the progress in acquisition of marine CSEM data (e.g., Weitemeyer et al. 2010). Therefore, and because most marine CSEM data are collected along single tow lines or arrays of tow lines, 2-D or 2.5-D inversion is still commonly used (e.g., MacGregor et al. 2007; Weitemeyer et al. 2010). On the other hand, Zhdanov et al. (2015) claimed that their 3-D anisotropic inversion code, which is based on the 3-D contraction integral method and utilizes a re-weighted regularization conjugate gradient technique, is fast and efficient for a relatively large towed CSEM data set in a complex geological setting. Another approach based on the method of synthetic aperture (copied from the research done in the radar field) addresses the increasing challenge of exploring off-shore hydrocarbon in complex environment (e.g., deep targets, shallower water, small targets; Knaak et al. 2015). Nevertheless, CSEM 3-D inversion codes can be computationally so expensive—especially if full anisotropy is considered—that access to massively parallel computing platforms and computing times of days to weeks are required for a real-world problem.

In 2007, Constable and Srnka (2007) named the following future challenges for marine CSEM: (1) collection of a much broader frequency spectrum of data, (2) development of more numerous receiver instruments, (3) collection of continuous data in a reconnaissance survey mode, (4) application to shallow-water targets, (5) solution of the airwave problem and (6) 4-D reservoir monitoring. Although there has been some progress on (some of) those aspects in the last 10 years, there is still room for improvement, further research and enhanced developments.

For land-based CSEM, 3-D inversion also does not seem to be standard procedure although some studies in cooperation with industry try to tackle this issue (Grayver et al. 2014). The major focus currently is more related to explore and apply transmitter and receiver configurations taking advantage of the full 3-D subsurface space. Wirianto et al. (2010) showed that it is difficult to detect conductivity changes in 3-D targets at typical reservoir depths using only surface-to-surface configurations as the effects are below the resolution of field data. Therefore, vertical dipoles (Vilamajó et al. 2013, 2015) and a combination of horizontal and vertical sources (e.g., Tietze et al. 2015b) are used to increase the resolution significantly by placing receivers or transmitters in observation wells closer to the reservoir. Such a setting comes along with the challenge to correctly implement these sources/transmitters into numerical modelling and inversion (see also distortion due to steel casing in Sects. 3.2.2, 5.1). To date the examination of borehole-to-

surface CSEM is based on forward modelling studies and hypothesis tests (Tang et al. 2015; Tietze et al. 2015b; Vilamajó et al. 2015, 2016), but as those progress well the corollary is to do the next step towards 3-D inversion.

6 Conclusions

While most things mentioned in this review are far from new and are common procedures in 1-D and 2-D, it sometimes seems necessary to remind people that at least the same caution and care is also required in 3-D. Do not become lazy and over-credulous regarding the power of 3-D inversion codes—you still only get out what you put in! Therefore, it is important that every user inverting data makes herself/himself aware of how the inversion algorithm works and what the requirements, strengths and weaknesses are. This clearly requires effort and time, but to use the code in an appropriate manner to finally obtain good and reliable results, this should go without saying.

The key aspects that the practitioner of 3-D EM inversion has to consider and which were discussed in detail here are the following:

- keeping the 3-D inversion and its requirements already in mind during survey planning, data acquisition and data processing is beneficial for the final inverse model (see Sects. 2, 3.1)
- document your data selection clearly and reproducible (see Sect. 3.1.2)
- error estimates are as important as the data themselves and are a tool to weight the data during inversion, so choose them carefully (see Sect. 3.1.3)
- wisely choose and thoroughly test the mesh design as well as the initial and prior models and be aware of their assets and drawbacks (see Sects. 3.2, 3.3)
- thoroughly explore regularization and smoothing parameters and keep their influence on the final model in mind for interpretation (see Sect. 3.4)
- if data are distorted, one should investigate the different approaches to handle distortion appropriately (see Sect. 3.5)
- different approaches to deal with large data sets are available (see Sect. 3.6)
- take advantage of many different approaches to appreciate that a single number, i.e. RMS, cannot rate the misfit (see Sect. 3.7)
- regularized inversion depends on misfit, data type, site coverage, model parameterization, regularization parameters, etc. and, therefore, thorough model assessment is essential (see Sect. 3.8)
- interpret the final inverse model with a lot of care paying attention to all concerns such as limitation of detectability, presence of anisotropy and bias due to visualization (see Sect. 4)

Furthermore, each data set is unique. Therefore, a 3-D modelling procedure, which works with one data set, does not necessarily work with another data set. Ultimately, understanding your data set is the key to know how to model it in 3-D. Also, beware of all assumptions made—from acquisition to interpretation—and their consequences. Be conscious of what you are doing, know your tools and their limitations inside out and keep questioning your results. Remember that changing your perspective may make things look differently and do not deceive yourself by forcing your data to fit models based on erroneous assumptions.

Acknowledgements I would like to thank the IAGA Division IV and the organizing committee for the opportunity to prepare and present this review paper at the 23rd Electromagnetic Induction Workshop at Chiang Mai, Thailand. In addition, I would like to thank those within the EM community who have drawn my attention to a range of studies. I particularly would like to thank Karen R Christopherson, William Cumming, Randy Mackie and Rita Streich to share with me their experiences and challenges from a commercial point of view and Steven Constable for making his SEG/AAPG Fall Distinguished Lecture Tour 2016 presentation available. Furthermore, this review has benefited greatly from discussions with Angelika Ullmann, Raphael Dlugosch and Thomas Günther. I also thank two anonymous referees for their patient reading of this rather long manuscript and their detailed suggestions, which certainly improved this manuscript. And last but not least I would like to thank all those persons who accompanied, supported and encouraged me over many years in the 'EM world'.

References

Andréis D, MacGregor L (2011) Using CSEM to monitor production from a complex 3D gas reservoir—a synthetic case study. Lead Edge 30(9):1070–1079. https://doi.org/10.1016/j.geothermics.2010.01.002

Árnason K (2015) The static shift problem in MT soundings. In: Proceedings world geothermal congress 2015, Melbourne, Australia, 19–25 April 2015

Árnason K, Eysteinsson H, Hersir GP (2010) Joint 1D inversion of TEM and MT data and 3D inversion of MT data in the Hengill area. SW Iceland. Geothermics 39(1):13–34. https://doi.org/10.1016/j.geothermics.2010.01.002

Avdeev D (2005) Three-dimensional electromagnetic modelling and inversion from theory to application. Surv Geophys 26(6):767–799. https://doi.org/10.1007/s10712-005-1836-x

Avdeeva A, Moorkamp M (2015) Imaging the Kemaliye geothermal reservoir using three-dimensional magnetotelluric inversion with full distortion correction. In: AGU Fall Meeting, San Francisco, 14–18 December, NS34A-04

Avdeeva A, Moorkamp M, Avdeev D, Jegen M, Miensopust M (2015) Three-dimensional inversion of magnetotelluric impedance tensor data and full distortion matrix. Geophys J Int 202(1):464–481. https://doi.org/10.1093/gji/ggv144

Avdeeva A, Jegen M, Moorkamp M, Franz G (2016) Three-dimensional resistivity image of off-shore magmatism at the Walvis Ridge and Rift Basin. In: MT3DINV-3 workshop, 16–18 Mai, Bari, Italy

Bedrosian PA (2007) MT+, integrating magnetotellurics to determine earth structure, physical state, and processes. Surv Geophys 28(2):121–167. https://doi.org/10.1007/s10712-007-9019-6

Bedrosian PA, Feucht DW (2014) Structure and tectonics of the northwestern United States from EarthScope USArray magnetotelluric data. Earth Planet Sci Lett 402:275–289. https://doi.org/10.1016/j.epsl.2013.07.035 (reprinted figures with permission from Elsevier)

Berdichevsky MN, Dmitriev VI (1976a) Basic principles of interpretation of magnetotelluric sounding curves. In: Adam A (ed) Geoelectric and geothermal studies, KAPG geophysical monograph. Akadémiai Kiadó, Budapest, pp 165–221

Berdichevsky MN, Dmitriev VI (1976b) Distortion of magnetic and electrical fields by near-surface lateral inhomogeneities. Acta Geod Geophys Montan Acad Sci Hung 11:447–483

Berdichevsky MN, Bezruk IA, Chinavera OM (1973) Magnetotelluric sounding with the use of mathematical filters. Izv Akad Nauk SSSR Fiz Zeml 3:72–92 **(in Russian)**

Bertrand EA, Caldwell TG, Hill GJ, Wallin EL, Bennie SL, Cozens N, Onacha SA, Ryan GA, Walter C, Zaino A, Wameyo P (2012a) Magnetotelluric imaging of upper-crustal convection plumes beneath the Taupo Volcanic Zone, New Zealand. Geophys Res Lett 39(2):L02304. https://doi.org/10.1029/2011GL050177 (published on behalf of the American Geophysical Union by Wiley Periodicals)

Bertrand EA, Unsworth MJ, Chiang CW, Chen CS, Chen CC, Wu FT, Türkoğlu E, Hsu HL, Hill GJ (2012b) Magnetotelluric imaging beneath the Taiwan orogen: an arc-continent collision. J Geophys Res Solid Earth 117(B1). https://doi.org/10.1029/2011JB008688,b01402

Bertrand E, Caldwell T, Bannister S, Soengkono S, Bennie S, Hill G, Heise W (2015) Using array MT data to image the crustal resistivity structure of the southeastern Taupo Volcanic Zone, New Zealand. J Volcanol Geoth Res 305:63–75. https://doi.org/10.1016/j.jvolgeores.2015.09.020 (reprinted figure with permission from Elsevier)

Bhuyian AH, Landrø M, Johansen SE (2012) 3D CSEM modeling and time-lapse sensitivity analysis for subsurface CO2 storage. Geophysics 77(5):E343–E355. https://doi.org/10.1190/geo2011-0452.1

Bibby H, Caldwell T, Davey F, Webb T (1995) Taupo Volcanic Zone, New Zealand geophysical evidence on the structure of the Taupo Volcanic Zone and its hydrothermal circulation. J Volcanol Geoth Res 68(1):29–58. https://doi.org/10.1016/0377-0273(95)00007-H

Bibby HM, Caldwell TG, Brown C (2005) Determinable and non-determinable parameters of galvanic distortion in magnetotellurics. Geophys J Int 163(3):915–930. https://doi.org/10.1111/j.1365-246X.2005.02779.x

Binley A, Henry-Poulter S, Shaw B (1996) Examination of solute transport in an undisturbed soil column using electrical resistance tomography. Water Resour Res 32(4):763–769. https://doi.org/10.1029/95WR02995

Booker JR, Favetto A, Pomposiello MC (2004) Low electrical resistivity associated with plunging of the Nazca flat slab beneath Argentina. Nature 429:399–403. https://doi.org/10.1038/nature02565

Börner RU (2010) Numerical modelling in geo-electromagnetics: advances and challenges. Surv Geophys 31(2):225–245. https://doi.org/10.1007/s10712-009-9087-x

Bostick FX (1977) A simple almost exact method of MT analysis. In: Workshop on electrical methods in geothermal exploration, US Geological Survey Contract No 14080001-8-359

Burd AI, Booker JR, Mackie R, Pomposiello C, Favetto A (2013) Electrical conductivity of the Pampean shallow subduction region of Argentina near 33°s: evidence for a slab window. Geochem Geophys Geosyst 14(8):3192–3209. https://doi.org/10.1002/ggge.20213

Burd AI, Booker JR, Mackie R, Favetto A, Pomposiello MC (2014) Three-dimensional electrical conductivity in the mantle beneath the Payún Matrú Volcanic Field in the Andean backarc of Argentina near 36.5°S: evidence for decapitation of a mantle plume by resurgent upper mantle shear during slab steepening. Geophys J Int 198(2):812–827. https://doi.org/10.1093/gji/ggu145

Buselli G (1982) The effect of near-surface superparamagnetic material on electromagnetic measurements. Geophysics 47(9):1315–1324. https://doi.org/10.1190/1.1441392

Caldwell TG, Bibby HM, Brown C (2004) The magnetotelluric phase tensor. Geophys J Int 158(2):457–469. https://doi.org/10.1111/j.1365-246X.2004.02281.x

Candansayar ME, Tezkan B (2008) Two-dimensional joint inversion of radiomagnetotelluric and direct current resistivity data. Geophys Prospect 56(5):737–749. https://doi.org/10.1111/j.1365-2478.2008.00695.x

Cembrowski M, Junge A, Hering P, Vilamajó E (2016) Waiting for the storm geomagnetic activity and its influence on the magnetotelluric transfer functions. Abstract S1.2-P176, 23rd electromagnetic induction in the earth workshop, Chiang Mai, Thailand

Chave AD (2012) Estimation of the magnetotelluric response function. In: Chave AD, Jones AG (eds) The magnetotelluric method—theory and practice, chapter 5, Cambridge University Press, Cambridge, pp 165–218

Chave AD (2017) Estimation of the magnetotelluric response function: the path from robust estimation to a stable Maximum Likelihood Estimator. Surv Geophys. https://doi.org/10.1007/s10712-017-9422-6

Chave AD, Jones AG (1997) Electric and magnetic field galvanic distortion decomposition of BC87 data. J Geomagn Geoelectr 49:767–789

Chave AD, Smith JT (1994) On electric and magnetic galvanic distortion tensor decompositions. J Geophys Res (Solid Earth) 99(B3):4669–4682

Chave AD, Thomson DJ, Ander ME (1987) On the robust estimation of power spectra, coherences, and transfer functions. J Geophys Res Solid Earth 92(B1):633–648. https://doi.org/10.1029/JB092iB01p00633

Commer M, Newman GA (2009) Three-dimensional controlled-source electromagnetic and magnetotelluric joint inversion. Geophys J Int 178(3):1305–1316. https://doi.org/10.1111/j.1365-246X.2009.04216.x

Commer M, Newman GA, Carazzone JJ, Dickens TA, Green KE, AWahrmund L, EWillen D, Shiu J (2008) Massively parallel electrical-conductivity imaging of hydrocarbons using the IBM BlueGene/L supercomputer. IBM J Res Dev 52(1/2):93–103

Commer M, Hoversten GM, Um ES (2015) Transient-electromagnetic finite-difference time-domain earth modeling over steel infrastructure. Geophysics 80(2):E147–E162. https://doi.org/10.1190/geo2014-0324.1

Constable S (1993) Constraints on mantle electrical conductivity from field and laboratory measurements. J Geomagn Geoelectr 45(9):707–728. https://doi.org/10.5636/jgg.45.707

Constable S (2016) Geophysical inversion: which model do you want? SEG/AAPG fall distinguished lecture tour. http://marineemlab.ucsd.edu/~steve/SEGDL/

Constable S, Srnka LJ (2007) An introduction to marine controlled-source electromagnetic methods for hydrocarbon exploration. Geophysics 72(2):WA3–WA12. https://doi.org/10.1190/1.2432483

Constable S, Weiss CJ (2006) Mapping thin resistors and hydrocarbons with marine EM methods. Part II—modeling and analysis in 3D. Geophysics 71(6):G321–G332. https://doi.org/10.1190/1.2356908

Constable S, Key K, Lewis L (2009) Mapping offshore sedimentary structure using electromagnetic methods and terrain effects in marine magnetotelluric data. Geophys J Int 176(2):431. https://doi.org/10.1111/j.1365-246X.2008.03975.x

Constable S, Orange A, Key K (2015) And the geophysicist replied: "which model do you want?" Geophysics 80(3):E197–E212. https://doi.org/10.1190/geo2014-0381.1

Cox C (1980) Electromagnetic induction in the oceans and inferences on the constitution of the earth. Geophys Surv 4(1):137–156. https://doi.org/10.1007/BF01452963

Cox L, Endo M, Siemon B, Zhdanov M (2015) Large-scale 3D inversion of airborne modeling electromagnetic data based on the hybrid IE-FE method and the moving sensitivity domain approach. IN: 14th SAGA biennial conference & exhibition

Cox LH, Wilson GA, Zhdanov MS (2012) 3D inversion of airborne electromagnetic data using a moving footprint. Explor Geophys 41:250–259. https://doi.org/10.1071/EG10003

Cumming W, Mackie R (2010) Resistivity imaging of geothermal resources using 1D, 2D and 3D MT inversion and TDEM static shift correction illustrated by a Glass Mountain case history. In: Proceedings world geothermal congress 2010, Bali, Indonesia, 25–29 April 2010

Daily W, Ramirez A, LaBrecque D, Nitao J (1992) Electrical resistivity tomography of vadose water movement. Water Resour Res 28(5):1429–1442. https://doi.org/10.1029/91WR03087

de Groot-Hedlin C (1991) Short notice: removal of static shift in two dimensions by regularized inversion. Geophysics 56(12):2102–2106

de Groot-Hedlin C (1995) Inversion for regional 2-D resistivity structure in the presence of galvanic scatterers. Geophys J Int 122:877–888

Egbert GD, Booker JR (1986) Robust estimation of geomagnetic transfer functions. Geophys J Roy Astron Soc 87(1):173–194. https://doi.org/10.1111/j.1365-246X.1986.tb04552.x

Egbert GD, Kelbert A (2012) Computational recipes for electromagnetic inverse problems. Geophys J Int 189(1):251–267. https://doi.org/10.1111/j.1365-246X.2011.05347.x

Farquharson CG, Craven JA (2009) Three-dimensional inversion of magnetotelluric data for mineral exploration: an example from the McArthur River uranium deposit, Saskatchewan. Canada. J Appl Geophys 68(4):450–458. https://doi.org/10.1016/j.jappgeo.2008.02.002

Ferguson IJ (2012) Instrumentation and field procedures. In: Chave AD, Jones AG (eds) The magnetotelluric method—theory and practice, chapter 9. Cambridge University Press, Cambridge, pp 421–479

Fischer G (1979) Electromagnetic induction effects at an ocean coast. Proc IEEE 67(7):1050–1060. https://doi.org/10.1109/PROC.1979.11388

Fischer G, LeQuang BV, Müller I (1983) VLF ground surveys, a powerful tool for the study of shallow two-dimensional structures. Geophys Prospect 31:977–991

Fitterman DV, Stewart MT (1986) Transient electromagnetic sounding for groundwater. Geophysics 51(4):995–1005. https://doi.org/10.1190/1.1442158

Fullea J (2017) On joint modelling of electrical conductivity and other geophysical and petrological observables to infer the structure of the lithosphere and underlying upper mantle. Surv Geophys. https://doi.org/10.1007/s10712-017-9432-4

Gallardo LA, Meju MA (2003) Characterization of heterogeneous near-surface materials by joint 2D inversion of dc resistivity and seismic data. Geophys Res Lett 30(13). https://doi.org/10.1029/2003GL017370, 1658

Garcia X, Jones AG (2002) Decomposition of three-dimensional magnetotelluric data. In: Zhdanov MS, Wannamaker PE (eds) Three-dimensional electromagnetics, methods in geochemistry and geophysics, vol 35, chapter 13, Elsevier, Amsterdam, pp 235–250. ISBN: 0-444-50429-X

Garcia X, Jones AG (2008) Robust processing of magnetotelluric data in the AMT dead band using the continuous wavelet transform. Geophysics 73(6):F223–F234. https://doi.org/10.1190/1.2987375

Garcia X, Seillé H, Elsenbeck J, Evans RL, Jegen M, Hölz S, Ledo J, Lovatini A, Marti A, Marcuello A, Queralt P, Ungarelli C, Ranero CR (2015) Structure of the mantle beneath the Alboran Basin from magnetotelluric soundings. Geochem Geophys Geosyst 16(12):4261–4274. https://doi.org/10.1002/2015GC006100 (published on behalf of the American Geophysical Union by Wiley Periodicals)

Gasperikova E, Newman G, Feucht D, Arnason K (2011) 3D MT characterization of two geothermal fields in Iceland. Geotherm Res Counc Transact 35:1667–1671

Girard JF, Coppo N, Rohmer J, Bourgeois B, Naudet V, Schmidt-Hattenberger C (2011) Time-lapse CSEM monitoring of the Ketzin (Germany) CO_2 injection using 2xMAM configuration. Energy Procedia 4:3322–3329. https://doi.org/10.1016/j.egypro.2011.02.253

Gist G, Ciucivara A, Houck R, Rainwater M, Willen D, Zhou JJ (2013) Case study of a CSEM false positive—Orphan Basin, Canada. In: SEG technical program expanded abstracts 2013, chapter 157, pp 805–809. https://doi.org/10.1190/segam2013-0307.1

Grayver AV (2013) Three-dimensional controlled-source electromagnetic inversion using modern computational concepts. PhD thesis, Free University of Berlin
Grayver AV (2015) Parallel three-dimensional magnetotelluric inversion using adaptive finite-element method. Part I: theory and synthetic study. Geophys J Int 202(1):584–603. https://doi.org/10.1093/gji/ggv165
Grayver AV, Kolev TV (2015) Large-scale 3D geoelectromagnetic modeling using parallel adaptive high-order finite element method. Geophysics 80(6):E277–E291. https://doi.org/10.1190/geo2015-0013.1
Grayver AV, Streich R, Ritter O (2014) 3D inversion and resolution analysis of land-based CSEM data from the Ketzin CO2 storage formation. Geophysics 79(2):E101–E114. https://doi.org/10.1190/geo2013-0184.1
Groom RW, Bailey RC (1991) Analytic investigations of the effects of near-surface three-dimensional glavanic scatterers on MT tensor decompositions. Geophysics 56(4):496–518
Haber E, Heldmann S (2007) An octree multigrid method for quasi-static Maxwell's equations with highly discontinuous coefficients. J Comput Phys 223:783–796
Haber E, Holtham E, Granek J, Marchant D, Oldenburg D, Schwarzbach C, Shekhtman R (2012) An adaptive mesh method for electromagnetic inverse problems. https://doi.org/10.1190/segam2012-0828.1 (SEG Las Vegas 2012 annual meeting)
He Z, Hu Z, Luo W, Wang C (2010) Mapping reservoirs based on resistivity and induced polarization derived from continuous 3d magnetotelluric profiling: case study from Qaidam basin, China. Geophysics 75(1):B25–B33. https://doi.org/10.1190/1.3279125
Heidlauf DT, Hsui AT, dev Klein G (1986) Tectonic subsidence analysis of the Illinois Basin. J Geol 94(6):779–794
Heise W, Pous J (2001) Effects of anisotropy on the two-dimensional inversion procedure. Geophys J Int 147(3):610–621. https://doi.org/10.1046/j.0956-540x.2001.01560.x
Heise W, Bibby HM, Caldwell TG, Bannister SC, Ogawa Y, Takakura S, Uchida T (2007) Melt distribution beneath a young continental rift: the Taupo Volcanic Zone, New Zealand. Geophys Res Lett 34(14). https://doi.org/10.1029/2007GL029629, l14313
Heise W, Caldwell TG, Bibby HM, Bannister SC (2008) Three-dimensional modelling of magnetotelluric data from the Rotokawa geothermal field, Taupo Volcanic Zone. New Zealand. Geophys J Int 173(2):740–750. https://doi.org/10.1111/j.1365-246X.2008.03737.x
Heise W, Caldwell TG, Bibby HM, Bennie SL (2010) Three-dimensional electrical resistivity image of magma beneath an active continental rift, Taupo Volcanic Zone, New Zealand. Geophys Res Lett 37(10):L10301. https://doi.org/10.1029/2010GL043110 (published on behalf of the American Geophysical Union by Wiley Periodicals)
Heise W, Caldwell TG, Bertrand EA, Hill GJ, Bennie SL, Ogawa Y (2013) Changes in electrical resistivity track changes in tectonic plate coupling. Geophys Res Lett 40(19):5029–5033. https://doi.org/10.1002/grl.50959,2013GL057640
Heise W, Caldwell T, Bertrand E, Hill G, Bennie S, Palmer N (2016) Imaging the deep source of the Rotorua and Waimangu geothermal fields, Taupo Volcanic Zone, New Zealand. J Volcanol Geotherm Res 314:39–48. https://doi.org/10.1016/j.jvolgeores.2015.10.017
Hewson-Browne RC, Kendall PC (1976) Magnetotelluric modelling and inversion in three-dimensions. Acta Geod Geophys Montan Acad Sci Hung 11:427–446
Hill GJ, Caldwell TG, Heise W, Chertkoff DG, Bibby HM, Burgess MK, Cull JP, Cas RA (2009) Distribution of melt beneath Mount St Hellens and Mount Adams inferred from magnetotelluric data. Nat Geosci 2:785–789
Holtham E, Oldenburg D (2012) Practical issues of inverting 3D natural source electromagnetic data. In: Lane RJL (ed) Natural Fields EM Forum 2012: Abstracts from the ASEG Natural Fields EM Forum 2012, Geoscience Australia, Geoscience Australia Record 2012/04
Hunziker JW (2012) Marine controlled-source electromagnetic interferometry. PhD thesis, Technische Universiteit Delft
Ingham MR, Bibby HM, Heise W, Jones KA, Cairns P, Dravitzki S, Bennie SL, Caldwell TG, Ogawa Y (2009) A magnetotelluric study of Mount Ruapehu volcano. New Zealand. Geophys J Int 179(2):887–904. https://doi.org/10.1111/j.1365-246X.2009.04317.x
Ivanov PV, Pushkarev PY (2010) Possibilities of interpretation of the magnetotelluric data, obtained on a single profile over 3D resistivity structures. Izv Phys Solid Earth 46(9):727–734
Ivanov PV, Pushkarev PY (2012) Three-dimensional inversion of the single-profile magnetotelluric data. Izv Phys Solid Earth 48(11–12):871–876
Jegen M, Avdeeva A, Berndt C, Franz G, Heincke B, Hölz S, Neska A, Marti A, Planert L, Chen J, Kopp H, Baba K, Ritter O, Weckmann U, Meqbel N, Behrmann J (2016) 3-D magnetotelluric image of offshore

magmatism at the Walvis Ridge and rift basin. Tectonophysics 683:98–108. https://doi.org/10.1016/j.tecto.2016.06.016 (reprinted figure with permission from Elsevier)
Jiracek GR (1990) Near-surface and topographic distortions in electromagnetic induction. Surv Geophys 11(2–3):163–203. https://doi.org/10.1007/BF01901659
Johansen SE, Amundsen H, Røsten T, Ellingsrud S, Eidesmo T, Bhuiyan AH (2005) Subsurface hydrocarbons detected by electromagnetic sounding. First Break 23(3):31–36. https://doi.org/10.3997/1365-2397.2005005
Jones AG (1983) The problem of current channelling: a critical review. Geophys Surv 6(1–2):79–122. https://doi.org/10.1007/BF01453996
Jones AG (1993a) The BC87 dataset: tectonic setting, previous EM results, and recorded MT data. J Geomagn Geoelectr 45:1089–1105
Jones AG (1993b) The COPROD2 dataset: tectonic setting, recorded MT data and comparison of models. J Geomagn Geoelectr 45:933–955
Jones AG (2012) Distortion of magnetotelluric data: its identification and removal. In: Chave AD, Jones AG (eds) The magnetotelluric method—theory and practice, chapter 6. Cambridge University Press, Cambridge, pp 219–302
Jones AG, Chave AD, Egbert G, Auld D, Bahr K (1989) A comparison of techniques for magnetotelluric response function estimation. J Geophys Res Solid Earth 94(B10):14201–14213. https://doi.org/10.1029/JB094iB10p14201
Jones AG, Vozar J, Queralt P, Miensopust M, Siniscalchi A, Romano G, Mackie R, the 3D MT modellers (2016) The 3D secret model DSM3: model geometry, responses, and inverted models from MT code writers and code users. In: 23rd electromagnetic induction workshop, Chiang Mai, Thailand, 14–20 August 2016
Junge A (1996) Characterization of and correction for cultural noise. Surv Geophys 17(4):361–391. https://doi.org/10.1007/BF01901639
Kalscheuer T, De los Ángeles García Juanatey M, Meqbel N, Pedersen LB (2010) Non-linear model error and resolution properties from two-dimensional single and joint inversions of direct current resistivity and radiomagnetotelluric data. Geophys J Int 182(3):1174–1188. https://doi.org/10.1111/j.1365-246X.2010.04686.x
Kelbert A, Schultz A, Egbert G (2009) Global electromagnetic induction constraints on transition-zone water content variations. Nature 460:1003–1006. https://doi.org/10.1038/nature08257
Kelbert A, Egbert GD, deGroot Hedlin C (2012) Crust and upper mantle electrical conductivity beneath the Yellowstone Hotspot Track. Geology 40(5):447–450. https://doi.org/10.1130/G32655.1
Kelbert A, Meqbel N, Egbert GD, Tandon K (2014) ModEM: a modular system for inversion of electromagnetic geophysical data. Comput Geosci 66:40–53. https://doi.org/10.1016/j.cageo.2014.01.010
Key K (2016) MARE2DEM: a 2-D inversion code for controlled-source electromagnetic and magnetotelluric data. Geophys J Int 207(1):571. https://doi.org/10.1093/gji/ggw290
Key K, Constable S (2011) Coast effect distortion of marine magnetotelluric data: Insights from a pilot study offshore northeastern Japan. Phys Earth Planet Inter 184(3–4):194–207. https://doi.org/10.1016/j.pepi.2010.11.008
Key K, Ovall J (2011) A parallel goal-oriented adaptive finite element method for 2.5-D electromagnetic modelling. Geophys J Int 186(1):137. https://doi.org/10.1111/j.1365-246X.2011.05025.x
Khan A, Shankland T (2012) A geophysical perspective on mantle water content and melting: inverting electromagnetic sounding data using laboratory-based electrical conductivity profiles. Earth Planet Sci Lett 317–318:27–43. https://doi.org/10.1016/j.epsl.2011.11.031
Knaak A, Snieder R, Súilleabháin LÓ, Fan Y, Ramirez-Mejia D (2015) Optimized 3D synthetic aperture for controlled-source electromagnetics. Geophysics 80(6):E309–E316. https://doi.org/10.1190/geo2014-0348.1
LaBrecque DJ, Yang X (2001) Difference inversion of ERT data: a fast inversion method for 3-D in situ monitoring. J Environ Eng Geophys 6(2):83–89. https://doi.org/10.4133/JEEG6.2.83
Ledo J (2005) 2-D versus 3-D magnetotelluric data interpretation. Surv Geophys 26(5):511–543. https://doi.org/10.1007/s10712-005-1757-8
Ledo J, Queralt P, Marcuello A, Garcia-Yeguas A, Piña-Varas P, Prudencio I, Diaz A, Ibañez J (2016) Fuzzy-logic clustering of 3d magnetotelluric and seismic velocity models: Tenerife Island (Spain). In: International conference and exhibition, Barcelona, Spain, 3–6 April 2016, pp 85–85. https://doi.org/10.1190/ice2016-6312042.1
Lee T (1981) Transient electromagnetic response of a polarizable ground. Geophysics 46(7):1037–1041. https://doi.org/10.1190/1.1441241
Lien M, Mannseth T (2008) Sensitivity study of marine CSEM data for reservoir production monitoring. Geophysics 73(4):F151–F163. https://doi.org/10.1190/1.2938512

Lilley FEM (2015) The distortion tensor of magnetotellurics: a tutorial on some properties. Explor Geophys 47:85–99. https://doi.org/10.1071/EG14093

Lindsey NJ, Newman GA (2015) Improved workflow for 3D inverse modeling of magnetotelluric data: examples from five geothermal systems. Geothermics 53:527–532. https://doi.org/10.1016/j.geothermics.2014.09.004 (reprinted figure with permission from Elsevier)

Löwer A (2014) Magnetotellurische Erkundung geologischer Großstrukturen des südwestlichen Vogelsberges mit anisotroper, dreidimensionaler Modellierung der Leitfähigkeitsstrukturen. PhD thesis, Johann Wolfgang Goethe-Universität, Frankfurt am Main **(in German)**

MacGregor L, Barker N, Overton A, Moody S, Bodecott D (2007) Derisking exploration prospects using integrated seismic and electromagnetic data—a Falkland Islands case study. Lead Edge 26(3):356–359. https://doi.org/10.1190/1.2715059

Mackie R, Watts MD (2012) Detectability of 3-D sulphide targets with AFMAG. In: SEG technical program expanded abstracts 2012, chapter 257, pp 1–4. https://doi.org/10.1190/segam2012-1248.1

Mansoori I, Oskooi B, Pedersen L, Javaheri R (2016) Three-dimensional modelling of magnetotelluric data to image Sehqanat hydrocarbon reservoir in southwestern Iran. Geophys Prospect 64(3):753–766. https://doi.org/10.1111/1365-2478.12328

Martí A (2014) The role of electrical anisotropy in magnetotelluric responses: from modelling and dimensionality analysis to inversion and interpretation. Surv Geophys 35(1):179–218. https://doi.org/10.1007/s10712-013-9233-3

Martí A, Queralt P, Ledo J (2009) WALDIM: a code for the dimensionality analysis of magnetotelluric data using the rotational invariants of the magnetotelluric tensor. Comput Geosci 35:2295–2303. https://doi.org/10.1016/j.cageo.2009.03.004

Meqbel N, Ritter O (2015) Joint 3D inversion of multiple electromagnetic datasets. Geophys Prospect 63(6):1450–1467. https://doi.org/10.1111/1365-2478.12334

Meqbel N, Egbert G, Wannamaker P, Kelbert A, Schultz A (2014) Deep electrical resistivity structure of the northwestern U.S. derived from 3-D inversion of USArray magnetotelluric data. Earth Planet Sci Lett 402(C):290–304. https://doi.org/10.1016/j.epsl.2013.12.026 (reprinted figures with permission from Elsevier)

Meqbel N, Weckmann U, Muñoz G, Ritter O (2016) Crustal metamorphic fluid flux beneath the Dead Sea Basin: constraints from 2D and 3D magnetotelluric modelling. Geophys J Int 207(3):1609–1629. https://doi.org/10.1093/gji/ggw359

Miensopust MP (2010) Multidimensional magnetotellurics—a 2D case study and a 3d approach to simultaneously invert for resistivity structure and distortion parameters. PhD thesis, National University of Ireland, Galway

Miensopust MP, Queralt P, Jones AG, the 3D MT modellers (2013) Magnetotelluric 3-D inversion - a review of two successful workshops on forward and inversion code testing and comparison. Geophys J Int 193(3):1216–1238. https://doi.org/10.1093/gji/ggt066

Miensopust MP, Jones AG, Hersir GP, Vilhjálmsson AM (2014) The Eyjafjallajökull volcanic system, Iceland: insights from electromagnetic measurements. Geophys J Int 199(2):1187–1204. https://doi.org/10.1093/gji/ggu322

Moorkamp M (2017) Integrating electromagnetic data with other geophysical observations for enhanced imaging of the earth: a tutorial and review. Surv Geophys. https://doi.org/10.1007/s10712-017-9413-7

Moorkamp M, Avdeeva A, Erdogan E, Basokur A (2016) Three-dimensional magnetotelluric inversion with distortion correction, practical experience and solution recipes. EGU General Assembly, Vienna, Austria

Mulder W (2006) A multigrid solver for 3D electromagnetic diffusion. Geophys Prospect 54(5):633–649. https://doi.org/10.1111/j.1365-2478.2006.00558.x

Myer D, Constable S, Key K (2011) Broad-band waveforms and robust processing for marine CSEM surveys. Geophys J Int 184(2):689–698. https://doi.org/10.1111/j.1365-246X.2010.04887.x

Nechaev O, Shurina E, Botchev M (2008) Multilevel iterative solvers for the edge finite element solution of the 3D Maxwell equation. Comput Math Appl 55(10):2346–2362. https://doi.org/10.1016/j.camwa.2007.11.003

Newman GA (2013) A review of high-performance computational strategies for modeling and imaging of electromagnetic induction data. Surv Geophys 35(1):85–100. https://doi.org/10.1007/s10712-013-9260-0

Newman GA, Alumbaugh DL (2000) Three-dimensional magnetotelluric inversion using non-linear conjugate gradients. Geophys J Int 140(2):410–424. https://doi.org/10.1046/j.1365-246x.2000.00007.x

Newman GA, Boggs PT (2004) Solution accelerators for large-scale three-dimensional electromagnetic inverse problems. Inverse Prob 20(6):S151–S170

Newman GA, Recher S, Tezkan B, Neubauer FM (2003) 3D inversion of a scalar radio magnetotelluric field data set. Geophysics 68(3):791–802. https://doi.org/10.1190/1.1581032
Newman GA, Gasperikova E, Hoversten GM, Wannamaker PE (2008) Three-dimensional magnetotelluric characterization of the Coso geothermal field. Geothermics 37(4):369–399. https://doi.org/10.1016/j.geothermics.2008.02.006
Newman GA, Commer M, Carazzone JJ (2010) Imaging CSEM data in the presence of electrical anisotropy. Geophysics 75(2):F51–F61. https://doi.org/10.1190/1.3295883
Niblett ER, Sayn-Wittgenstein C (1960) Variation of electrical conductivity with depth by the magneto-telluric method. Geophysics 25(5):998–1008. https://doi.org/10.1190/1.1438799
Ó Súilleabháin L, Rosenquist M, Johnson J, Plessix R-É, Rensbergen PV, Sebayang D (2012) Anisotropic inversion of CSEM data from offshore Malaysia. In: Technical program expanded abstracts 2012, SEG, pp 1–5. https://doi.org/10.1190/segam2012-0726.1
Ogawa Y (2002) On two-dimensional modeling of magnetotelluric field data. Surv Geophys 23(2–3):251–273. https://doi.org/10.1023/A:1015021006018
Ogawa Y, Uchida T (1996) A two-dimensional magnetotelluric inversion assuming Gaussian static shift. Geophys J Int 126(1):69–76. https://doi.org/10.1111/j.1365-246X.1996.tb05267.x
Oldenburg D (1990) Inversion of electromagnetic data: an overview of new techniques. Surv Geophys 11(2–3):231–270. https://doi.org/10.1007/BF01901661
Oldenburg D, Yang D, Haber E (2013a) New strategies for faster 3D inversion of airborne EM data. In: 6th international AEM conference & exhibition
Oldenburg DW, Haber E, Shekhtman R (2013b) Three dimensional inversion of multisource time domain electromagnetic data. Geophysics 78(1):E47–E57. https://doi.org/10.1190/geo2012-0131.1
Olsen N (1999) Long-period (30 days-1 year) electromagnetic sounding and the electrical conductivity of the lower mantle beneath Europe. Geophys J Int 138(1):179–187. https://doi.org/10.1046/j.1365-246x.1999.00854.x
Orange A, Key K, Constable S (2009) The feasibility of reservoir monitoring using time-lapse marine CSEM. Geophysics 74(2):F21–F29. https://doi.org/10.1190/1.3059600
Oristaglio M, Spies B (eds) (1999) Three-dimensional electromagnetics, geophyscial developments, vol 7. SEG. ISBN: 1-56080-079-8
Padilha AL, Vitorello Í, Antunes CE, Pádua MB (2015) Imaging three-dimensional crustal conductivity structures reflecting continental flood basalt effects hidden beneath thick intracratonic sedimentary basin. J Geophys Res Solid Earth 120(7):4702–4719. https://doi.org/10.1002/2014JB011657
Patzer C, Tietze K, Ritter O (2017) Steel-cased wells in 3-D controlled source EM modelling. Geophys J Int 209(2):813–826. https://doi.org/10.1093/gji/ggx049
Patro PK, Egbert GD (2008) Regional conductivity structure of Cascadia: preliminary results from 3D inversion of USArray transportable array magnetotelluric data. Geophys Res Lett 35(20). https://doi.org/10.1029/2008GL035326,l20311
Patro PK, Egbert GD (2011) Application of 3D inversion to magnetotelluric profile data from the Deccan Volcanic Province of Western India. Phys Earth Planet Inter 187(1–2):33–46. https://doi.org/10.1016/j.pepi.2011.04.005 (reprinted figures with permission from Elsevier)
Patro PK, Sarma S (2016) Evidence for an extensive intrusive component of the Deccan Large Igneous Province in the Narmada Son Lineament region, India from three dimensional magnetotelluric studies. Earth Planet Sci Lett 451:168–176. https://doi.org/10.1016/j.epsl.2016.07.005
Patro PK, Uyeshima M, Siripunvaraporn W (2013) Three-dimensional inversion of magnetotelluric phase tensor data. Geophys J Int 192(1):58–66. https://doi.org/10.1093/gji/ggs014
Pellerin L, Hohmann GW (1990) Transient electromagnetic inversion: a remedy for magnetotelluric static shift. Geophysics 55(9):1242–1250
Poll HE, Weaver JT, Jones AG (1989) Calculations of voltages for magnetotelluric modelling of a region with near-surface inhomogeneities. Phys Earth Planet Inter 53:287–297
Puzyrev V, Koric S, Wilkin S (2016) Evaluation of parallel direct sparse linear solvers in electromagnetic geophysical problems. Comput Geosci 89:79–87. https://doi.org/10.1016/j.cageo.2016.01.009
Raiche A, Bennet A, Clark P, Smith R (1985) The use of Cole–Cole impedances to interpret the TEM response of layered earths. In: 4th ASEG conference
Ranganayaki RP, Madden TR (1980) Generalized thin sheet analysis in magnetotellurics: an extension of Price's analysis. Geophys J Int 60(3):445
Robertson K, Heinson G, Thiel S (2016) Lithospheric reworking at the Proterozoic–Phanerozoic transition of Australia imaged using AusLAMP magnetotelluric data. Earth Planet Sci Lett 452:27–35. https://doi.org/10.1016/j.epsl.2016.07.036
Rödder A, Tezkan B (2013) A 3D resistivity model derived from the transient electromagnetic data observed on the Araba fault, Jordan. J Appl Geophys 88:42–51. https://doi.org/10.1016/j.jappgeo.2012.09.009

Roos P, Burgess H, Ward I (2007) Updated mineral resource and reserve estimate, Cerro De Maimón Project, Msnr. Noul Province, Dominican Republic. Technical report NI 43-101 for GlobeStar Mining Corporation

Scheunert M, Ullmann A, Afanasjew M, Börner RU, Siemon B, Spitzer K (2016) A cut-&-paste strategy for the 3-D inversion of helicopter-borne electromagnetic data- I. 3-D inversion using the explicit Jacobian and a tensor-based formulation. J Appl Geophys. https://doi.org/10.1016/j.jappgeo.2016.03.023

Schilling FR, Partzsch GM, Brasse H, Schwarz G (1997) Partial melting below the magmatic arc in the central Andes deduced from geoelectromagnetic field experiments and laboratory data. Phys Earth Planet Inter 103:17–31. https://doi.org/10.1016/S0031-9201(97)00011-3

Scholl C, Neumann J, Watts MD (2015) Geo-steered 3D inversion of airborne electromagnetic data in rugged terrain. In: Near surface geoscience, First European Airborne Electromagnetics Conference, Turin, Italy, 6–10 September 2015. https://doi.org/10.3997/2214-4609.201413864

Schultz A, Egbert GD, Kelbert A, Peery T, Clote V, Fry B, Erofeeva S (2006–2018) Staff of the National Geoelectromagnetic Facility and their contractors. USArray TA Magnetotelluric Transfer Functions. https://doi.org/10.17611/DP/EMTF/USARRAY/TA

Schultz A, Egbert GD, Kelbert A, Peery T, Clote V, Fry B, Erofeeva S (2008–2013) Staff of the national geoelectromagnetic facility and their contractors. USArray BB Magnetotelluric Transfer Functions. https://doi.org/10.17611/DP/EMTF/USARRAY/BB

Sengpiel KP, Siemon B (2000) Advanced inversion methods for airborne electromagnetic exploration. Geophysics 65(6):1983–1992. https://doi.org/10.1190/1.1444882

Siemon B, Auken E, Christiansen AV (2009) Laterally constrained inversion of helicopter-borne frequency-domain electromagnetic data. J Appl Geophys 67(3):259–268. https://doi.org/10.1016/j.jappgeo.2007.11.003

Siripunvaraporn W (2011) Three-dimensional magnetotelluric inversion: an introductory guide for developers and users. Surv Geophys 33(1):5–27. https://doi.org/10.1007/s10712-011-9122-6

Siripunvaraporn W, Egbert G (2009) WSINV3DMT: vertical magnetic field transfer function inversion and parallel implementation. Phys Earth Planet Inter 173(3–4):317–329. https://doi.org/10.1016/j.pepi.2009.01.013

Siripunvaraporn W, Egbert G, Lenbury Y, Uyeshima M (2005a) Three-dimensional magnetotelluric inversion: data-space method. Phys Earth Planet Inter 150(1–3):3–14. https://doi.org/10.1016/j.pepi.2004.08.023

Siripunvaraporn W, Egbert G, Uyeshima M (2005) Interpretation of two-dimensional magnetotelluric profile data with three-dimensional inversion: synthetic examples. Geophys J Int 160(3):804–814. https://doi.org/10.1111/j.1365-246X.2005.02527.x

Sleep NH, Sloss LL (1978) A deep borehole in the Michigan Basin. J Geophys Res Solid Earth 83(B12):5815–5819. https://doi.org/10.1029/JB083iB12p05815

Ślęzak K, Jóźwiak W, Nowozyński K, Brasse H (2016) 3-D inversion of MT data for imaging deformation fronts in NW Poland. Pure Appl Geophys 1–12. https://doi.org/10.1007/s00024-016-1275-2

Smith JT (1997) Estimating galvanic-distortion magnetic fields in magnetotellurics. Geophys J Int 130(1):65–72. https://doi.org/10.1111/j.1365-246X.1997.tb00988.x

Stark MA, Soyer W, Hallinan S, Watts MD (2013) Distortion effects on magnetotelluric sounding data investigated by 3D modeling of high-resolution topography. Geotherm Resour Counc Trans 37:521–527

Sternberg BK, deGroot Hedlin C (1993) Removal of static shift in two dimensions by regularized inversion; discussion and reply. Geophysics 58(4):598–599. https://doi.org/10.1190/1.1443444

Sternberg BK, Washburne JC, Pellerin L (1988) Correction for the static shift in magnetotellurics using transient electromagnetic soundings. Geophysics 53(11):1459–1468. https://doi.org/10.1190/1.1442426

Streich R, Becken M (2011) Electromagnetic fields generated by finite-length wire sources: comparison with point dipole solutions. Geophys Prospect 59(2):361–374. https://doi.org/10.1111/j.1365-2478.2010.00926.x

Streich R, Becken M, Ritter O (2013) Robust processing of noisy land-based controlled-source electromagnetic data. Geophysics 78(5):E237–E247. https://doi.org/10.1190/geo2013-0026.1

Szarka L (1988) Geophysical aspects of man-made electromagnetic noise in the earth—a review. Surv Geophys 9(3):287–318. https://doi.org/10.1007/BF01901627

Tang W, Li Y, Swidinsky A, Liu J (2015) Three-dimensional controlled-source electromagnetic modelling with a well casing as a grounded source: a hybrid method of moments and finite element scheme. Geophys Prospect 63(6):1491–1507. https://doi.org/10.1111/1365-2478.12330

Thiel S, Heinson G (2013) Electrical conductors in Archean mantle—result of plume interaction? Geophys Res Lett 40(12):2947–2952. https://doi.org/10.1002/grl.50486

Thiel S, Heinson G, Mudge C, Chandrasekhar P, Alexander B (2012) 3D magnetotelluric inversion using cloud computing. In: Lane RJL (ed) Natural Fields EM Forum 2012: abstracts from the ASEG Natural Fields EM Forum 2012, Published by Geoscience Australia, Geoscience Australia Record 2012/04. ISBN: 978-1-921954-67-2

Thiel S, Heinson G, Reid A, Robertson K, (2016) Insights into lithospheric architecture, fertilisation and fluid pathways from AusLAMP MT. In: ASEG-PESA-AIG 2016, 25th geophysical conference & exhibition, 21–24 August. Adelaide, Australia

Tietze K, Ritter O (2013) Three-dimensional magnetotelluric inversion in practice-the electrical conductivity structure of the San Andreas Fault in Central California. Geophys J Int. 195(1):130–147. https://doi.org/10.1093/gji/ggt234

Tietze K, Ritter O, Egbert GD (2015a) 3-D joint inversion of the magnetotelluric phase tensor and vertical magnetic transfer functions. Geophys J Int 203(2):1128–1148. https://doi.org/10.1093/gji/ggv347

Tietze K, Ritter O, Veeken P (2015b) Controlled-source electromagnetic monitoring of reservoir oil saturation using a novel borehole-to-surface configuration. Geophys Prospect 63(6):1468–1490. https://doi.org/10.1111/1365-2478.12322

Tietze K, Ritter O, Patzer C, Veeken P, Verboom B (2016) Timelapse Borehole CSEM for HC-Saturation Monitoring in the Bockstedt Oilfield Onshore NW Germany. https://doi.org/10.2118/183165-MS (Society of Petroleum Engineers, Abu Dhabi International Petroleum Exhibition and Conference, 7–10 November)

Tikhonov A, Arsenin V (1977) Solutions of ill-posed problems. Scripta series in mathematics, Winston

Tuncer V, Unsworth MJ, Siripunvaraporn W, Craven JA (2006) Exploration for unconformity-type uranium deposits with audiomagnetotelluric data: a case study from the McArthur River mine, Saskatchewan. Canada. Geophysics 71(6):B201–B209. https://doi.org/10.1190/1.2348780

Türkoğlu E, Unsworth M, Pana D (2009) Deep electrical structure of northern Alberta (Canada): implications for diamond exploration. Can J Earth Sci 46(2):139–154. https://doi.org/10.1139/E09-009

Ullmann A, Scheunert M, Afanasjew M, Börner RU, Siemon B, Spitzer K (2016) A cut-&-paste strategy for the 3-D inversion of helicopter-borne electromagnetic data-II. Combining regional 1-D and local 3-D inversion. J Appl Geophys. 130:131–144. https://doi.org/10.1016/j.jappgeo.2016.04.008 (reprinted figures with permission from Elsevier)

Urzúa-Monsalve L (2008) Integration of a preliminary one-dimensional MT analysis with geology and geochemistry in a conceptual model of the Ngatamariki geothermal field. M.Sc. thesis, Univesity of Auckland

Viezzoli A, Christiansen AV, Auken E, Sørensen K (2008) Quasi-3D modeling of airborne TEM data by spatially constrained inversion. Geophysics 73(3):F105–F113. https://doi.org/10.1190/1.2895521

Vilamajó E (2016) CSEM monitoring at the Hontomín CO2 storage site: modeling, experimental design and baseline results. PhD thesis, Universitat de Barcelona

Vilamajó E, Queralt P, Ledo J, Marcuello A (2013) Feasibility of Monitoring the Hontomín (Burgos, Spain) CO2 Storage Site Using a Deep EM Source. Surv Geophys 34(4):441–461. https://doi.org/10.1007/s10712-013-9238-y

Vilamajó E, Rondeleux B, Queralt P, Marcuello A, Ledo J (2015) A land controlled-source electromagnetic experiment using a deep vertical electric dipole: experimental settings, processing, and first data interpretation. Geophys Prospect 63(6):1527–1540. https://doi.org/10.1111/1365-2478.12331

Vilamajó E, Puzyrev V, Queralt P, Marcuello A, Ledo J (2016) Study of the casing effect on Borehole-to-surface onshore CSEM. In: 78th EAGE conference and exhibition, 31 May, Vienna, Austria

Vozar J, Queralt P, Jones AG, Miensopust M, Romano G, Siniscalchi A, the 3D MT modellers (2016) The 3D forward DTM3 models benchmark studies for different MT forward solvers. In: 23rd electromagnetic induction workshop, Chiang Mai, Thailand, 14–20 August 2016

Wannamaker PE, Jiracek GR, Stodt JA, Caldwell TG, Gonzalez VM, McKnight JD, Porter AD (2002) Fluid generation and pathways beneath an active compressional orogen, the New Zealand Southern Alps, inferred from magnetotelluric data. J Geophys Res Solid Earth 107(B6):ETG 6-1–ETG 6-20. https://doi.org/10.1029/2001JB000186

Watts MD (2012) Reflections on natural field EM methods. In: 22nd international geophysical conference and exhibition, 26–29 February, Brisbane, Australia

Watts MD, Mackie R, Scholl C, Hallinan S (2013) Limitations of MT static shift corrections using time-domain EM data. https://doi.org/10.1190/segam2013-1078.1 (SEG technical program expanded abstracts 2013)

Weaver JT (1994) Mathematical methods for geo-electromagnetic induction. Research Studies Press, Baldock. ISBN: 10 086380165X. ISBN: 13 9780863801655

Weaver JT, Agarwal AK, Lilley FEM (2000) Characterization of the magnetotelluric tensor in terms of its invariants. Geophys J Int 141(2):321–336. https://doi.org/10.1046/j.1365-246x.2000.00089.x

Weitemeyer K, Gao G, Constable S, Alumbaugh D (2010) The practical application of 2D inversion to marine controlled-source electromagnetic data. Geophysics 75(6):F199–F211. https://doi.org/10.1190/1.3506004

Wheelock B, Constable S, Key K (2015) The advantages of logarithmically scaled data for electromagnetic inversion. Geophys J Int 201(3):1765. https://doi.org/10.1093/gji/ggv107

Wilt M, Williams J (1989) Layered model inversion of central-loop EM soundings near a geological contact. Explor Geophys 20:71–73

Wirianto M, Mulder WA, Slob EC (2010) A feasibility study of land CSEM reservoir monitoring in a complex 3-D model. Geophys J Int 181(2):741–755. https://doi.org/10.1111/j.1365-246X.2010.04544.x

Worzewski T, Jegen M, Swidinsky A (2012) Approximations for the 2-D coast effect on marine magnetotelluric data. Geophys J Int 189(1):357–368. https://doi.org/10.1111/j.1365-246X.2012.05385.x

Wright D, Ziolkowski A, Hobbs B (2002) Hydrocarbon detection and monitoring with a multicomponent transient electromagnetic (mtem) survey. Lead Edge 21(9):852–864. https://doi.org/10.1190/1.1508954

Xiao Q, Cai X, Xu X, Liang G, Zhang B (2010) Application of the 3D magnetotelluric inversion code in a geologically complex area. Geophys Prospect 58(6):1177–1192. https://doi.org/10.1111/j.1365-2478.2010.00896.x

Xu Y, Shankland TJ, Poe BT (2000) Laboratory-based electrical conductivity in the Earth's mantle. Journal of Geophysical Research: Solid Earth 105(B12):27865–27875. https://doi.org/10.1029/2000JB900299

Yang B, Xu Y, Egbert G, Liu Y (2014a) 3D inversion of audiomagnetotelluric data in Baogutu copper deposit, Western Junggar, NW China. In: Extended abstract 22nd EM induction workshop, Weimar, Germany, 25–30 August

Yang B, Egbert GD, Kelbert A, Meqbel NM (2015) Three-dimensional electrical resistivity of the north-central USA from EarthScope long period magnetotelluric data. Earth Planet Sci Lett 422:87–93. https://doi.org/10.1016/j.epsl.2015.04.006 (reprinted figure with permission from Elsevier)

Yang D, Oldenburg DW, Haber E (2014b) 3-D inversion of airborne electromagnetic data parallelized and accelerated by local mesh and adaptive soundings. Geophys J Int 196(3):1492–1507. https://doi.org/10.1093/gji/ggt465

Yang W, Torres-Verdín C, Hou J, Zhang ZI (2009) 1D subsurface electromagnetic fields excited by energized steel casing. Geophysics 74(4):E159–E180. https://doi.org/10.1190/1.3131382

Yavich N, Scholl C (2012) Advances in multigrid solution of 3D forward mCSEM problems. In: 5th Saint Petersburg international conference & exhibition—geosciences: maiking the most of the Earth's resources, Saint Petersburg, Russia, 2–5 April 2012

Yoshino T, Katsura T (2013) Electrical conductivity of mantle minerals: role of water in conductivity anomalies. Annu Rev Earth Planet Sci 41(1):605–628. https://doi.org/10.1146/annurev-earth-050212-124022

Zhdanov M, Varentsov I, Weaver J, Golubev N, Krylov V (1997) Methods for modelling electromagnetic fields results from COMMEMI—the international project on the comparison of modelling methods for electromagnetic induction. J Appl Geophys 37(3):133–271. https://doi.org/10.1016/S0926-9851(97)00013-X

Zhdanov M, Endo M, Black N, Spangler L, Fairweather S, Hibbs A, Eiskamp G, Will R (2013) Electromagnetic monitoring of CO_2 sequestration in deep reservoirs. First Break 31(2):71–78

Zhdanov M, Endo M, Sunwall D, Mattsson J (2015) Advanced 3D imaging of complex geoelectrical structures using towed streamer EM data over the Mariner field in the North Sea. First Break 33(11):59–63

Zhdanov MS, Green A, Gribenko A, Cuma M (2010) Large-scale three-dimensional inversion of EarthScope MT data using the integral equation method. Izv Phys Solid Earth 46(8):670–678

Zhdanov MS, Smith RB, Gribenko A, Cuma M, Green M (2011) Three-dimensional inversion of large-scale EarthScope magnetotelluric data based on the integral equation method: geoelectrical imaging of the Yellowstone conductive mantle plume. Geophys Res Lett 38(8). 10.1029/2011GL046953,l08307